Noise in a Dynamical Open Quantum System: Coupling a Resonator to an Artificial Atom

by Thomas Harvey

Thesis submitted to the University of Nottingham
for the degree of Doctor of Philosophy, April 2009

Abstract

The subject of this thesis is the study of a particular open quantum system consisting of a resonator coupled to a superconducting single electron transistor (SSET). The theoretical model we use is applicable to both mechanical and superconducting stripline resonators leading to a large parameter regime that can be explored. The SSET is tuned to the Josephson quasi-particle resonance, in which the transport occurs via Cooper pairs coherently tunnelling across one junction followed by the incoherent tunnelling of quasi-particles across the other. The SSET can be thought of as an artificial atom since it has a similar energy level structure and transitions to an atom. We investigate to what extent the current and current noise through the SSET can be used to infer the state of the resonator. In order to carry out these investigations we describe the system with a Born-Markov master equation, which we solve numerically. The evolution of the density matrix of the system is described by a Liouvillian superoperator. In order to better understand the results we perform an eigenfunction expansion of the Liouvillian, which is useful in connecting the behaviour of the resonator to the current noise. The mixture of coherent and incoherent processes in the SSET leads to interesting back action effects on the resonator. For weak coupling the SSET acts as an effective thermal bath on the resonator. Depending on the operating point the resonator can be either heated or cooled in comparison to its surroundings. In this regime we can use a set of mean field equations to describe the system and also capture certain aspects of the behaviour with some simple models. For sufficient coupling the SSET can drive the resonator into states of self-sustained oscillations. At the transition between stable and oscillating states of the resonator we also find regions of co-existence between oscillating and fixed point states of the resonator. The current noise provides a way to identify these transitions and the state of the resonator. The system also shows analogies with quantum optical systems such as the micromaser. We calculate the linewidth of the resonator and find deviations from the expected behaviour.

Acknowledgements

I would like to thank my supervisor Andrew Armour. Without his help and support this PhD would not have been possible. Also Denzil Rodrigues has been like a second supervisor and I have enjoyed working with them both.

I also want to thank Jane for giving me support home, where I have a life outside of physics. Finally I would like to thank my fellow PhD students who have made the last few years so enjoyable.

Contents

List of Figures

Chapter 1

Introduction

There is always a desire to scale down devices to ever smaller scales. An example, of relevance to this thesis, is electromechanical systems, which consist of an electronic device coupled to a mechanical degree of freedom. The first such device is thought to be Coulomb's electrical torsion balance in 1785 [1]. The idea of an electromechanical system is simply to act as a transducer, converting mechanical motion into a measurable electrical signal or conversely to convert an applied electrical signal into mechanical motion.

Devices at the micron-scale are known as microelectromechanical systems (MEMS). MEMS devices are common place and find applications in tiny moveable mirrors in digital projectors, motion sensors for car air bags, video game controllers and microbiology [1–3]. With the great successes of devices at the micron-scale the natural continuation is to the nano-scale and the creation of nanoelectromechanical systems (NEMS) [1, 2, 4–6].

At the nano-scale the mechanical part may be, a carbon nanotube [7], a small pillar [8], a cantilever [9] or a beam [10]. In figure 1.1 we show some examples of a few of these devices. The device in figure 1.1a is a shuttle device [8]. An ac voltage is applied to the pillar (labelled I) via the source and drain electrodes (labelled S and D). When the pillar is driven at the correct frequency an enhancement of the current is seen corresponding to electrons tunnelling onto the pillar when near the source electrode and off again when near the drain electrode. Devices of this kind may see applications as a mechanical switch [8].

In this thesis we are interested in devices of the type shown in figure 1.1c [10]. This consists of a single electron transistor (SET) [11, 12] where a freely suspended beam is capacitively coupled to the island (see Section 2.3). The current through the device is sensitive to the position of the beam and so could see applications in position detection [13].

Due to the small size of the mechanical parts they have very high fundamental

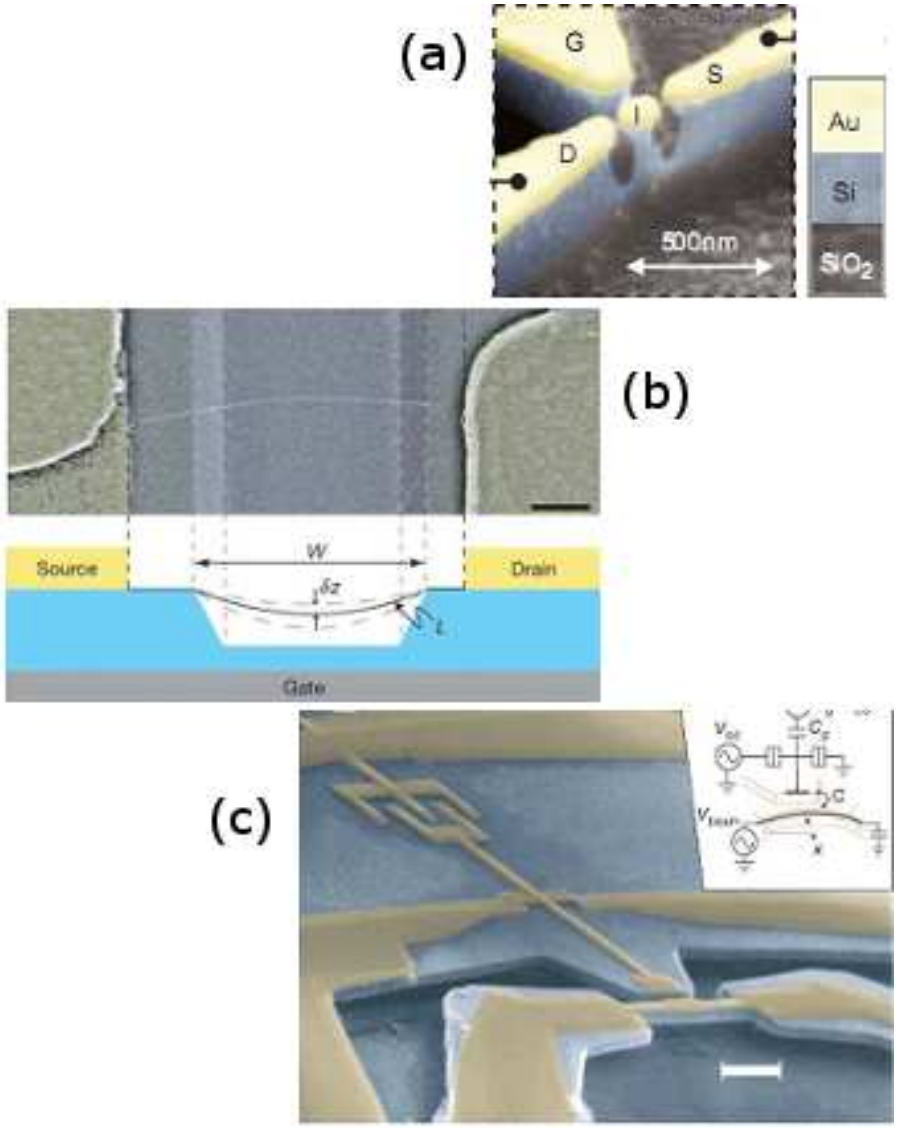

Figure 1.1. (a) Transistor with the island formed from from a nanomechanical pillar reproduced from [8][a]. (b) Suspended carbon nanotube forming the island of a transistor reproduced from [7][b]. (c) Single electron transistor where one of the plates of the gate capacitor is a doubly clamped beam, reproduced from [10][c]. The scale bar shows 1 μm

[a] Reprinted from Superlattices and Microstructures, **33**, R. H. Blick and D. V. Scheible, A quantum electromechanical device: the electromechanical single-electron pillar, p397, copyright (2003), with permission from Elsevier

[b] Reprinted by permission from Macmillan Publishers Ltd: Nature (**431** 284), copyright (2004)

[c] Reprinted by permission from Macmillan Publishers Ltd: Nature (**424** 291), copyright (2003)

frequencies, of the order 10Hz–1GHz. At these frequencies the device can be sufficiently cooled, in a dilution fridge, that the thermal fluctuations in energy of the beam, $k_B T$, are less than the spacing between energy states of a quantum harmonic oscillator, $\hbar\Omega$ [6]. This suggests that a quantum mechanical description is necessary for these devices and that in the future it should be possible to observe interesting quantum effects in NEMS [6].

At the nano-scale charging effects cannot be neglected when considering metallic objects [11]. These lead to discrete energy levels in the metallic island at the centre of the SET. The device we consider in this thesis is a superconducting SET (SSET), so Cooper pairs as well as quasi-particle excitations take part in the transport through the system, which leads to resonances in the current (see Section 2.2). We focus on a particular resonance known as the Josephson quasi-particle (JQP) resonance [14–17], where Cooper pair tunnelling takes place at one junction and quasi-particle tunnelling at the other. Theoretical investigations of the SSET-resonator system at this resonance have led to predictions of a range of interesting effects of the SSET on the resonator including cooling, driving into states of self-sustained oscillations and the formation of non-classical states [18–24]. Experimental efforts have so far have focused on cooling [21] and position detection [25].

Although an interesting field of study NEMS have yet to unambiguously show quantum behaviour [26–28]. However, the theoretical methods we use can equally be applied to other systems where a SSET couples to a harmonic mode. Superconducting stripline resonators support harmonic modes that at dilution fridge temperatures are almost unaffected by thermal noise. The strong coupling of electronic devices to superconducting stripline resonators has also been an area of active research experimentally, first with qubits [29], and more recently with a SSET at the JQP resonance [30], examples of which are shown in figure 1.2. It is thought that a superconducting stripline resonator could provide a bus between qubits in a quantum computer [31].

Electronic devices such as the SSET are often known as artificial atoms. This is because the energy level structure and transitions that occur in the solid state devices are similar to those in atoms. We can therefore use many techniques and ideas from quantum optics to investigate our device. The SSET interacting with a resonator shows many similarities with an atom interacting with a light field. In later chapters of this thesis we make some comparisons between features we find and those seen in quantum optical systems.

In a realistic model of any device it is important to take account of the surroundings of the system we are interested in. Within a quantum formulation this field is known as open quantum systems [32, 33]. Interaction with the environment leads to dissipation and can destroy the quantum nature of the device. However, interaction with the environment is also essential to perform measurements on the system, for instance there would be no dc current at the JQP resonance without dissipation.

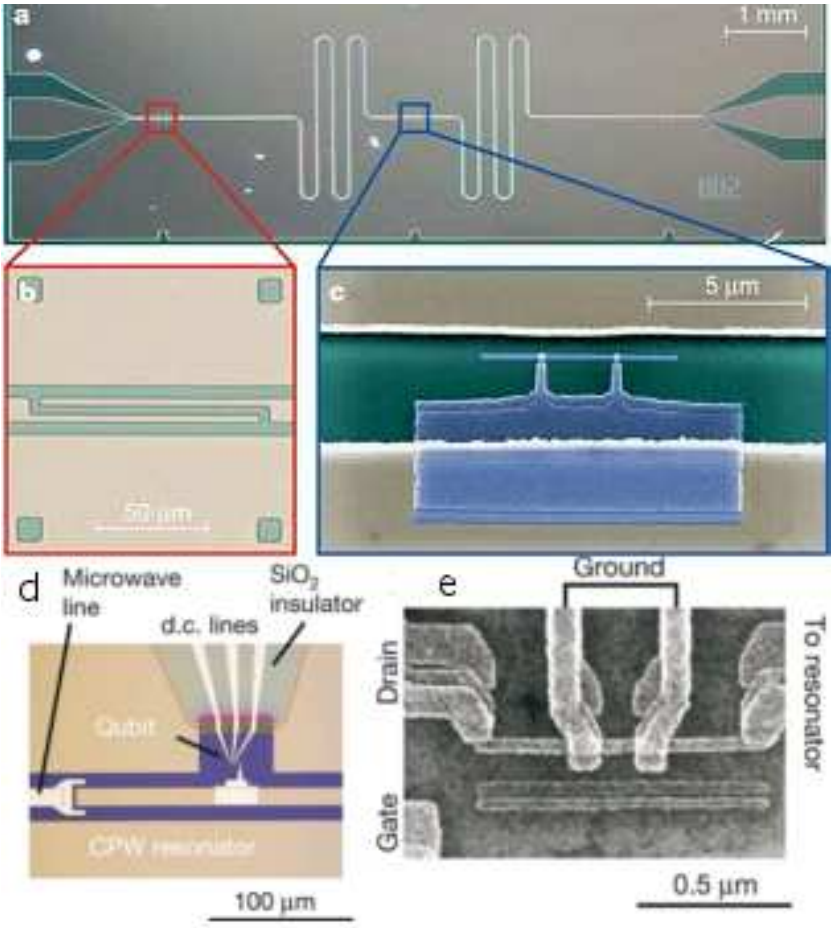

Figure 1.2. (a–c) False colour image of a qubit coupled to a superconducting stripline resonator reproduced from [29][a]. (a) Green regions are the silicon substrate and beige the central conductor and ground planes forming the cavity. (b) An expansion of one of the capacitors at the end of the cavity. (c) The qubit is shown in blue fabricated in the gap between the central conductor and ground plane. (d,e) Superconducting stripline resonator coupled to a SSET, reproduced from [30][b]. (d) Micrograph of one end of the resonator showing an aluminium strip that extends from the middle of the resonator to the SSET. (e) Scanning electron micrograph of the SSET.

[a] Reprinted by permission from Macmillan Publishers Ltd: Nature (**431** 162), copyright (2004)
[b] Reprinted by permission from Macmillan Publishers Ltd: Nature (**449** 588), copyright (2007)

Experimentally the state of the resonator is not directly accessible. The state must be inferred, either from measurements performed on the SSET or, for the case of the superconducting stripline resonator, emission from the cavity can be measured. As we show later the current through the SSET is only sensitive to average properties of the system, but the current noise can be used to reveal information about the dynamics of the resonator.

1.1 Outline

Chapter 2 of this thesis contains the background material and methods used in the following chapters to investigate the SSET-resonator system that is the subject of this thesis. It begins with a discussion of both normal and superconducting single electron transistors and the transport processes that occur. The coupling of the electronic device to a resonator is also described along with a discussion of two of the types of resonator (mechanical and superconducting) that we can consider. The remainder of the chapter is devoted to the master equation description of the system and the methods by which it can be used to calculate the steady-state and noise properties of the device.

Chapter 3 begins with a discussion of how the state of the resonator is determined and the types of dynamical state that occur. The simplest state of the resonator is the fixed point state, where the resonator is damped by the SSET. For weak coupling (between the SSET and resonator) the fixed point state is a thermal state, since the SSET behaves like an effective thermal bath for the resonator. If the system is tuned so that the SSET gives energy to the resonator during the JQP cycle then, for sufficient coupling, the resonator is driven into states of self-sustained oscillations, which we refer to as a limit cycle state. We also observe states where fixed point and limit cycle states co-exist. An overview of the behaviour for a range of parameters is given in Chapter 3, in order to identify regions of common behaviour. In particular we identify three frequency regimes of operation corresponding to the resonator being either much faster, much slower or on the same time-scale as the SSET. The chapter finishes with a comparison of the SSET-resonator system and the particular quantum optical device of a micromaser.

Chapter 4 is devoted to an analysis of the regime, in which the resonator remains in a thermal like state. The current through the SSET can be captured by a very simple model that assumes that the fluctuations in the position of the resonator cause a smearing out of the JQP current peak and a shift in the average position of the resonator causes a shift in the current peak. However, this simple model is not sufficient to capture the current noise, since it neglects both the dynamics of the resonator and the correlations between the SSET and resonator. Mean field equations can be used to describe the system but they do not form a closed set. Due to the Gaussian nature of the resonator distribution we can form a closed set of equations by assuming that all third

order cumulants of the operators used to describe the system are zero. These equations provide an accurate description of the system in this regime. We then derive a second simple model for the current noise that also includes the dynamics of the resonator, but still neglects correlations between the SSET and resonator. This second model is valid for a large external temperature or large external damping of the resonator. Finally we investigate the finite frequency current noise in this regime. It is found that a combination of the simple models and an eigenfunction expansion of the current noise expressions can be used to understand the spectrum.

The focus of Chapter 5 is the transitions between dynamical states of the resonator as a function of the parameters. We pay particular attention to the region where the dynamics of the resonator is approximately bistable. In this regime the resonator switches slowly between two different dynamical states, which are associated with two different average currents through the SSET. Extensive use is made of an eigenfunction expansion of the current noise in this chapter in order to connect fluctuations in the resonator to the current noise.

Chapter 6 is the final major chapter of the thesis. It is concerned with further laser analogies that can be explored in the device by focusing on the limit cycle region. For a laser the rate of phase diffusion is inversely proportional to the energy of the laser cavity. Although we find this to be true to some extent, calculations of the rate of phase diffusion for the SSET-resonator system show deviations from the simple relationship for the laser.

Chapter 7 gives the conclusions of the thesis. There are also a number of appendixes that give further details of various parts of the thesis and in addition a comparison with some recent experimental results in Appendix E.

Following Section 2.5 and with the exception of Section 4.1, the contents of this thesis are the result of new investigations carried out by the author in collaboration with Andrew Armour and Denzil Rodrigues. The main publication of the results contained in this thesis is in [24]. This publication focused on the zero frequency current noise and contained some of the numerical results from Chapter 3. In the thermal regime it included the results from Sections 4.2 and 4.3. Also introduced was the eigenfunction expansion of the current noise along with most of the results of Chapter 5. In an earlier publication, [22], some of the numerical methods as described in Section 2.5 and Appendix A were used. The work on phase diffusion described in Chapter 6 and the work on quantum trajectories described in Section 5.4 will be the subject of future publications.

Chapter 2

SSET and Resonator System

This chapter begins with a discussion of the normal state single electron transistor as this introduces many of the concepts required to understand the superconducting device. Section 2.2 then looks at a superconducting single electron transistor (SSET) and describes the resonant transport regimes. In particular the Josephson quasi-particle (JQP) resonance, which form the focus of this thesis, is discussed in detail. The master equation for transport at the JQP resonance is also given. Section 2.3 describes the coupling of a resonator to a single electron transistor. In Section 2.4 we give the full master equation description of the coupled SSET-resonator system. The way in which the master equation can be solved numerically is described in Section 2.5 together with details of the Liouville space description of the system. In Section 2.6 we introduce a formalism for calculating the noise spectrum of a pair of operators in a general system. Finally in Section 2.7 we apply this formalism to the SSET at the JQP resonance to calculate the current noise.

2.1 The single electron transistor

A single electron transistor (SET) [34] consists of a metal island linked to two leads by two tunnel junctions with capacitances C_L and C_R, as shown schematically in figure 2.1. The left and right junctions form the source and drain of the transistor and a voltage $V_{\rm ds}$ is applied across them. A capacitor, C_g, forms a gate and has a voltage V_g applied to it. The island has a charging energy, E_c, which is the electrostatic energy required to add an additional electron to the island [11],

$$E_c = \frac{e^2}{2C_{\rm T}}, \tag{2.1.1}$$

where $C_{\rm T} = C_L + C_R + C_g$ is the total capacitance of the island and $e = 1.6 \times 10^{-19}$C is the elementary charge. For a large device the charging energy is small and can easily

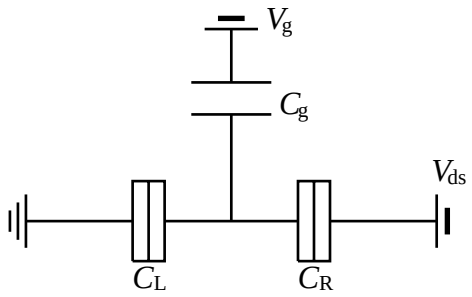

Figure 2.1. Schematic diagram of a SET. C_L and C_R are tunnel junctions across which a voltage $V_{\rm ds}$ is applied. C_g is the gate capacitor, which has a voltage V_g applied.

be overcome by thermal effects (i.e. $E_c \ll k_{\rm B}T$). For a small island, however, the total capacitance is small and we can have $E_c \gg k_B T$, so for an electron to tunnel onto the island a sufficiently large voltage bias must be applied in order to overcome this energy cost.

To understand the transport in the device we must consider the energy change of the system due to the tunnelling of a charge across each of the junctions. For the device shown in figure 2.1, assuming a positive bias ($V_{\rm ds} > 0$) and zero temperature so that electrons only flow from left to right, the relevant energy changes ΔE_L and ΔE_R for a single electron to tunnel across the left and right junctions are [12],

$$\begin{aligned}\Delta E_L(n) &= \frac{e}{C_T}\left[-\frac{e}{2} + C_g V_g + V_{\rm ds}\left(C_R + \frac{1}{2}C_g\right) - ne\right] \\ &= -E_c\left(2n + 1 - 2n_g\right) + c_R e V_{\rm ds}, \qquad (2.1.2)\\ \Delta E_R(n) &= \frac{e}{C_T}\left[-\frac{e}{2} - C_g V_g + V_{\rm ds}\left(C_L + \frac{1}{2}C_g\right) + ne\right] \\ &= E_c\left(2n - 1 - 2n_g\right) + c_L e V_{\rm ds}, \qquad (2.1.3)\end{aligned}$$

where n is the *initial* number of excess charges on the island. $n_g \equiv \frac{C_g V_g}{e}$ is the effective change in the number of charges on the island due to the applied gate voltage. $c_L \equiv \frac{2C_L + C_g}{2C_T}$ and $c_R \equiv \frac{2C_R + C_g}{2C_T}$ give the symmetry of the device and always sum to unity [35, 36]. Tunnelling across the left hand junction changes $n \rightarrow n + 1$ and tunnelling across the right hand junction $n \rightarrow n - 1$. In order for an electron to tunnel across a junction the energy change, as given by equation 2.1.2 or 2.1.3, must be positive, which corresponds to the system moving to a state of lower energy. The conditions on the bias that must be applied (for tunnelling in the forward direction) for

each of the two junctions are,

$$\Delta E_L : c_R e V_{\rm ds} \geq E_c \left(2n + 1 - 2n_g\right), \tag{2.1.4}$$

$$\Delta E_R : c_L e V_{\rm ds} \geq -E_c \left(2n - 1 - 2n_g\right), \tag{2.1.5}$$

Taking the simple example of an initially neutral island ($n = 0$), zero gate voltage ($V_g = 0$) and symmetric junctions ($c_L = c_R = \frac{1}{2}$). A drain source voltage of $eV_{\rm ds} \geq 2E_c$ is required for an electron to tunnel across either junction. For a second electron to tunnel across the same junction (and so change the island charge by two) will require $eV_{\rm ds} \geq 6E_c$. Further increasing $V_{\rm ds}$ allows states with larger numbers of electrons on the island to be accessed. So long as the tunnelling conditions for one junction are met the current can flow. The reason being that increasing n, by an electron tunnelling across the left hand junction, results in a reduction of the energy required to tunnel across the right hand junction. Similarly decreasing n, by an electron tunnelling across the right hand junction, reduces the energy requirement for tunnelling across the left hand junction. The restriction of the allowed charge states of the island due to charging effects is known as Coulomb blockade.

A clear signature of these charging effects can be observed experimentally as steps in the current for increasing drain source voltage known as the Coulomb staircase [37]. In order to observe the Coulomb staircase the junctions should be asymmetric [11]. To achieve this asymmetry we can still use equal capacitances but have the junction resistances very different. For example if the resistance of the right hand junction is small then any electrons that tunnel onto the island via the left hand junction can rapidly tunnel off again through the right hand junction. The current is then controlled by the ease with which electrons can tunnel across the left hand junction. The result is a jump in the current when a new island charge state becomes accessible [11].

By tuning the gate voltage the conditions for tunnelling are modified. For example if $n_g = 1/2$ an electron can tunnel from the left lead to the island at $V_{\rm ds} = 0$ and so the blockade is removed entirely. A stability plot, shown in figure 2.2, can be produced showing the regions where the Coulomb blockade restricts the charge state of the island to a fixed value. Small adjustments in the gate voltage switch the device from almost no current to a finite value. This allows the device to act as a very sensitive electrometer [38], the sensitivity of which is limited by the temperature of the device [11].

2.2 The superconducting single electron transistor

Single electron transistors are typically made of Aluminium [34, 38] and so at a low enough temperature become superconducting. A single electron transistor made entirely from superconducting material and below the transition temperature is known

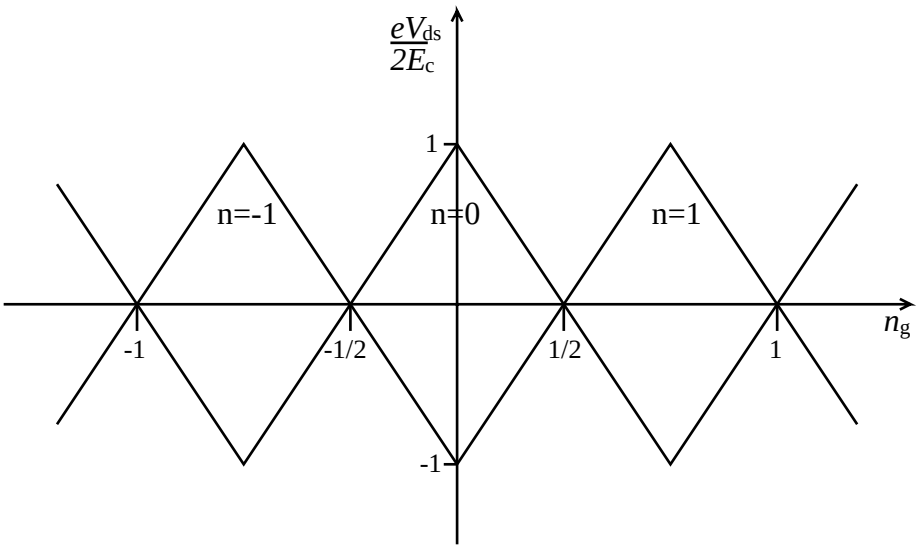

Figure 2.2. Coulomb diamonds for a single electron transistor, with $c_L = c_R = \frac{1}{2}$. Within the diamond shapes the island has a fixed charge (ne) and no current can flow. For $V_{\rm ds} > 0$ the Coulomb blockade conditions are given in equations 2.1.4 and 2.1.5. Equivalent conditions can be found for transport in the opposite direction ($V_{\rm ds} < 0$) [11].

as a superconducting single electron transistor (SSET) [39]. In a superconductor the main charge carriers are Cooper pairs. The tunnelling of Cooper pairs across the junctions is described by the Josephson effect [40]. In order for this tunnelling to occur the Fermi energies on each side of the junction must be close to alignment. Cooper pair tunnelling is a resonant process as opposed to the tunnelling of electrons in the SET, which has a threshold energy requirement.

In bulk superconductor electrons exist as quasi-particle excitations [39]. At a barrier it is the electron that tunnels through, although it exists as a quasi-particle on either side. We are not concerned with the details of this process here and just refer to the tunnelling of quasi-particles, see [39] for a detailed treatment.

The combination of the resonant tunnelling of Cooper pairs and incoherent tunnelling of quasi-particles leads to a number of different current processes in the SSET. We discuss some of these in Section 2.2.1. In this thesis we focus on a particular one of these current processes, that of the Josephson quasi-particle (JQP) cycle [14–17]. A model of which is discussed in Section 2.2.2.

2.2.1 Current Processes

In a superconductor a gap in the density of states opens at the Fermi energy of width 2Δ, where Δ is the superconducting gap. Thus for a quasi-particle (as opposed to a Cooper pair) to tunnel across a junction between two superconductors requires an

applied bias of at least this energy. For a pair of junctions the energy requirements calculated for the normal state SET will still hold, but an additional energy of 4Δ is required (2Δ for each junction). There is a region of large current above a drain source voltage of 4Δ, the border of which shows the Coulomb diamond shape seen in figure 2.2, see for example [41, 42]. The lowest value of the drain-source voltage at which the quasi-particle current can flow corresponds to $n_g = \frac{1}{2}$.

Other features occur for lower bias voltages than that required for pure quasi-particle current to flow. These are resonances involving the transport of Cooper pairs in the system, which is described by Josephson tunnelling [40, 43]. The following Hamiltonian can be used to describe the Cooper pair tunnelling across one of the junctions, between the states with n and $n+2$ excess charges on the island [43],

$$H_{cp} = \Delta E_{n,n+2} \, |n+2\rangle\langle n+2| - \frac{E_J}{2}\Big(|n\rangle\langle n+2| + |n+2\rangle\langle n| \Big), \qquad (2.2.1)$$

where E_J is the Josephson coupling energy between the two superconductors and $\Delta E_{n,n+2}$ is the electrostatic energy difference between the two charge states. Typically, E_J and $\Delta E_{n,n+2}$ will be different for each of the two junctions. Evolution under the Hamiltonian describes an oscillation between the n and $n+2$ charge states of the island, which corresponds to an AC current across the junction. When $\Delta E_{n,n+2} = 0$ the eigenstates of the Hamiltonian consist of a superposition of equal amounts of the two charge states, which corresponds to the resonant tunnelling of Cooper pairs.

For the left hand junction, $\Delta E^L_{n,n+2}$ can be calculated by using equation 2.1.2, which gives the energy to add an electron to the island. $\Delta E^L_{n,n+2}$ will be the energy required to add two electrons onto the island of the SET separately, across the left hand junction,

$$\Delta E^L_{n,n+2} = \Delta E_L(n) + \Delta E_L(n+1) = -4E_c\,(n+1-n_g) + 2c_R e V_{\rm ds}. \qquad (2.2.2)$$

For the right hand junction equation 2.1.3 gave the energy to remove an electron from the island across the right hand junction and so $\Delta E^R_{n,n+2}$ is,

$$\Delta E^R_{n,n+2} = \Delta E_R(n+2) + \Delta E_R(n+1) = 4E_c\,(n+1-n_g) + 2c_L e V_{\rm ds}. \qquad (2.2.3)$$

The Cooper pair resonance conditions are satisfied for lines in the $V_{\rm g}$–$V_{\rm ds}$ plane for different values of the initial island charge, ne, as shown in figure 2.3.

Cooper pair tunnelling alone will not lead to a DC current here. It is necessary to also have tunnelling of quasi-particles. At $eV_{\rm ds} = 2E_c$, as indicated in figure 2.3, there is a crossing between the Cooper pair resonance lines differing by $n = 1$. At this crossing a particular current resonance known as the double Josephson quasi-particle (DJQP) or $3e$ resonance occurs [44]. At the DJQP resonance only one junction is close to resonance for Cooper pair tunnelling at any one time. The current flows in

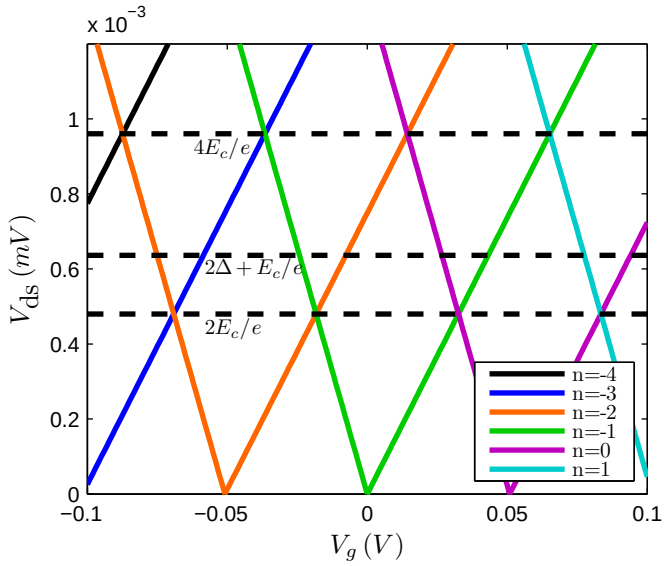

Figure 2.3. The lines indicate the positions of Cooper pair resonances in the $V_{\rm g}$–$V_{\rm ds}$ plane, as given by equations 2.2.2 and 2.2.3. The resonances occur between the charge states n and $n+2$. The parameters used are taken from the experiment in [42], $C_L = 210\,\text{aF}$, $C_R = 117\,\text{aF}$, $C_g = 3.15\,\text{aF}$, $E_c = 240\,\mu\text{eV}$ and $\Delta = 198\,\mu\text{eV}$. Note that the system has a negative bias applied in [42] and there is a shift in the gate voltage due to background charges that is not included here. Also indicated are the JQP cycle threshold ($2\Delta + E_c$), the position of the DJQP resonance ($2E_c$) and the crossing point of the JQP resonances with the same island charge ($4E_c$).

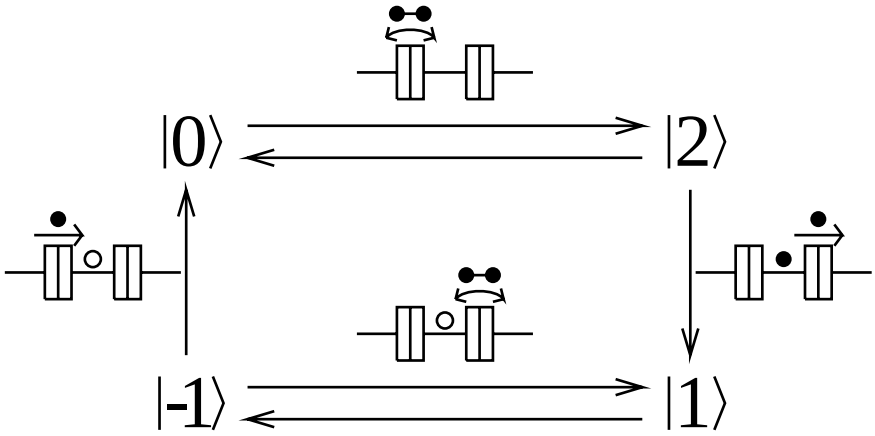

Figure 2.4. Double Josephson quasi-particle cycle (DJQP). $|-1\rangle$, $|0\rangle$, $|1\rangle$ and $|2\rangle$ correspond to -1, 0, 1 and 2 excess electrons on the island.

the following cycle, which is shown in figure 2.4. First one junction is on resonance for Cooper tunnelling. A quasi-particle then tunnels across the second junction, which switches the Cooper pair resonance to the second junction. A second quasi-particle tunnelling across the first junction then switches the system back to the initial state of the Cooper pair resonance at the first junction. It is known as the $3e$ resonance as three electrons are transported through the SSET during the cycle.

In this thesis we are going to study the Josephson quasi-particle (JQP) resonance [14–17]. For this resonance Cooper pair tunnelling is close to resonance at only one junction. For a sufficiently large drain source voltage two quasi-particles can tunnel sequentially across the other junction. Taken together the Cooper pair and quasi-particle tunnelling lead to a cycle, in which 2 charges are transferred through the SSET. The cycle is shown schematically in figure 2.5 for Cooper pair tunnelling at the left hand junction.

In addition to being near a resonance for Cooper pair tunnelling the JQP resonance requires that the tunnelling of the two quasi-particles is energetically favourable. Throughout this thesis we choose the left hand junction to be close to the Cooper pair resonance and consider quasi-particle tunnelling only at the right hand junction, although the results would be equally valid for the reverse case. The energy requirements for the quasi-particle tunnelling can be calculated from equation 2.1.3 with an additional penalty of 2Δ due to the superconducting gap. For an initial island charge of ne, and following the tunnelling of a Cooper pair onto the island across the left hand junction there will be $n+2$ excess electrons on the island. The energy changes for the two quasi-particles to tunnel across the right-hand junction and return the island to the

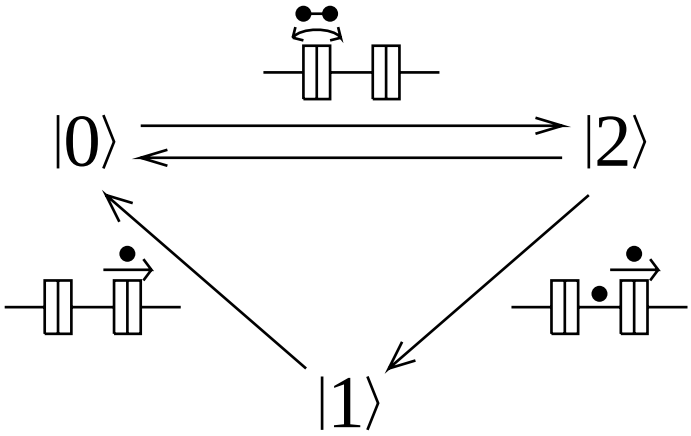

Figure 2.5. The JQP cycle, Cooper pairs tunnel across the left hand junction, which is interrupted by the splitting of the Cooper pair and the tunnelling of two quasi-particles through the right hand junction. $|0\rangle$, $|1\rangle$ and $|2\rangle$ correspond to zero, one or two electrons on the island.

n state are,

$$\Delta E_R(n+2) - 2\Delta = E_c\left(2n+3-2n_g\right) + c_L e V_{\rm ds} - 2\Delta, \tag{2.2.4}$$

$$\Delta E_R(n+1) - 2\Delta = E_c\left(2n+1-2n_g\right) + c_L e V_{\rm ds} - 2\Delta. \tag{2.2.5}$$

As before these changes must be positive. The second quasi-particle tunnelling requires the higher voltage so as long as this condition is satisfied the first will also be satisfied. For the JQP resonance there are two conditions that need to be met,

$$c_R e V_{\rm ds} \simeq 2E_c\left(n+1-n_g\right), \tag{2.2.6}$$

$$e V_{\rm ds} \geq E_c + 2\Delta. \tag{2.2.7}$$

The first is the condition for the Cooper pair resonance at the left hand junction and the second is the threshold voltage for quasi-particle tunnelling when *on resonance*, which is found by combining equations 2.2.5 and 2.2.6. Notice that the threshold is independent of the island charge, gate charge and capacitances and is indicated on figure 2.3.

Other processes such as Andreev reflection [45] can also be observed in this system. Throughout this thesis we assume that only the conditions for the JQP resonance are met and ignore all other transport processes.

There are several advantages of the JQP resonance that aid its experimental investigation. The cycle is periodic in e so unlike the supercurrent due to Cooper pair tunnelling alone it is not affected by quasi-particle poisoning, where an unwanted quasi-particle tunnels onto the island and blocks the supercurrent [39]. The periodicity also

means that it does not matter what the initial value of n is. The Cooper pair and quasi-particle tunnelling occur at different junctions so the parameters for the two processes can be individually tuned by constructing a very asymmetric device. For example the device in [46] allowed the adjustment of the Josephson coupling energy at one junction by applying a magnetic field. A high resistance tunnel junction formed the second junction, so the current could be used as a probe of the strong Josephson tunnelling.

2.2.2 Model of a SSET at the JQP resonance

A full master equation description of the SSET tuned to the JQP resonance can be derived from a Hamiltonian for the microscopic degrees of freedom of the system [47]. The Hamiltonian is split into two parts, the system consisting of the island charge and the reservoir consisting of the unwanted degrees of freedom of the SSET. To obtain the master equation the reservoir is traced out making Born and Markov approximations [32, 33, 48]. The approximation made is that correlations in the reservoir decay fast in comparison to the time scales in the system.

The JQP resonance is periodic in the island charge as is clear from equation 2.2.6 and figure 2.3. We label the states for an initially neutral island for simplicity, and so consider just the three charge states $|0\rangle$, $|1\rangle$ and $|2\rangle$. As mentioned previously we choose the Cooper pair tunnelling to be at the left hand junction. From equation 2.2.1 the Hamiltonian for the Cooper pair tunnelling part of the evolution is,

$$H_{\mathrm{SSET}} = \Delta E\,|2\rangle\langle 2| + \frac{E_J}{2}\left(|0\rangle\langle 2| + |2\rangle\langle 0|\right) \tag{2.2.8}$$

where $\Delta E \equiv \Delta E^L_{0,2} = -4E_c(1-n_g) + 2c_R e V_{\mathrm{ds}}$, is the detuning from the Cooper pair resonance (equation 2.2.2) and E_J is the Josephson coupling energy for the left hand junction. This Hamiltonian describes an effective qubit between the zero and two charge states. The evolution of the system is given by the master equation [17],

$$\dot{\rho}(t) = -\frac{i}{\hbar}\left[H_{\mathrm{SSET}}, \rho(t)\right] + \mathcal{L}_{\mathrm{qp}}\rho(t), \tag{2.2.9}$$

where $\rho(t)$ is the reduced density matrix of the system [33], describing just the three charge states and $\mathcal{L}_{\mathrm{qp}}$ is a superoperator describing the quasi-particle tunnelling. We will come back to a full description of superoperators in Section 2.5.

The quasi-particle part of the evolution is dissipative and causes decoherence of the qubit. It must include the two quasi-particle decays to take the system from the $|2\rangle$

state back to the $|0\rangle$ state incoherently. The quasi-particle term is given by [16, 22],

$$\begin{aligned}\mathcal{L}_{\rm qp}\rho(t) = \Gamma_{21}&\left[|1\rangle\langle 2|\,\rho(t)\,|2\rangle\langle 1| - \frac{1}{2}\left\{|2\rangle\langle 2|\,,\rho(t)\right\}\right]\\ &+\Gamma_{10}\left[|0\rangle\langle 1|\,\rho(t)\,|1\rangle\langle 0| - \frac{1}{2}\left\{|1\rangle\langle 1|\,,\rho(t)\right\}\right]\\ &+\frac{\Gamma_{21}+\Gamma_{10}}{2}\Big[\,|1\rangle\langle 2|\,\rho(t)\,|1\rangle\langle 0| + |0\rangle\langle 1|\,\rho(t)\,|2\rangle\langle 1|\,\Big],\end{aligned} \tag{2.2.10}$$

where Γ_{21}, Γ_{10} are the tunnelling rates for the two processes and $\{\cdot\,,\cdot\}$ is the anti-commutator. The terms on the first two lines describe the quasi-particle decays from $|2\rangle \rightarrow |1\rangle$ and $|1\rangle \rightarrow |0\rangle$ respectively and are of Lindblad form [49]. The final term is often omitted (e.g. [47]). It describes part of the evolution of the off-diagonal density matrix elements corresponding to the coherence between the $|1\rangle$ state and the other two charge states. Since the Hamiltonian (equation 2.2.8) does not generate any coherence between the $|1\rangle$ state and the $|0\rangle$ or $|2\rangle$ states these elements rapidly decay to zero and have no influence on the dynamics of the rest of the system, as we show below.

The quasi-particle tunnelling rate from left to right through a barrier is [50],

$$\Gamma(\varepsilon) = \frac{1}{e^2 R_N}\int_{-\infty}^{\infty} dE_i \varrho_L(E_i) f(E_i) \varrho_R(E_i+\varepsilon)\left[1-f(E_i+\varepsilon)\right], \tag{2.2.11}$$

where R_N is the junction resistance, $\varrho_{L(R)}(E_i)$ are the normalized density of states on the left (right) of the barrier, ε is the electrostatic energy change of the system (given by equation 2.1.3) and $f(E_i)$ is the Fermi function,

$$f(E_i) = \frac{1}{1+\exp\left(E_i/k_B T\right)}. \tag{2.2.12}$$

For a superconductor the density of states has a gap of width 2Δ at the Fermi energy $E_i = 0$,

$$\varrho(E_i) = \frac{|E_i|}{\sqrt{E_i^2-\Delta^2}}\Theta\left(|E_i|-\Delta\right), \tag{2.2.13}$$

where $\Theta(x)$ is the Heaviside step function.

Near the JQP resonance the energy changes, for the two transitions, are given by,

$$\varepsilon_{21} = \Delta E_R(2) = eV_{\rm ds} + E_c - \frac{1}{2}\Delta E, \tag{2.2.14}$$

$$\varepsilon_{10} = \Delta E_R(1) = eV_{\rm ds} - E_c - \frac{1}{2}\Delta E, \tag{2.2.15}$$

where we have incorporated the definition of ΔE into equation 2.1.3. For the quasi-particle tunnelling rates to be non-zero sufficient voltage must be applied in order to overcome the superconducting gap as shown in figure 2.6a. For the first quasi-particle tunnelling the threshold is at $eV_{\rm ds} = 2\Delta - E_c + \frac{1}{2}\Delta E$ and the second at $eV_{\rm ds} =$

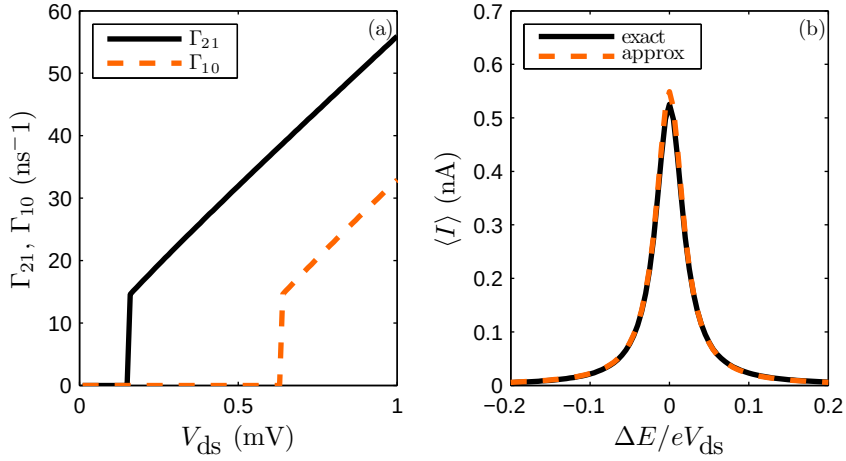

Figure 2.6. (a) Tunnelling rates at JQP resonance for varying drain source voltage at zero temperature obtained from a numerical integration of equation 2.2.11. (b) Current at the JQP resonance. *exact* is the current using rates calculated from equation 2.2.11 and *approx* is the current assuming that the rates are given by Γ_{21} at $\Delta E = 0$. Parameters are the same as in figure 2.3.

$2\Delta + E_c + \frac{1}{2}\Delta E$. After the threshold is reached the increase in the tunnelling rates are, to a good approximation, linear and given by $\Gamma_{21,10} = (eV_{\rm ds} \pm E_c)/e^2 R_N$ where the plus sign is for Γ_{21} [42].

From the master equation it is straightforward to write down a set of equations for the SSET island charge and the coherence between the $|0\rangle$ and $|2\rangle$ charge states. There are five equations in total for which we use the notation $\rho_{ab}(t) \equiv \mathrm{Tr}\left[|a\rangle\langle b|\,\rho(t)\right]$,

$$\dot{\rho}_{00}(t) = 1 - \dot{\rho}_{11}(t) - \dot{\rho}_{22}(t) \tag{2.2.16}$$

$$\dot{\rho}_{11}(t) = \Gamma_{21}\rho_{22}(t) - \Gamma_{10}\rho_{11}(t) \tag{2.2.17}$$

$$\dot{\rho}_{22}(t) = -i\frac{E_J}{2\hbar}\left(\rho_{02}(t) - \rho_{20}(t)\right) - \Gamma_{21}\rho_{22}(t) \tag{2.2.18}$$

$$\dot{\rho}_{02}(t) = \left(-i\frac{\Delta E}{\hbar} - \frac{\Gamma_{21}}{2}\right)\rho_{02}(t) + i\frac{E_J}{2\hbar}\left(\rho_{00}(t) - \rho_{22}(t)\right) \tag{2.2.19}$$

$$\dot{\rho}_{20}(t) = \dot{\rho}_{02}(t)^\dagger \tag{2.2.20}$$

Two of the equations have been expressed in terms of the other three. This can be done because of the Hermitian nature of the density matrix (equation 2.2.20) and the normalisation of the density matrix $\mathrm{Tr}\left[\rho(t)\right] = \rho_{00}(t) + \rho_{11}(t) + \rho_{22}(t) = 1$ (equation 2.2.16). Notice also that, as discussed below equation 2.2.10, we do not require equations for $\rho_{10}(t)$, $\rho_{01}(t)$, $\rho_{12}(t)$ or $\rho_{21}(t)$ in order to describe the evolution of the island charge.

The set of equations can be easily solved to find the steady-state probabilities for

each of the charge states. The current through the SSET at the JQP resonance is then [14, 51],

$$\begin{aligned}\langle I\rangle &= \Gamma_{21}\rho_{22}(\infty) + \Gamma_{10}\rho_{11}(\infty) \\ &= \frac{2eE_J^2\Gamma_{21}}{4\Delta E^2 + \hbar^2\Gamma_{21}^2 + E_J^2\left(2+\frac{\Gamma_{21}}{\Gamma_{10}}\right)},\end{aligned} \tag{2.2.21}$$

where the ∞ indicates that the probabilities are evaluated in the steady-state. In this thesis we will typically work in the regime of $E_J < \hbar\Gamma$ so the width of the peak is dominated by the quasi-particle tunnelling rate. Our choice of small E_J is motivated by the fact that this is the typical experimental regime for this device [21, 42] and is convenient since we can assume that the quasi-particle tunnelling process is the dominant source of decoherence in the system. Another source of dissipation is quantum leakage due to the coupling to other charge states of the island [52], however, near to $\Delta E = 0$ these couplings should be weak [53]. In Appendix E we do consider a larger value of E_J in order to perform a comparison with recent experiments [30] and include some additional qubit dephasing as well.

In equation 2.2.21 the tunnelling rate Γ_{10} only appears in the E_J term so it is the first quasi-particle rate that is most important. The rates also have only a weak dependence on the detuning. As shown in figure 2.6b the current peak is well approximated by using only the rate Γ_{21} evaluated at $\Delta E = 0$. Due to the insensitivity of the current to a difference in rates we assume equal tunnelling rates, $\Gamma = \Gamma_{21} = \Gamma_{10}$, throughout and also neglect any dependence of the rate on the detuning.

2.3 Coupling a resonator to a SET

In Section 2.1 it was stated that a SET is a very sensitive electrometer. Because of the sharp variation in current as a function of the SET operating point changes in gate charge can be detected to a high accuracy. The gate charge depends on both the gate voltage and the gate capacitance. By allowing one of the capacitor plates to move the device becomes a transducer converting the mechanical motion of the capacitor plate into a measurable change in current [13]. This method is applicable to nanomechanical beams that are too small for other detection methods such as optical interference [54].

Nanomechanical resonators can be fabricated at the same time as the SET as shown in figure 1.1d. The beam is fabricated either from metal or from semiconductor with a metal coating. The beam must then be under-etched to allow it to move freely [2].

There are a number of different mechanical deformations of a nanomechanical resonator [55]. It is the flexural modes in the plane of the substrate to which the SET is sensitive. The frequencies of the flexural modes for a doubly clamped beam are given

by [55],

$$\omega_i = \frac{\alpha_i^2 t}{l^2}\sqrt{\frac{E}{12\varrho}} \qquad \alpha_i = 4.73, 7.85, 11.00, 14.14, \ldots \tag{2.3.1}$$

where the beam has thickness t, length l, Young's modulus E and density ϱ. The beam is effectively stiffer to higher order modes of the beam as they require more bending [56] and hence more energy to produce a significant displacement. For a SET coupled to the centre of the resonator, such as the device in figure 1.1d, all even modes will have a node at the position of the SET. We can assume that the SET couples only to the fundamental mode. We also assume that the resonator is perfectly elastic so that the modes are independent and we need only consider the fundamental harmonic mode.

So long as the displacement of the resonator, x, is much less than the initial separation of the gate capacitor plates, d, we can assume that there is a linear dependence of the capacitance on the displacement [57].

$$C_g(x) = \frac{\varepsilon A}{d+x} \simeq C_g(0)\left(1 - \frac{x}{d}\right), \tag{2.3.2}$$

where ε is the permittivity of the dielectric and A the plate area.

The best sensitivity that can be obtained for continuous position detection is the quantum limit [25, 58, 59],

$$x_{\mathrm{QL}} = \sqrt{\frac{\hbar}{\ln 3 m\Omega}} \tag{2.3.3}$$

The calculation of the quantum limit includes not only the uncertainty in the position due to the uncertainty principle but also the back action of the measuring device. In terms of x_{QL} the best sensitivity achieved for a SET is $\sim 100\, x_{\mathrm{QL}}$ [10].

During transport through the SET the charges tunnel on and off the island randomly causing a fluctuating force on the resonator. This acts like an additional thermal bath on the resonator. The thermal bath is characterized by an effective temperature that is proportional to V_{ds} and always damps the resonator [57]. This back-action ultimately limits the sensitivity of the device so that the quantum limit cannot be reached [13, 60].

In a superconducting device the back-action is much richer. In order for DC current to flow through the SSET energy must be lost or gained through dissipation. In the absence of the resonator this dissipation occurs in the leads of the SSET. Instead energy can be exchanged with the resonator leading to energy loss in the resonator for positive detuning and energy gain for negative detuning. In the weak coupling regime, like the SET, the SSET acts on the resonator like an effective thermal bath [18, 19], which is the focus of Chapter 4. The effective temperature of the SSET can be much lower than that of the SET, which can lead to cooling of the resonator [21]. In terms of position detection, the reduced back-action has allowed sensitivities of $\sim 4\, x_{\mathrm{QL}}$ to be achieved [21, 25].

On the negative detuning side and for sufficiently strong coupling the transfer of

energy into the resonator leads to driving into states of self-sustained oscillations. This stronger coupling regime is investigated in Chapters 5 and 6. In Chapter 3 we describe the various states of the resonator in more detail.

Mechanical resonators have typical frequencies 10–1000 MHz and quality factors 10^3–10^6 [2]. Compared with the time-scale of the SSET ($\Gamma \sim 30\,\mathrm{GHz}$ from figure 2.6a) the resonator is slow, which does not allow us to explore the regime of a fast resonator in comparison to the SSET. However, a number of devices have been fabricated, in which a qubit is strongly coupled to a cavity mode in a superconducting stripline resonator [29] as shown in figures 1.2a–c. The cavity is formed from a strip of superconducting material patterned onto semiconductor with ground planes either side. Capacitors at each end are the equivalent of the mirrors in an optical cavity and allow the resonator to be probed.

The superconducting cavity supports a number of modes due to the electric field between the central conductor and the ground planes. These modes are similar to the harmonic flexural modes in the mechanical resonator. The qubit is fabricated in the gap between the central conductor and the ground plane as shown in figure 1.2c. A gate capacitance is formed between the qubit and the central conductor which provides the coupling. Just like for the mechanical device we can assume that only the fundamental mode is important.

Recently a SSET has also been coupled to a superconducting stripline resonator experimentally [30]. These resonators typically have frequencies $\sim$10 GHz and by using a high resistance tunnel junction Γ can be sufficiently reduced that we are in the regime of a fast resonator. We are therefore justified in exploring all frequency regimes for our device as both these types of resonator are described by the same Hamiltonian. Typically we will use language and notation appropriate for a mechanical resonator and use the terms phonons and photons interchangeably to refer to excitations.

2.4 Master equation description of the coupled system

Having introduced the device, that is the subject of this thesis, we now devote the remainder of this chapter to methods used in the solution. We use a master equation approach to describe the coupled dynamics of the SSET and resonator system, the derivation of which is outlined in [22]. The derivation is carried out in the same manner described in Section 2.2.2 for the SSET alone, in that the full Hamiltonian is first split into system and reservoir parts. The reservoir is then traced over by making Born and Markov approximations. We make the assumption that both the coupling between the system and reservoir and the coupling between the SSET and resonator is sufficiently weak that the baths corresponding to the SSET and resonator are independent [61]. The full master equation is then a combination of the master equations for a SSET (described in Section 2.2.2) and for a resonator, with the addition of a coupling term

between them in the Hamiltonian part.

The master equation describing the evolution of the reduced density matrix, $\rho(t)$, of the SSET and resonator at the JQP resonance is given by [22, 23],

$$\begin{aligned}\dot{\rho}(t) &= -\frac{i}{\hbar}\left[H_{\rm co}, \rho(t)\right] + \mathcal{L}_{\rm qp}\rho(t) + \mathcal{L}_{\rm d}\rho(t) \\ &= \mathcal{L}\rho(t). \end{aligned} \tag{2.4.1}$$

The first term describes the coherent evolution of the density matrix under the Hamiltonian $H_{\rm co}$, while the second and third terms describe the dissipative effects of quasiparticle tunnelling and the resonator's environment respectively. We define the following operators in terms of the three accessible charge states of the SSET for convenience,

$$\begin{aligned} p_0 &\equiv |0\rangle\langle 0|\,, & p_1 &\equiv |1\rangle\langle 1|\,, & p_2 &\equiv |2\rangle\langle 2|\,, \\ c &\equiv |0\rangle\langle 2|\,, & q_1 &\equiv |0\rangle\langle 1|\,, & q_2 &\equiv |1\rangle\langle 2|\,. \end{aligned} \tag{2.4.2}$$

The Hamiltonian, $H_{\rm co}$, written in terms of these operators takes the form,

$$H_{\rm co} = \Delta E p_2 - \frac{E_J}{2}\left(c + c^\dagger\right) + \frac{p^2}{2m} + \frac{1}{2}m\Omega^2 x^2 + m\Omega^2 x_s x\left(p_1 + 2p_2\right), \tag{2.4.3}$$

where ΔE is the detuning from the JQP resonance, E_J is the Josephson energy and the resonator has frequency Ω, mass m, momentum operator p and position operator x. The final term represents the linear coupling of the resonator to the charge on the SSET island. The length scale x_s is the shift in the resonator position due to the addition of a single electronic charge to the island. The coupling strength is conveniently expressed in terms of the dimensionless parameter $\kappa = \frac{m\Omega^2 x_s^2}{eV_{\rm ds}}$.

Quasi-particle decay at the right hand junction is described by the superoperator $\mathcal{L}_{\rm qp}$ given in equation 2.2.10. In terms of the new SSET operators and for $\Gamma = \Gamma_{21} = \Gamma_{10}$ this becomes,

$$\mathcal{L}_{\rm qp}\rho(t) = \Gamma\Big(q_1 + q_2\Big)\rho(t)\Big(q_2^\dagger + q_1^\dagger\Big) - \frac{\Gamma}{2}\left\{p_1 + p_2, \rho(t)\right\}, \tag{2.4.4}$$

where Γ is the quasi-particle tunnelling rate and $\{\cdot\,,\cdot\}$ is the anticommutator. Note that as discussed below equation 2.2.10 the terms $q_1\rho(t)q_2^\dagger$ and $q_2\rho(t)q_1^\dagger$ can be neglected. Due to our assumption that the SSET bath is unmodified, we have neglected the (weak) dependence of Γ on the position of the resonator [22]. The final term in equation 2.4.1 represents the damping of the resonator by its external environment.

$$\mathcal{L}_{\rm d}\rho(t) = -\frac{\gamma_{\rm ext} m\Omega}{2\hbar}\left(1 + 2\bar{n}_{\rm ext}\right)\left[x, \left[x, \rho(t)\right]\right] - \frac{i\gamma_{\rm ext}}{2\hbar}\left[x, \left\{p, \rho(t)\right\}\right], \tag{2.4.5}$$

where $\gamma_{\rm ext}$ is the damping rate and $\bar{n}_{\rm ext} = \left(e^{\hbar\Omega/k_{\rm B}T_{\rm ext}} - 1\right)^{-1}$ where $T_{\rm ext}$ is the

temperature of the resonator's surroundings. $\bar{n}_{\rm ext}$ gives the average occupation number the resonator would have in the absence of coupling to the SSET. The resonator bath used here is the Brownian motion bath. An alternative choice is obtained by making the rotating wave approximation (RWA). The advantage of the RWA bath is that the master equation will be of Lindblad form and so guarantee positivity of the density matrix. However, this is at the cost of losing translational invariance [62]. For weak external damping, which is always the case here, the Brownian motion bath will give a positive density matrix and it is useful to keep translational invariance in order to derive the correct mean field equations of the system [22, 62, 63].

In the main part of this thesis we do not include any source of decoherence in the SSET other than the quasi-particles. We justify this in terms of the values of the parameters chosen. We choose a relatively small junction resistance of $r = R_N e^2/h = 1$ throughout, where R_N is the junction resistance. $\Gamma \simeq V_{\rm ds}/eR_N$ as shown in Section 2.2.2. Also $E_J/eV_{\rm ds} = 1/16$ is used throughout so that $E_J \lesssim \hbar\Gamma$ corresponding to strong dephasing by the quasi-particles. In this parameter regime the quasi-particle decay should be the dominant source of decoherence. These parameters are similar to those used in the SSET-resonator experiments of Naik et al. [21]. In Appendix E we investigate a recent experiment [30] where $E_J > \hbar\Gamma$ and so include an additional source of decoherence to show what effect this has on the results. In terms of the resonator parameters we choose the external damping and frequency such that we can solve the problem over the range of parameters we vary whilst still observing a range of behaviours.

2.5 Liouville space and the steady state solution of the master equation

The whole master equation can be represented by the single superoperator $\mathcal{L}$, known as the Liouvillian. The Liouvillian operates in Liouville space where a Hilbert space operator a becomes a vector $|a\rangle\rangle$ and both pre- (left) and post- (right) multiplication of the operator a can be represented by an appropriate matrix multiplying $|a\rangle\rangle$ [33, 63–67]. The inner product for two vectors in Liouville space is defined as $\langle\langle a|b\rangle\rangle \equiv \mathrm{Tr}\left[a^\dagger b\right]$. Using this notation equation 2.4.1 takes the form,

$$\frac{d}{dt}\,|\rho(t)\rangle\rangle = \mathcal{L}\,|\rho(t)\rangle\rangle\,. \tag{2.5.1}$$

Since we are dealing with an open system, the Liouvillian is non-Hermitian and hence has different right, $|r_p\rangle\rangle$, and left, $|l_p\rangle\rangle$, eigenvectors,

$$\begin{aligned} \mathcal{L}\,|r_p\rangle\rangle &= \lambda_p\,|r_p\rangle\rangle\,, \\ \langle\langle l_p|\,\mathcal{L} &= \lambda_p\,\langle\langle l_p|\,. \end{aligned} \tag{2.5.2}$$

We choose to label the set of eigenvalues such that $|\lambda_0| < |\lambda_1| < \ldots$. Neglecting the possibility of degeneracy, we assume that the eigenvectors form a complete orthonormal set, $\langle\langle l_p|r_q\rangle\rangle \equiv \mathrm{Tr}\left[l_p^\dagger r_q\right] = \delta_{pq}$ [65]. The solution of equation 2.5.1 can be expanded in terms of the eigenvectors of $\mathcal{L}$ to give,

$$\begin{aligned} |\rho(t)\rangle\rangle &= \sum_{p=0}\langle\langle l_p|\rho(0)\rangle\rangle e^{\lambda_p t}\,|r_p\rangle\rangle \\ &= |r_0\rangle\rangle + \sum_{p=1}\langle\langle l_p|\rho(0)\rangle\rangle e^{\lambda_p t}\,|r_p\rangle\rangle\,, \end{aligned} \tag{2.5.3}$$

where $\rho(0)$ is an initial density matrix. For a master equation with a well-defined steady state (such as the one we consider here) the lowest eigenvalue will be $\lambda_0 = 0$, a property which we used to obtain the second line above. The other eigenvalues must obey $\Re\left(\lambda_{p>0}\right) < 0$ [65], where $\Re$ indicates the real part, and the steady state density operator is $|\rho(\infty)\rangle\rangle = |r_0\rangle\rangle$. The normalization of $|r_0\rangle\rangle$ is determined by $\mathrm{Tr}\left[\rho(t)\right] = 1$, which gives $\langle\langle l_0| = \langle\langle \hat{I}|$, where $\hat{I}$ is the identity operator (in Hilbert space). While $|r_0\rangle\rangle$ corresponds to the steady state, the eigenvectors $|r_p\rangle\rangle$ for $p > 0$ each represent a change to the steady state density matrix that decays exponentially with rate $-\Re\left(\lambda_p\right)$.

The problem of finding the steady state density matrix is reduced to finding the right hand eigenvector of $\mathcal{L}$ corresponding to the eigenvalue $\lambda_0 = 0$. By truncating the oscillator basis, equation 2.5.1 can be solved numerically to find a few eigenvalues and eigenvectors of $\mathcal{L}$. The numerical method and approximations that are made are described in Appendix A.

2.6 Formalism for calculating the noise spectrum of a pair of operators

The steady-state of a system only gives information about average quantities. By also calculating noise spectra, information about the dynamics of the system can be obtained. Of particular interest is the noise in the current of the system as this directly measurable in experiment and can provide important information about the dynamics of the resonator. In this section we discuss noise spectra in general and show how they are calculated for system operators. In Section 2.7 we will apply this general formalism to a calculation of the current noise through the SSET at the JQP resonance.

The symmetrized noise spectrum for any two operators a and b is [68],

$$S_{a,b}(\omega) = \lim_{t\to\infty} \int_{-\infty}^{\infty} d\tau \left\langle \{\bar{a}(t+\tau), \bar{b}(t)\} \right\rangle e^{i\omega\tau}, \tag{2.6.1}$$

where $\bar{a}(t) = a(t) - \langle a \rangle$ and $\langle a \rangle = \langle a(\infty) \rangle$, which is the expectation value of a in the steady-state. The symmetrized noise spectrum has the property $S_{a,b}(\omega) = S_{b,a}(-\omega)$. For a pair of operators the problem is to evaluate the correlation function in Fourier space. Note that we are discussing fluctuations about the steady-state of the system represented by the limit $t \to \infty$. Also note that here we have taken the Fourier transform with a factor of 2 in front as in [68]. Factors of 1 are used elsewhere (e.g. [63]) which lead to different numerical factors for the noise.

For system operators the quantum regression theorem (QRT) [32, 48] can be used to evaluate the correlation function. A system operator is one that acts only on the system Hilbert space. In order to apply the QRT we must rewrite the expression so that $\tau \geq 0$,

$$\begin{aligned} S_{a,b}(\omega) &= \lim_{t\to\infty} \int_{0}^{\infty} d\tau \Big(\left\langle \{\bar{a}(t+\tau), \bar{b}(t)\} \right\rangle e^{i\omega\tau} + \left\langle \{\bar{b}(t+\tau), \bar{a}(t)\} \right\rangle e^{-i\omega\tau} \Big) \\ &= S^{+}_{a,b}(\omega) + S^{-}_{a,b}(\omega), \end{aligned} \tag{2.6.2}$$

where we have defined,

$$S^{+}_{a,b}(\omega) = \lim_{t\to\infty} \int_{0}^{\infty} d\tau \left\langle \{\bar{a}(t+\tau), \bar{b}(t)\} \right\rangle e^{i\omega\tau} \tag{2.6.3}$$

$$S^{-}_{a,b}(\omega) = \lim_{t\to\infty} \int_{0}^{\infty} d\tau \left\langle \{\bar{b}(t+\tau), \bar{a}(t)\} \right\rangle e^{-i\omega\tau}. \tag{2.6.4}$$

The QRT states that the two-time correlation function can be rewritten in the following way [48],

$$\lim_{t\to\infty} \langle a(t+\tau)b(t) \rangle = \mathrm{Tr}\left[a e^{\mathcal{L}\tau} b \rho(\infty) \right], \qquad \tau \geq 0 \tag{2.6.5}$$

where a and b are system operators.

We first evaluate $S^{+}_{a,b}(\omega)$. The integral to be performed is a Laplace transform [69],

$$\begin{aligned} S^{+}_{a,b}(\omega) &= \int_{0}^{\infty} d\tau e^{i\omega\tau} \lim_{t\to\infty} \left[\langle a(t+\tau)b(t) \rangle + \langle b(t)a(t+\tau) \rangle - 2 \langle a \rangle \langle b \rangle \right] \\ &= \int_{0}^{\infty} d\tau e^{i\omega\tau} \Big[\mathrm{Tr}\left[a e^{\mathcal{L}\tau} b \rho(\infty) \right] + \mathrm{Tr}\left[a e^{\mathcal{L}\tau} \rho(\infty) b \right] - 2 \langle a \rangle \langle b \rangle \Big] \\ &= \mathrm{Tr}\left[a \left(-i\omega - \mathcal{L} \right)^{-1} \left(b\rho(\infty) + \rho(\infty) b \right) \right] + \frac{2}{i\omega} \langle a \rangle \langle b \rangle, \end{aligned} \tag{2.6.6}$$

where we have used the QRT and taken the $t \to \infty$ limit in the second line and then performed the Laplace transform in the final line. We continue using the Liouville space notation introduced in Section 2.5. We define symmetrized superoperators for a

and b,

$$\mathcal{A}\left|\rho(t)\right\rangle\!\rangle \equiv \frac{1}{2}\left(a\rho(t)+\rho(t)a\right), \tag{2.6.7}$$

$$\mathcal{B}\left|\rho(t)\right\rangle\!\rangle \equiv \frac{1}{2}\left(b\rho(t)+\rho(t)b\right). \tag{2.6.8}$$

In Liouville space equation 2.6.6 becomes,

$$S^{+}_{a,b}(\omega) = 2\left\langle\!\langle l_0\right|\mathcal{A}\left(-i\omega-\mathcal{L}\right)^{-1}\mathcal{B}\left|r_0\right\rangle\!\rangle + \frac{2}{i\omega}\left\langle\!\langle l_0\right|\mathcal{A}\left|r_0\right\rangle\!\rangle\left\langle\!\langle l_0\right|\mathcal{B}\left|r_0\right\rangle\!\rangle. \tag{2.6.9}$$

As in Section 2.5 we now perform an eigenfunction expansion of the Liouvillian and obtain the result,

$$S^{+}_{a,b}(\omega) = \sum_{p=1}^{\infty}\frac{2}{-i\omega-\lambda_p}\left\langle\!\langle l_0\right|\mathcal{A}\left|r_p\right\rangle\!\rangle\left\langle\!\langle l_p\right|\mathcal{B}\left|r_0\right\rangle\!\rangle \tag{2.6.10}$$

We can see now the importance of calculating the noise spectrum of the operators about their steady-state values. The constant terms cancel with the $p=0$ term corresponding to $\lambda_0 = 0$. Without this cancellation we would have a singularity as $\omega \to 0$. The spectrum can also be written in matrix form, in terms of projection operators as introduced by Flindt et al. [63],

$$S^{+}_{a,b}(\omega) = 2\left\langle\!\langle l_0\right|\mathcal{A}\mathcal{R}(\omega)\mathcal{B}\left|r_0\right\rangle\!\rangle, \tag{2.6.11}$$

where $\mathcal{R}(\omega)$ is the psuedo-inverse of the Liouvillian given by,

$$\mathcal{R}(\omega) = \mathcal{W}\left(-i\omega-\mathcal{L}\right)^{-1}\mathcal{W}, \tag{2.6.12}$$

where,

$$\mathcal{W} \equiv 1 - \left|r_0\right\rangle\!\rangle\left\langle\!\langle l_0\right|. \tag{2.6.13}$$

The matrix formulation is advantageous for numerical evaluation since we do not have to calculate the eigenspectrum of the Liouvillian, which is a non-trivial task. The eigenfunction expansion is used extensively in the interpretation of the noise spectra in later sections.

Similarly the $S^{-}_{a,b}(\omega)$ part of the noise spectrum is found using the same method to be,

$$\begin{aligned} S^{-}_{a,b}(\omega) &= \sum_{p=1}^{\infty}\frac{2}{i\omega-\lambda_p}\left\langle\!\langle l_0\right|\mathcal{B}\left|r_p\right\rangle\!\rangle\left\langle\!\langle l_p\right|\mathcal{A}\left|r_0\right\rangle\!\rangle \\ &= 2\left\langle\!\langle l_0\right|\mathcal{B}\mathcal{R}(-\omega)\mathcal{A}\left|r_0\right\rangle\!\rangle. \end{aligned} \tag{2.6.14}$$

The full spectrum is given by,

$$S_{a,b}(\omega) = 2\left\langle\!\left\langle l_0\right| \mathcal{A}\mathcal{R}(\omega)\mathcal{B} + \mathcal{B}\mathcal{R}(-\omega)\mathcal{A}\left|r_0\right\rangle\!\right\rangle . \tag{2.6.15}$$

For $a = b^\dagger$, which is normally the case, it can be shown in a straightforward manner from equations 2.6.3 and 2.6.4 that $S^-_{a,b}(\omega) = S^+_{a,b}(\omega)^\dagger$ and the full spectrum has the particularly simple form,

$$\begin{aligned} S_{a,b}(\omega) &= 4\Re\left\langle\!\left\langle l_0\right| \mathcal{A}\mathcal{R}(\omega)\mathcal{B}\left|r_0\right\rangle\!\right\rangle , \\ &= 4\Re\left[\sum_{p=1}^{\infty} \frac{1}{-i\omega - \lambda_p} \left\langle\!\left\langle l_0\right| \mathcal{A}\left|r_p\right\rangle\!\right\rangle\!\left\langle\!\left\langle l_p\right| \mathcal{B}\left|r_0\right\rangle\!\right\rangle\right] \end{aligned} \tag{2.6.16}$$

where $\Re$ indicates the real part.

2.7 Calculating the current noise of a SSET at the JQP resonance

In this section we use the formalism introduced in the previous section to show how the current noise through the SSET can be calculated. For a SSET alone an analytical solution of the current noise is possible [17], which has a simple form in the $\omega \to 0$ limit and is discussed in Section 3.2. The total current through the SSET at some time t is given by the Ramo-Shockley theorem,

$$I(t) = c_L I_L(t) + c_R I_R(t), \tag{2.7.1}$$

where I_L and I_R are the current at the left and right junctions respectively and c_L and c_R were introduced in Section 2.1. c_L and c_R must obey $c_L + c_R = 1$, we assume a symmetric SSET so take $c_L = c_R = 1/2$ [35]. Using this splitting and the charge conservation condition $\dot{Q}(t) = I_L(t) - I_R(t)$, where Q is the charge operator for the SSET island, the total current noise can be split into three parts [70],

$$S_{II}(\omega) = \frac{1}{2}S_{I_L I_L}(\omega) + \frac{1}{2}S_{I_R I_R}(\omega) - \frac{1}{4}\omega^2 S_{QQ}(\omega). \tag{2.7.2}$$

To find the full current noise spectrum we need to evaluate the current noise at each of the two junctions and also the charge noise of the island.

The charge operator is $Q = p_1 + 2p_2$. This is a system operator and so we define

the superoperator $\mathcal{Q}$ and from equation 2.6.16 write the result,

$$\mathcal{Q}\,|\rho(t)\rangle\!\rangle = \frac{1}{2}\left(Q\rho(t) + \rho(t)Q\right), \tag{2.7.3}$$

$$\begin{aligned} S_{Q,Q}(\omega) &= 4\Re\,\langle\!\langle l_0|\,\mathcal{Q}\mathcal{R}(\omega)\mathcal{Q}\,|r_0\rangle\!\rangle \\ &= 4\Re\left[\sum_{p=1}^{\infty}\frac{1}{-i\omega-\lambda_p}\,\langle\!\langle l_0|\,\mathcal{Q}\,|r_p\rangle\!\rangle\langle\!\langle l_p|\,\mathcal{Q}\,|r_0\rangle\!\rangle\right]. \end{aligned} \tag{2.7.4}$$

In order to determine the current operators for the two junctions we must consider the flow of charge into and out of the island [63]. This gives for the left hand junction the current operator,

$$I_L = i\frac{eE_J}{\hbar}\left(c^\dagger - c\right). \tag{2.7.5}$$

This is again a system operator so we can write down the result,

$$\mathcal{I}_L\,|\rho(t)\rangle\!\rangle = \frac{1}{2}\left(I_L\rho(t) + \rho(t)I_L\right) \tag{2.7.6}$$

$$\begin{aligned} S_{I_L,I_L}(\omega) &= 4\Re\,\langle\!\langle l_0|\,\mathcal{I}_L\mathcal{R}(\omega)\mathcal{I}_L\,|r_0\rangle\!\rangle \\ &= 4\Re\left[\sum_{p=1}^{\infty}\frac{1}{-i\omega-\lambda_p}\,\langle\!\langle l_0|\,\mathcal{I}_L\,|r_p\rangle\!\rangle\langle\!\langle l_p|\,\mathcal{I}_L\,|r_0\rangle\!\rangle\right]. \end{aligned} \tag{2.7.7}$$

The current operator at the right hand junction is a non-system operator as it involves the leads, which we have traced out. The definition of the current operator comes from the quasi-particle part of the dissipation (equation 2.4.4) and is given by,

$$\mathcal{I}_R\,|\rho(t)\rangle\!\rangle = e\Gamma\Big(q_1 + q_2\Big)\rho(t)\left(q_1^\dagger + q_2^\dagger\right) \tag{2.7.8}$$

In Appendix B we use the quantum trajectories method to derive the correct correlation function for the right hand junction, which is given by,

$$\lim_{t\to\infty}\langle\{I_R(t+\tau), I_R(t)\}\rangle = 2e\delta(\tau)\,\langle\!\langle l_0|\,\mathcal{I}_R\,|r_0\rangle\!\rangle + 2\,\langle\!\langle l_0|\,\mathcal{I}_R e^{\mathcal{L}\tau}\mathcal{I}_R\,|r_0\rangle\!\rangle \tag{2.7.9}$$

By comparison with the result from the QRT (equation 2.6.5), the correlation function is the same as that obtained for system operators but with the addition of a self-correlation term. The resulting spectrum is,

$$\begin{aligned} S_{I_R,I_R}(\omega) &= 2e\,\langle\!\langle l_0|\,\mathcal{I}_R\,|r_0\rangle\!\rangle + 4\Re\,\langle\!\langle l_0|\,\mathcal{I}_R\mathcal{R}(\omega)\mathcal{I}_R\,|r_0\rangle\!\rangle \\ &= 2e\,\langle\!\langle l_0|\,\mathcal{I}_R\,|r_0\rangle\!\rangle + 4\Re\left[\sum_{p=1}^{\infty}\frac{1}{-i\omega-\lambda_p}\,\langle\!\langle l_0|\,\mathcal{I}_R\,|r_p\rangle\!\rangle\langle\!\langle l_p|\,\mathcal{I}_R\,|r_0\rangle\!\rangle\right]. \end{aligned} \tag{2.7.10}$$

The same result was obtained by using an electron counting variable approach in [63].

The current noise is typically given in terms of the current Fano factor [68]. This is defined as,

$$F_I(\omega) = \frac{S_{II}(\omega)}{2e\,\langle I\rangle}. \tag{2.7.11}$$

The factor on the bottom is the Poissonian or shot noise limit of the current noise. This corresponds to the current noise through a single tunnel junction (i.e. the electrons are independent). A Fano factor of less than one means that the electrons tend to be more evenly separated, which is *sub-Poissonian* noise, and occurs in systems such as a quantum dot in the Coulomb blockade regime [71]. *Super-Poissonian* noise, on the other hand, indicates bunching of the transport electrons and a Fano factor greater than one. The definition of the Fano factor must be consistent with the definition of the current noise and so Fano factors can be easily compared.

We mainly consider the zero frequency current noise, which is the same for the two junctions due to charge conservation and so can be calculated using either equation 2.7.7 or 2.7.10. The charge noise does not contribute to the zero frequency current noise as can be seen from equation 2.7.2.

Chapter 3

Signatures of the Dynamical State of the Resonator

With the numerical tools described in Chapter 2 we are now in a position, in this chapter, to find the steady-state of the SSET-resonator system and analyse how it behaves. We then go on to show how the current and current noise can be a useful probe of the resonator state. In Section 3.1 we describe how the state of the resonator can be inferred from the steady-state solution. Section 3.2 gives a summary of the current and zero frequency current noise for a SSET alone, which are useful as a comparison to the results for the coupled system. The parameter space for the SSET-resonator system can be divided into regions of similar behaviour in a number of ways. In Section 3.3 we describe three frequency regimes of operation that we use throughout this thesis. Sections 3.4–3.6 each focus on a particular frequency regime for the system and describe the overall behaviour as the detuning and coupling are varied. Finally in Section 3.7 we make a comparison between the SSET-resonator system and the particular quantum optical system of a micromaser.

3.1 Determining the dynamical state of the resonator

The interaction between the SSET and resonator leads to a modification of the steady-state of the resonator. Cooper pairs can exchange energy with the resonator when they tunnel between the lead and island. When the SSET is biased so that $\Delta E < 0$ the Cooper pairs lose energy when tunnelling from the lead to the island and so energy can be given to the resonator. In contrast, $\Delta E > 0$ corresponds to the Cooper pairs needing to gain energy to go from the lead to the island and so energy can be removed from the resonator. For sufficiently large coupling the resonator can be driven into states of self-sustained oscillations. States of multi-stability can also be observed, nor-

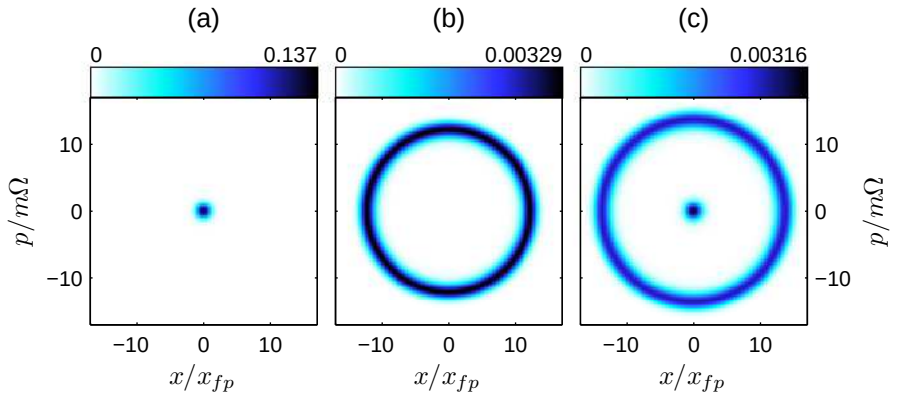

Figure 3.1. Wigner distributions, (a) fixed point, (b) limit cycle and (c) bistable. The parameters used are $\Omega = \Gamma$, $\kappa = 0.005$, $\gamma_{\rm ext} = 8\times10^{-4}\,\Gamma$, $E_J = 1/16\,eV_{\rm ds}$, $r = 1$, $\bar{n}_{\rm ext} = 0$ and the values of $\Delta E/eV_{\rm ds}$ are (a) -0.7, (b) -0.486 and (c) -0.4.

mally consisting of both an oscillating and a fixed point state. Regions where multiple oscillating states can also be observed [23], which we investigate in Section 3.7.

The method described in Section 2.5 and Appendix A can be used to find the steady-state density matrix of the system, $\rho(\infty)$. We then perform a partial trace over the SSET Hilbert space to obtain the reduced density matrix for the resonator alone, $\rho_R(\infty) = \mathrm{Tr}_{\rm SSET}\left[\rho(\infty)\right]$. $\rho_R(\infty)$ contains the full information about the steady-state of the resonator, but further methods are required to visualise the solution and ultimately characterize the state. The first method we use is the Wigner function [72]. This is a quasi-probability distribution in position-momentum space and is defined by [73],

$$W(x,p) \equiv \frac{1}{2\pi\hbar}\int_{-\infty}^{\infty}\left\langle x+\frac{1}{2}y\right|\rho_R(\infty)\left|x-\frac{1}{2}y\right\rangle e^{ipy/\hbar}dy \tag{3.1.1}$$

The Wigner function is not a true probability distribution as it can be negative, which is an indication of non-classical behaviour [23]. For the parameters considered in this thesis the Wigner function is always positive.

Figure 3.1 shows the Wigner functions for the three dynamical states of the resonator that we discuss for the majority of this thesis. Distributions such as that shown in figure 3.1a we refer to as a fixed point state. It is characterized by a single peak in the Wigner function. The state corresponds to fluctuations of the resonator about some average position and momentum. The resonator would be in a state of this kind if it were uncoupled from the SSET and the fluctuations would then be thermal. When coupled to the SSET we can interpret the state as one in which the conditions to drive the resonator into self-sustaining oscillations are not met, which occurs for $\Delta E > 0$ or for insufficient coupling for $\Delta E < 0$.

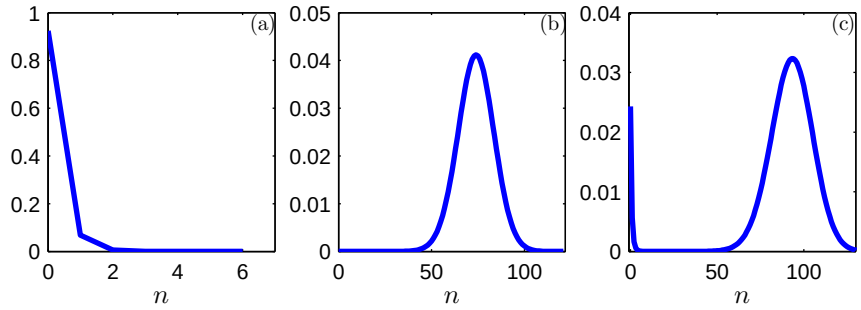

Figure 3.2. $P(n)$ distributions, (a) fixed point, (b) limit cycle and (c) bistable. The parameters are the same as in figure 3.1.

We refer to states that have a Wigner distribution such as figure 3.1b as limit cycle states. These occur for parameters where the SSET drives the resonator into a state of self-sustained oscillations, that is for $\Delta E < 0$ and sufficient coupling. The limit cycle state shares many properties with a laser and is also known as a lasing state, an analogy which is explored in Section 3.7 and Chapter 6.

The final state, which is shown in figure 3.1c, we refer to as a bistable state. It occurs when both fixed point and limit cycle states are stable solutions for a set of parameters. We do not justify our use of the term bistable here. In fact it is clear in figure 3.1c that strictly speaking the system cannot be bistable since there is some noise in the two states. However, as shown in Sections 5.2–5.4 some of the behaviour of the SSET-resonator system can be described in terms of simple model of a two state system. A two state model is valid so long as there is a region in the phase space between the fixed point and limit cycle states where the Wigner function approaches zero. We use the term bistable state more loosely in our description of the system to be any state where there is both a fixed point and limit cycle solution present in the Wigner function of the resonator.

Although useful for a description of the resonator state, the Wigner function is a two dimensional probability distribution for each set of parameters. This reduces its usefulness when characterizing behaviour as parameters are varied. However, it can be seen from figure 3.1 that the various states are circularly symmetric, which suggests that the phase information of the resonator is not required to characterize the state.

A representation that does not include phase information is the distribution of the resonator energy defined as $P(n) = \langle n| \rho_R(\infty) |n\rangle$, where $|n\rangle$ is a Fock state. Figure 3.2 shows the $P(n)$ distributions for the same parameters as the Wigner distributions in figure 3.1. The characterization of states in the $P(n)$ distribution is straightforward. We define the fixed point state as a single peak at $n = 0$, a limit cycle state as a single peak at $n > 0$ and a bistable state as having two peaks one of which is at $n = 0$.

Plots can be made of the $P(n)$ distribution as a parameter is varied (e.g. figure 3.21). However, as we show in Sections 3.3–3.6 the state of the resonator can be inferred quite effectively by looking at just the first two cumulants of the $P(n)$ distribution, which are the average energy, $\langle n \rangle$ and the variance $\langle \bar{n}^2 \rangle$.

3.2 Current and current noise of a SSET

We start by reviewing the characteristics of the SSET in the uncoupled limit, $\kappa \to 0$. The current, $\langle I \rangle^{\kappa=0}$, and zero frequency Fano factor of the current noise, $F_I^{\kappa=0}(0)$, for a SSET tuned to the JQP resonance are given by [17, 47],

$$\langle I \rangle^{\kappa=0} = \frac{2eE_J^2\Gamma}{4\Delta E^2 + \hbar^2\Gamma^2 + 3E_J^2}, \tag{3.2.1}$$

$$F_I^{\kappa=0}(0) = 2 - \frac{8E_J^2\left(E_J^2 + 2\hbar^2\Gamma^2\right)}{\left(4\Delta E^2 + \hbar^2\Gamma^2 + 3E_J^2\right)^2}, \tag{3.2.2}$$

and are shown in figure 3.3. The current has a peak at the centre of the resonance $\Delta E = 0$, which has a width determined by Γ and E_J and was discussed previously in Section 2.2.2. Far from resonance $F_I^{\kappa=0}(0)$ has a value of 2. This is because for large detuning the probability to be in the $|2\rangle$ state is always small (it is proportional to the current). Due to the low current the charge is effectively transported in pairs, since the time between the two quasi-particles in each JQP cycle will always be small. Due to the large time between the breaking up of the Cooper pairs each pair is independent and so follows Poissonian statistics. The transport is equivalent to a single tunnel junction with a charge carrier of $2e$. This result is more general and in any transport process that has Poissonian statistics the zero frequency current Fano factor can be used to find the effective charge of the carrier, an example of which is the fractional quantum hall effect [74–76].

Close to the centre of the resonance there is a strong interplay between the coherent transfer of Cooper pairs and the quasi-particle tunnelling which results in a suppression of the noise. The reason being that the probability of the $|2\rangle$ state no longer remains small and so the time it takes for the system to evolve from the $|0\rangle$ state to the $|2\rangle$ state is reflected in a more ordered transport process. This suppression is strongest at the centre of the resonance where the coherent motion of Cooper pairs is most important.

3.3 Frequency regimes of operation

There is a large parameter space for the system that can be explored. We will not attempt to investigate all of this here, but instead try to split the parameter space into smaller regions that can be investigated more closely. As discussed in Section 2.4 we

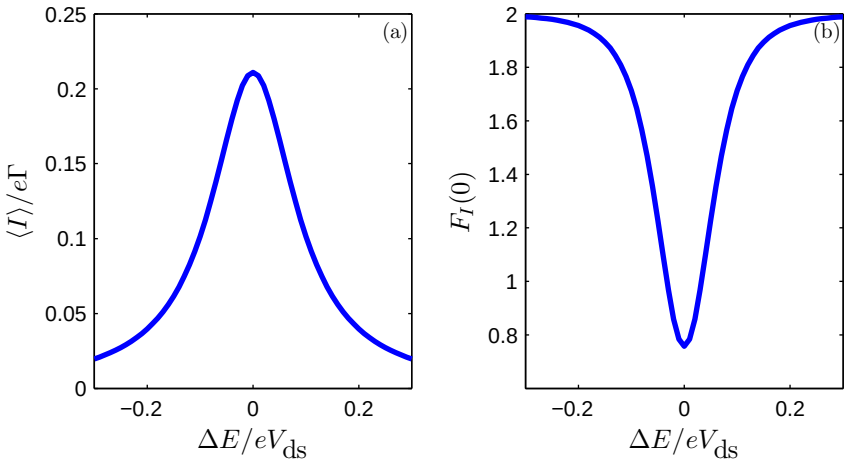

Figure 3.3. current (a) and current noise (b) of a SSET tuned to the JQP resonance. The parameters used are $E_J = 1/16\, eV_{\rm ds}$ and $r = 1$.

use $r = 1$ and $E_J = 1/16\, eV_{\rm ds}$ throughout. We give the time-scales of the system in terms of Γ, which we can think of as the typical time-scale of the SSET since $E_J \lesssim \hbar\Gamma$.

For the resonator parameters we must choose the external damping, $\gamma_{\rm ext}$, to be somewhat larger than what would be expected in experiment in order to ensure the resonator can be described by a limited number of energy states. For the frequency of the resonator we identify three regimes in comparison to the time-scale of the SSET. These are where $\Omega \gg \Gamma$, where $\Omega \ll \Gamma$ and where $\Omega \simeq \Gamma$. In this section we look at how they are connected before we discuss each of them in detail in Sections 3.4, 3.5 and 3.6.

In Section 3.1 it was shown how the $P(n)$ distribution can be used to characterize the state of the resonator. To explore a wide range of parameters it is easier to work with a few cumulants of the $P(n)$ distribution. The full set of cumulants contains the same information as the $P(n)$ distribution, but we do not necessarily need them all to gain a lot of information about the system. In fact the first two, the average energy $\langle n\rangle$ and the variance $\langle \bar{n}^2\rangle = \langle n^2\rangle - \langle n\rangle^2$, where n is the number operator, $n \equiv a^\dagger a$, are sufficient for our purposes. Rather than the variance we plot the resonator Fano factor $F_n = \langle \bar{n}^2\rangle / \langle n\rangle$. Just like the current Fano factor the Fano factor here is an indication of the relationship of the distribution to a Poissonian distribution. A sub-Poissonian resonator Fano factor indicates number squeezing of the resonator distribution, which is a non-classical state [48, 73, 77].

We will look at these moments as a function of the detuning, ΔE, and the resonator frequency in relation to the SSET time-scale, Ω/Γ. Figure 3.4 provides an overview of how the resonator behaves in terms of the average occupation number $\langle n\rangle$. The average

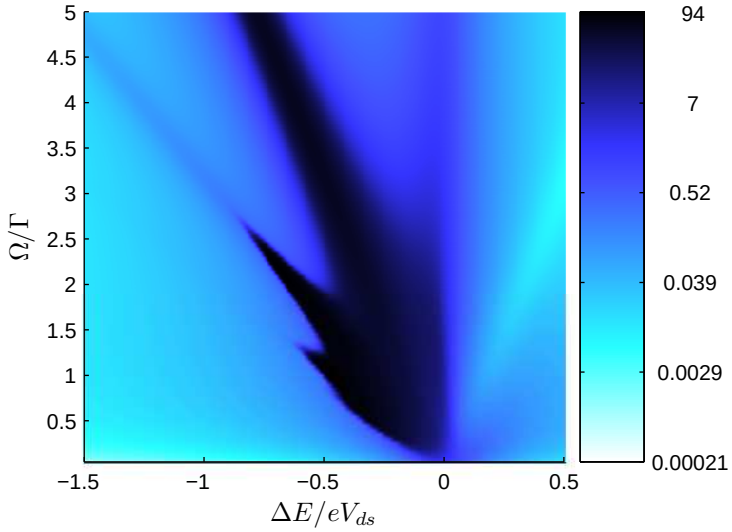

Figure 3.4. Average energy, $\langle n \rangle$, of the resonator as a function of the detuning from resonance and resonator frequency for $\kappa = 0.005$, $E_J = 1/16\, eV_{\rm ds}$, $\gamma_{\rm ext} = 8 \times 10^{-4}\,\Gamma$, $r = 1$ and $\bar{n}_{\rm ext} = 0$. Colours are on a $\log_{10}$ scale.

energy of the resonator is $\hbar\Omega \langle n \rangle$, so we also refer to $\langle n \rangle$ as the average energy. For negative detuning large values of $\langle n \rangle$ are seen, which correspond to the driving of the resonator into limit cycle states. From the average energy it is not clear where the transitions occur or how they occur. Generally we see two kinds of transition. The most common is a continuous transition, where the system evolves smoothly between dynamical states. The second is a discontinuous transition where the system changes state via a bistability and we see a rapid change in the state.

The location of the transitions and what type they are is indicated quite faithfully by the resonator Fano factor, F_n, as shown in figure 3.5. It can be seen that this has a peak around the region of large $\langle n \rangle$. The peak to the left of the central limit cycle region is rather large compared to the peak on the right of the region. This large peak corresponds to the bistable region and elsewhere we have a continuous transition. Other features of the plot will be explained in the following sections. The location and nature of the transition can be confirmed by use of the $P(n)$ distribution.

We can compare the resonator moments with the current and current noise for the same parameters as shown in figures 3.6 and 3.7. Broadly speaking $\langle I \rangle$ shares many similar features with $\langle n \rangle$ and $F_I(0)$ with F_n. We will discuss further the extent to which this is true by looking at the three frequency regimes in more detail.

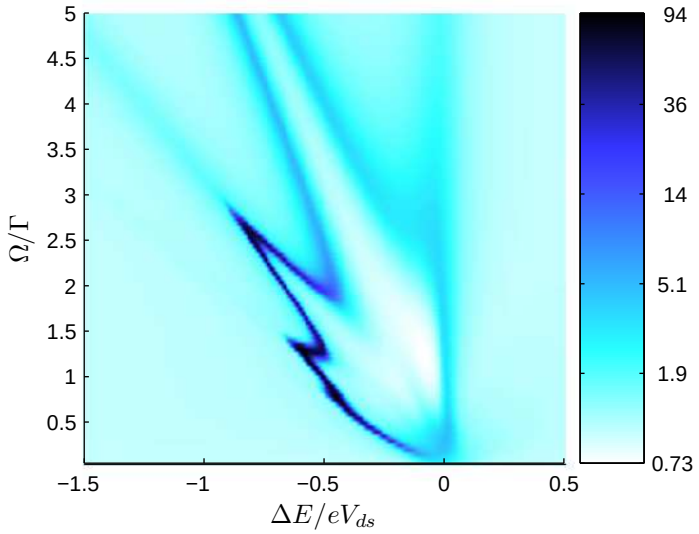

Figure 3.5. Resonator Fano factor, F_n, as a function of the detuning from resonance and resonator frequency for the same parameters as figure 3.4. Colours are on a $\log_{10}$ scale.

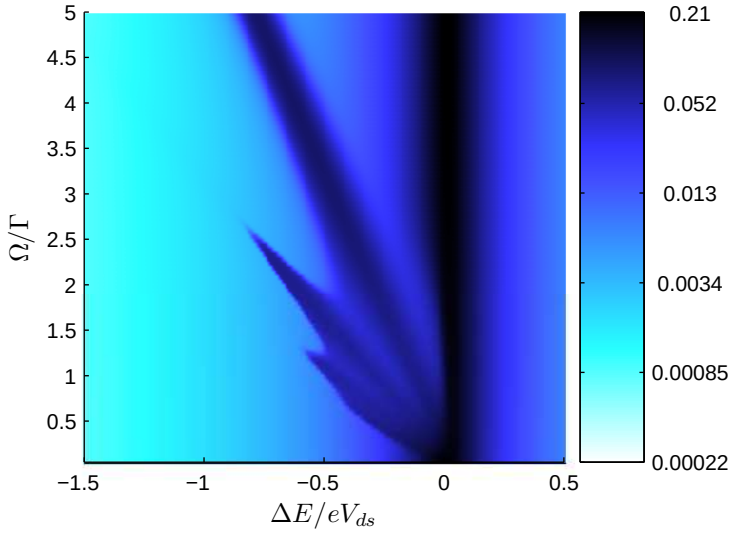

Figure 3.6. Average SSET current, $\langle I \rangle$, as a function of the detuning from resonance and resonator frequency for the same parameters as figure 3.4. Colours are on a $\log_{10}$ scale.

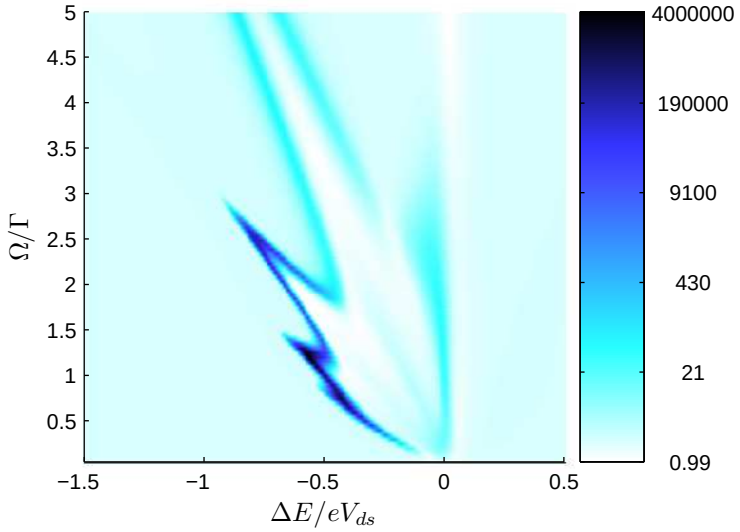

Figure 3.7. Current noise, $F_I(0)$, as a function of the detuning from resonance and resonator frequency for the same parameters as figure 3.4. Colours are on a $\log_{10}$ scale.

3.4 High frequency resonator $\Omega \gg \Gamma$

In the high frequency regime discrete peaks are seen in $\langle n \rangle$ for $\Delta E < 0$, as shown in figure 3.4. These correspond to resonant absorption of energy by the resonator. Less clear are the dips in $\langle n \rangle$ that are observed for $\Delta E > 0$, which correspond to the resonant emission of energy by the resonator i.e. the resonator can be cooled here if the external temperature is large [18, 19]. For the weak coupling values that we consider here, the resonances can be located by the matching of the resonator frequency to a multiple of the eigenenergy of the SSET.

$$k\hbar\Omega = \pm\sqrt{\Delta E^2 + E_J^2}, \tag{3.4.1}$$

where k is a non-zero integer and the sign on the right hand side should be the same as the sign of ΔE, so that resonances for $k < 0$ correspond to driving of the resonator. For large Ω we will have $\Delta E \gg E_J$ at these resonances and so their location is almost entirely determined by ΔE.

To see in more detail the effect of this resonance on the resonator state, figure 3.8 shows $\langle n \rangle$, F_n, $\langle I \rangle$ and $F_I(0)$ around the $k = -1$ resonance as ΔE and the coupling, κ, are varied. From figure 3.8 it can be seen that as the coupling is increased the system undergoes a transition, which is from a fixed point to a limit cycle state. The limit cycle region grows for larger couplings to occur further from the exact resonance condition.

The value of $\langle n \rangle$ indicates the size of the limit cycle, which grows with the coupling strength and is largest on resonance. However, the value of $\langle n \rangle$ only gives an indication of where a transition occurs as it increases steadily through the transition.

F_n is better indicator of the position of the transition as it is strongly peaked at the transition. To move from a fixed point state to a limit cycle state involves a transition through a state with a large variance. This transition can occur in two ways. The first is a bistable transition where there are two peaks in the $P(n)$ distribution. A bistable state must have a high variance since $\langle n \rangle$ will be somewhere in between the peaks. The second type of transition is a continuous transition where the fixed point state smoothly evolves to a limit cycle state with a small amplitude which then grows progressively as we move further into the limit cycle region. During the transition we will go through states which have the bell shape of figure 3.2b but at small amplitude so that there will be a sharp cut-off in the distribution at $n = 0$, an example of which is shown in figure 3.9. This type of state will also have a large variance although smaller than the bistability.

In the limit cycle F_n can become very low even becoming sub-Poissonian by dropping below 1 suggesting a non-classical state. The current noise is very similar to F_n and can also become sub-Poissonian. However, there is no direct correlation between $F_n < 1$ and $F_I(0) < 1$ they may occur at the same time or separately [24]. A similar result was obtained in [78] for a SET coupled to a resonator. They found that by changing the bias voltage and the asymmetry of the junctions any combination of sub- and super-Poissonian values of F_n and $F_I(0)$ could be obtained.

The plot of $\langle I \rangle$ takes a very similar form to that for $\langle n \rangle$. Indeed a plot of $\langle I \rangle$ / $\langle n \rangle$ shows that, to a good approximation, there is a constant multiplier relating the two within the limit cycle region as shown by figure 3.10. The factor can be found by a simple argument due to energy conservation. In order for a Cooper pair to move from the lead to the island it must dissipate an amount of energy $\sqrt{\Delta E^2 + E_J^2} \simeq |\Delta E|$. Without the coupling to the resonator the current at this large detuning is negligibly small. We can therefore assume that the energy is entirely absorbed by the resonator. The rate of energy gain by the resonator is therefore, $\frac{\langle I \rangle}{2e}|\Delta E|$. In the steady-state this must be balanced by the energy loss of the resonator due to damping by the environment, which occurs at a rate $\gamma_{ext}\hbar\Omega \langle n \rangle$. We therefore expect the relationship,

$$\langle I \rangle = \frac{\hbar\Omega}{|\Delta E|} 2e\gamma_{ext} \langle n \rangle \simeq \frac{2e\gamma_{ext}}{|k|} \langle n \rangle , \tag{3.4.2}$$

where we have used the resonance condition given by equation 3.4.1. It can be seen in figure 3.10 that this is indeed the case.

A peak in $\langle n \rangle$ is also seen in figure 3.4 at $\Delta E = 0$, but this has a different origin. It is due to heating of the resonator by the charge noise on the SSET island and there is no dynamical transition in the state of the resonator. The peak corresponds to the JQP

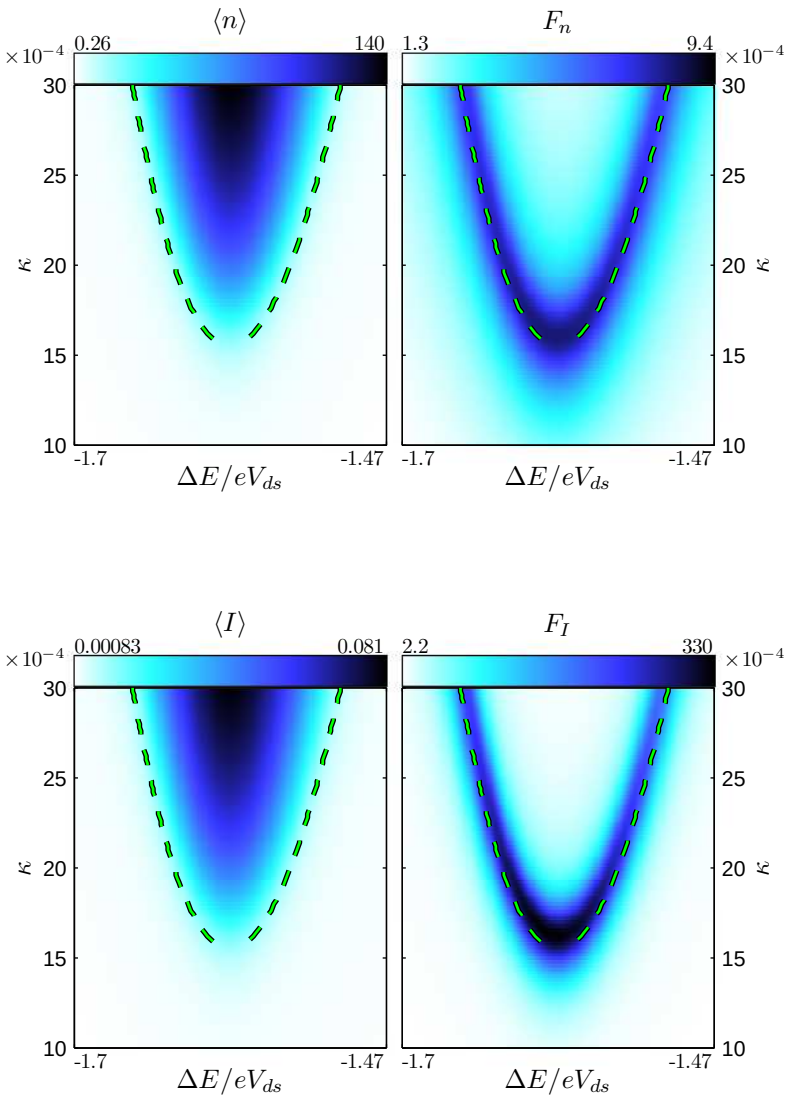

Figure 3.8. $\langle n \rangle$, F_n, $\langle I \rangle$ and $F_I(0)$ as a function of the detuning from resonance and coupling strength for $\Omega = 10\,\Gamma$, $E_J = 1/16\,eV_{\rm ds}$, $\gamma_{\rm ext} = 3\times10^{-4}\,\Gamma$, $r = 1$ and $\bar{n}_{\rm ext} = 0$. The dashed line indicates the transition in dynamical state from fixed point to limit cycle via a continuous transition as the coupling is increased.

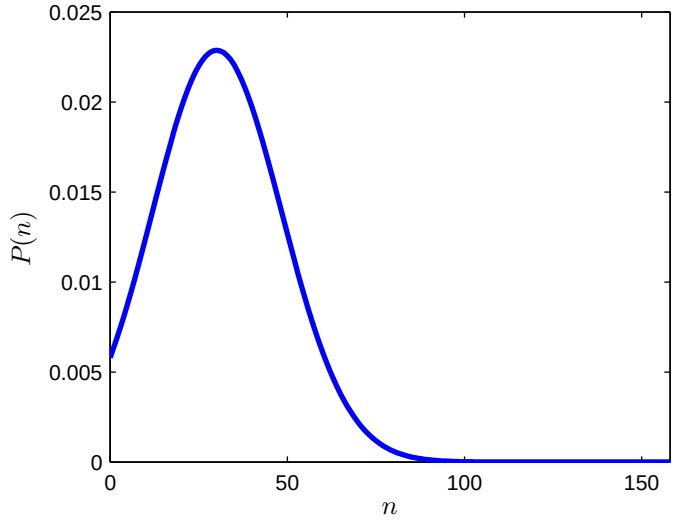

Figure 3.9. $P(n)$ distribution for a continuous transition for $\Delta E = -1.59$ and $\kappa = 1.3 \times 10^{-3}$, with the other parameters the same as figure 3.8.

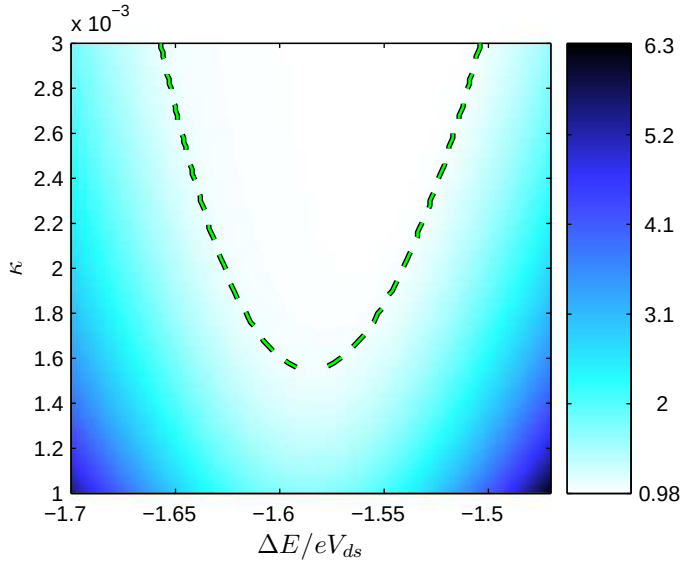

Figure 3.10. $\langle I \rangle / 2e\Gamma \langle n \rangle \gamma_{ext}$ as a function of the detuning from resonance and coupling strength. The parameters are the same as figure 3.8. The dashed line indicates the transition from fixed point to limit cycle state as the coupling is increased.

peak seen in the current in figure 3.6. We will discuss in Chapter 4 how the SSET acts as an effective thermal bath for the resonator in the low frequency and low coupling regime.

3.5 Low frequency resonator $\Omega \ll \Gamma$

The resonances described by equation 3.4.1 will have a width related to the coupling, κ, and quasi-particle tunnelling rate, Γ. In the regime $\Omega \ll \Gamma$ the resonances will no longer be distinguishable. Also note that as the frequency is reduced some of the resonances become disallowed. This occurs when $k\hbar\Omega < E_J$ but will not be observed here since $E_J < \hbar\Gamma$.

Transfer of energy between the SSET and resonator still occurs in this regime with the direction given by the sign of ΔE but is now non-resonant [20]. Figure 3.11 shows the average energy, $\langle n \rangle$, as the detuning and coupling are varied. The transitions between the three different dynamical states of the resonator are indicated by dashed lines in the figure. For $\Delta E < 0$ energy is transferred to the resonator and for strong enough coupling the resonator is driven into the limit cycle state which grows in size as ΔE becomes more negative. For $\kappa \gtrsim 0.0011$ when ΔE is sufficiently negative ($\Delta E \simeq -0.15\, eV_{\rm ds}$) the resonator enters the bistable regime and then undergoes a transition back to the fixed point state in which the limit cycle disappears abruptly [23].

Unlike the high frequency case there is not a strong correspondence between $\langle n \rangle$ and $\langle I \rangle$ as can be seen by comparing figures 3.11 and 3.12. In fact the current is always dominated by the JQP current peak of the SSET. There is some modification, however, which can be seen more clearly by subtracting off the background (uncoupled) current as given by equation 3.2.1, which is what we do in Chapter 4.

As in the high frequency case, F_n is peaked around the transitions between the fixed point and limit cycle states, figure 3.13. The strongest feature occurs in the vicinity of the bistable region. The peak at the continuous transition is not as clear as the $\Omega \gg \Gamma$ case.

F_n can be compared with the zero frequency current noise shown in figure 3.14 as before. For weak coupling a dip can be seen in $F_I(0)$ along the $\Delta E = 0$ line, which is due to the suppression of the current noise present in the uncoupled case (figure 3.3). For stronger coupling, peaks are seen at the transitions as seen in the F_n plot. However, the correspondence between $F_I(0)$ and F_n is not as strong as for the high frequency case. In particular we see a minimum in $F_I(0)$ to the right of the bistable region that extends down to zero coupling. This feature will be explained in Section 4.5, but here it demonstrates that the zero frequency noise contains more information about the system than just measuring average properties or moments.

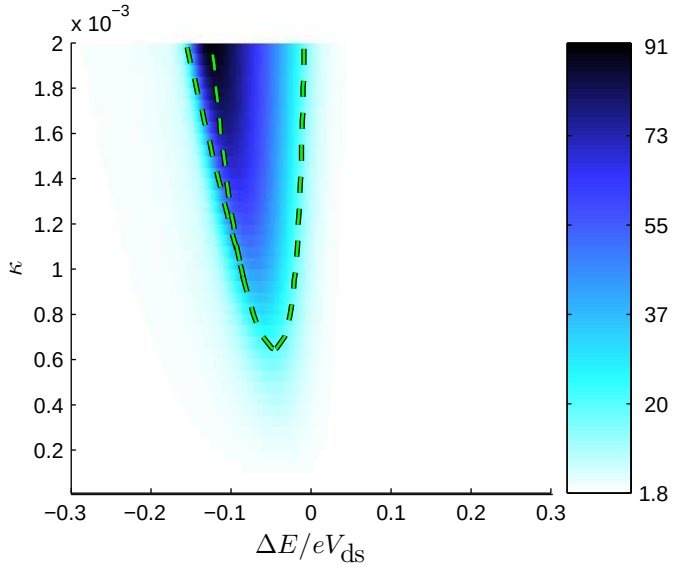

Figure 3.11. Average energy of the resonator as a function of the detuning from resonance and coupling strength for $\Omega = 0.12\,\Gamma$, $E_J = 1/16\,eV_{\rm ds}$, $\gamma_{\rm ext} = 1 \times 10^{-4}\,\Gamma$, $r = 1$ and $\bar{n}_{\rm ext} = 2$. The dashed lines indicate transitions between dynamical states: for most of the range considered the resonator is in the fixed point state, but for large enough coupling a transition to the limit cycle state occurs close to the centre of the resonance. The bistable region is the smallest and occurs for $\kappa > 0.0011$ and $\Delta E \simeq -0.15\,eV_{\rm ds}$.

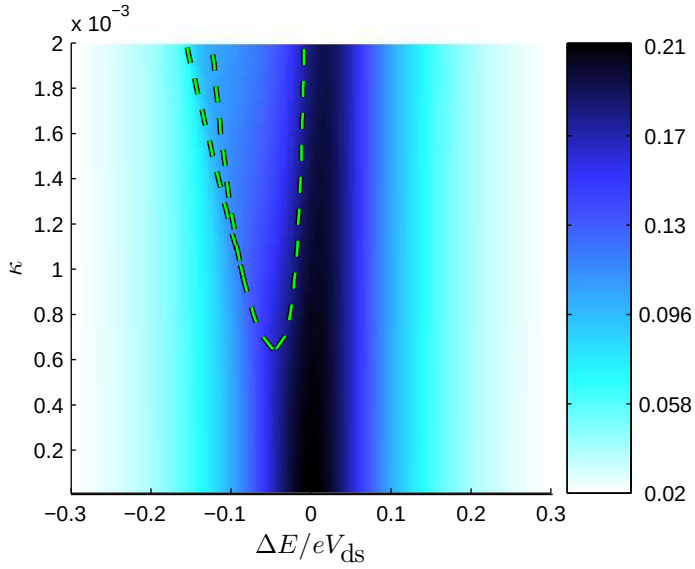

Figure 3.12. Current through the SSET as a function of the detuning from resonance and coupling strength. The dashed lines indicate transitions in the resonator's state and the parameters are the same as in figure 3.11.

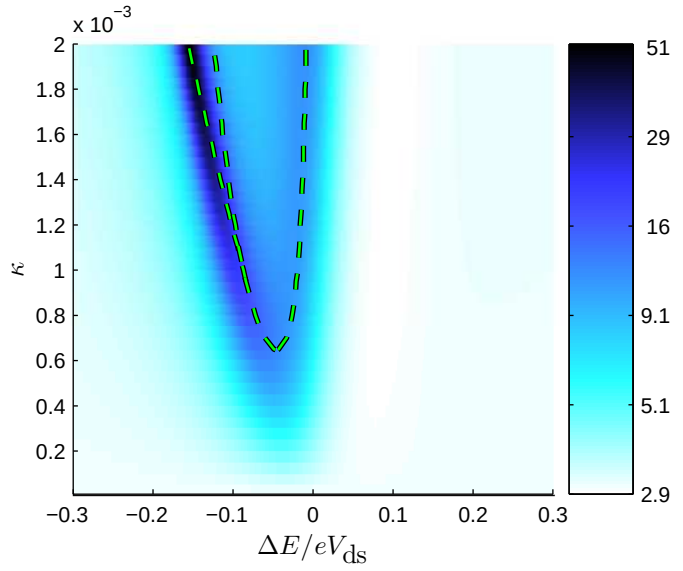

Figure 3.13. Resonator Fano factor, F_n as a function of the detuning from resonance and coupling strength. The dashed lines indicate transitions in the resonator's state and the parameters are the same as in figure 3.11 and the colours are on a $\log_{10}$ scale.

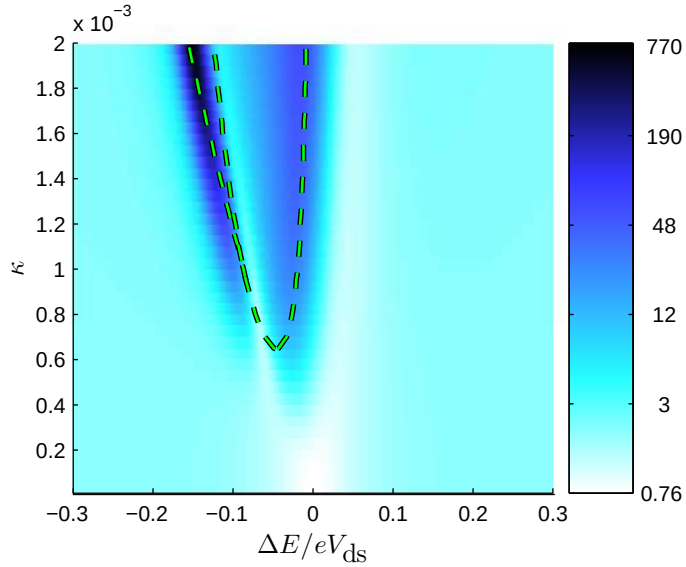

Figure 3.14. Current noise, $F_I(0)$, as a function of the detuning from resonance and coupling strength. The dashed lines indicate transitions in the resonator's state and the parameters are the same as in figure 3.11 and the colours are on a $\log_{10}$ scale.

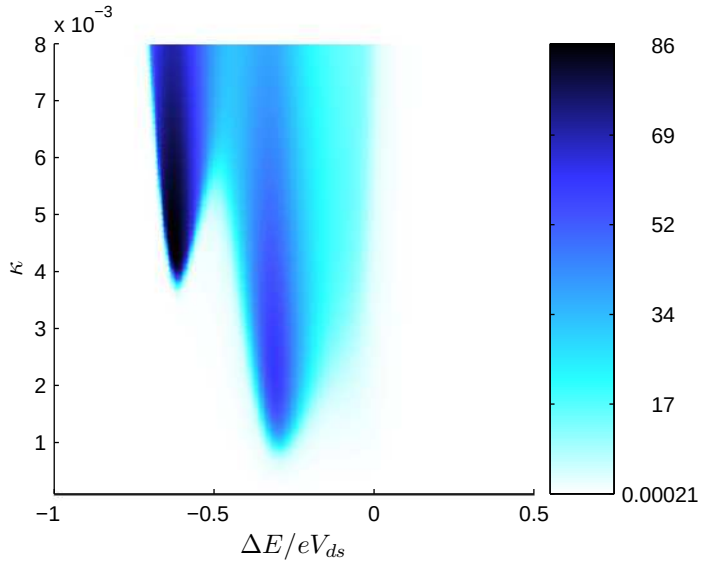

Figure 3.15. Average energy of the resonator as a function of the detuning from resonance and coupling strength for $\Omega = 2\,\Gamma$, $E_J = 1/16\,eV_{\rm ds}$, $\gamma_{\rm ext} = 8 \times 10^{-4}\,\Gamma$, $r = 1$ and $\bar{n}_{\rm ext} = 0$.

3.6 Strongly interacting regime $\Omega \sim \Gamma$

The final operating regime we consider for the device is where $\Omega \sim \Gamma$. At this point the matching of the electrical and mechanical time-scales leads to a relatively strong mutual interaction.

Figure 3.15 show the average energy of the resonator as the detuning and coupling are varied. The resonances corresponding to the absorption of one or two photons ($k = -1$ and $k = -2$ in equation 3.4.1) can clearly be seen in the figure. The $k = -2$ resonance requires a stronger coupling than the $k = -1$ resonance to be allowed since it is a higher order process. Figure 3.16 shows the current for the same parameters. Peaks are seen in the current due to the same resonances as in $\langle n \rangle$. An additional peak is seen due to the JQP peak of the SSET. The JQP current peak can be seen to be modified more strongly as the coupling is increased. The current for the $k = -1$ and $k = -2$ resonances can be seen to be approximately equal. In contrast the average energy of the resonator is larger for the $k = -2$ resonance. This can be understood qualitatively from equation 3.4.1. The equation states that if the current is the same at the $k = -1$ and $k = -2$ resonances then the average energy should be twice as big for the $k = -2$ resonance, which is seen to be the case. However, it is not understood why the two currents are the same.

Figures 3.17 and 3.18 show F_n and $F_I(0)$ respectively. A strong enhancement is seen in both these quantities around the resonant peaks. For the $k = -1$ peak this

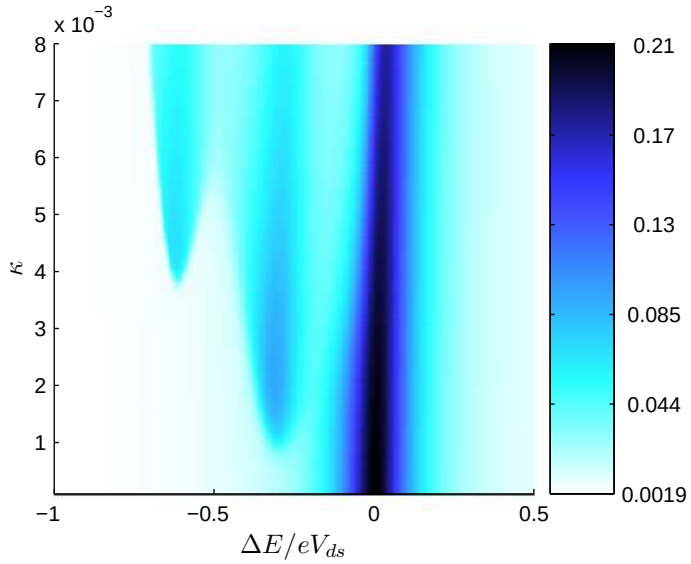

Figure 3.16. Current as a function of the detuning from resonance and coupling strength for the same parameters as figure 3.15.

corresponds to a continuous transition from fixed point to limit cycle state. For the $k = -2$ peak the noise is much larger at the transition and corresponds to a bistable transition. Evidence of the $k = -3$ resonance is also seen in the noise although the coupling is not sufficiently strong to observe a feature in $\langle n \rangle$ or $\langle I \rangle$. The plots of F_n and $F_I(0)$ are generally in agreement with two notable exceptions. For $\Delta E \simeq -0.2$ and $\kappa \simeq 2 \times 10^{-3}$ a peak is seen in F_n that is not present in $F_I(0)$. A similar feature was also observed in the low frequency case and will be explained in Section 4.5. Also within the $k = -1$ resonance F_n can be seen to reduce on resonance to a sub-Poissonian value. However, a peak is seen in $F_I(0)$ on the resonance. We will return to this feature in Section 6.3.

3.7 Analogy with a micromaser

The instabilities seen in this system are similar to those seen in quantum optical systems. In particular we find close analogies with the micromaser system [22, 23]. The micromaser [79] consists of a superconducting cavity resonator through which a beam of two level atoms prepared in the excited state is sent. The beam is of low intensity so that only one atom is in the cavity at any one time. While in the cavity the atoms can exchange energy with the resonator and so excite or cool it when on resonance. This is analogous to the SSET resonator system where the Cooper pairs are transported through the system one at a time and so play the role of the atoms.

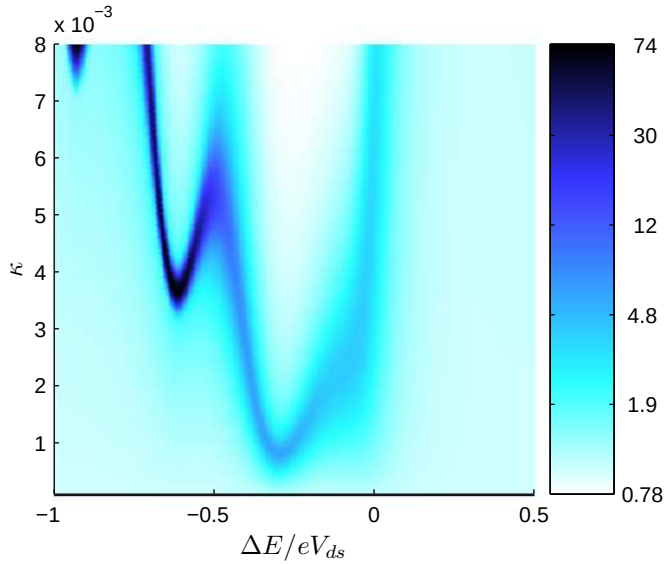

Figure 3.17. Resonator Fano factor, F_n as a function of the detuning from resonance and coupling strength. The parameters are the same as in figure 3.15 and the colours are on a $\log_{10}$ scale.

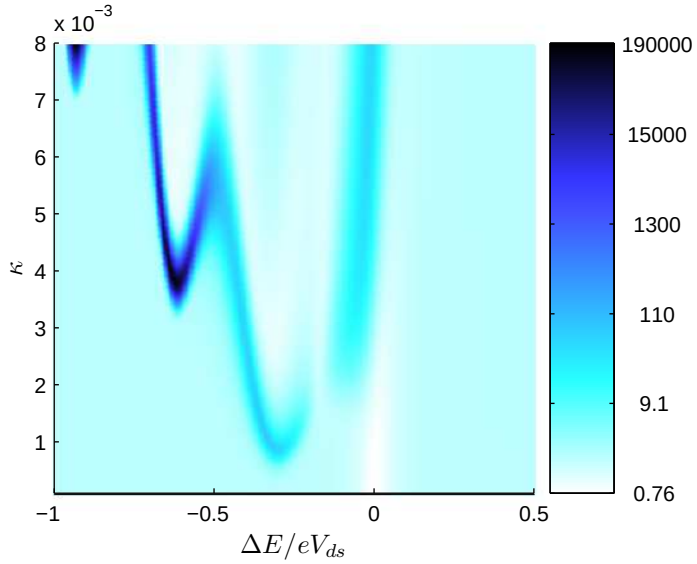

Figure 3.18. Current Fano factor, $F_I(0)$, as a function of the detuning from resonance and coupling strength. The parameters are the same as in figure 3.15 and the colours are on a log_{10} scale.

There is, however, an important difference between the two systems. In the micromaser the rate at which the atoms travel through the cavity is controlled externally and so is not influenced by the interaction with the resonator. In our solid state system, however, the back-action of the resonator on the SSET modifies the current. This makes the system more complex, but also allows us to use the current as a probe of the behaviour of the system, which cannot be done in the micromaser.

A series of dynamical transitions in the resonator state occur in the micromaser as the coupling between the atoms and cavity is increased as shown in [79]. The transitions are accompanied by jumps in the average energy of the resonator that correspond to the formation of new stable limit cycle states. There is also an accompanying peak in the variance of the resonator energy at the transition [79]. The transitions become sharper as the number of atoms to pass through the cavity during the cavity lifetime is increased. The transitions also become less sharp at higher coupling strengths.

We can carry out a similar analysis for the SSET-resonator system. The equivalent of the rate of atoms through the cavity is the current and the lifetime of the cavity mode is given by the external damping. Unlike the micromaser we cannot easily increase the current without modifying the interaction between the SSET and resonator. It is therefore easier to alter the external damping of the resonator, although this will also cause a shift in the position of the transitions. We are also limited by the finite number of resonator states and so cannot reach the limit where the transitions become sharp.

In figure 3.19 the normalized average energy is shown as the coupling is varied for three values of the external damping. As the coupling is increased the resonator first goes through a transition from fixed point to limit cycle state to reach a maximum value. Further increasing the coupling causes the average energy to reduce until an increase is seen corresponding to the formation of a second limit cycle state. The increase in the average energy becomes sharper as the damping is reduced. The behaviour is also observed in the variance of the energy as shown in figure 3.20. The first peak is at the transition from fixed point to limit cycle state. The second peak becomes much more pronounced as the external damping is reduced. Also note that in-between the two peaks $F_n < 1$ indicating a sub-Poissonian distribution in the resonator energy as previously observed [23].

The nature of the transitions is made clearer by observing the change in the $P(n)$ distribution as the coupling is varied. This is shown for the smallest and largest values of $\gamma_{\rm ext}$ from figure 3.19, in figures 3.21 and 3.22 respectively. It can be seen in the figures that as the coupling is increased more stable limit cycle states of the system are formed. For small $\gamma_{\rm ext}$, as in figure 3.21, it can be seen that the first limit cycle state vanishes soon after the second is formed. It is for this reason that the jump in $\langle n \rangle$ is seen. For the larger value of $\gamma_{\rm ext}$, shown in figure 3.22, and for the further transitions in figure 3.21, it can be seen that the limit cycle states co-exist and so a sharp jump in $\langle n \rangle$ is not seen.

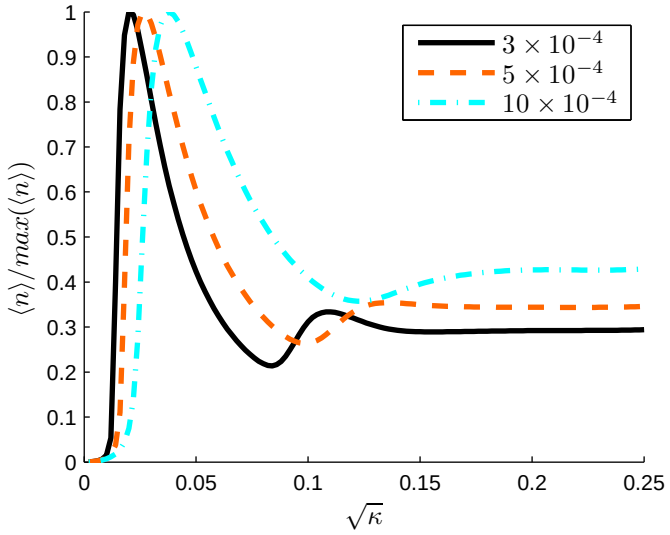

Figure 3.19. Normalized average energy of the resonator as a function of the coupling for 3 values of the external damping. The other parameters are $\Delta E = -0.1\, eV_{\rm ds}$, $\Omega = \Gamma$, $E_J = 1/16\, eV_{\rm ds}$, $r = 1$ and $\bar{n}_{\rm ext} = 0$. A transition is seen for $\sqrt{\kappa} \simeq 0.12$ that becomes sharper for reduced $\gamma_{\rm ext}$

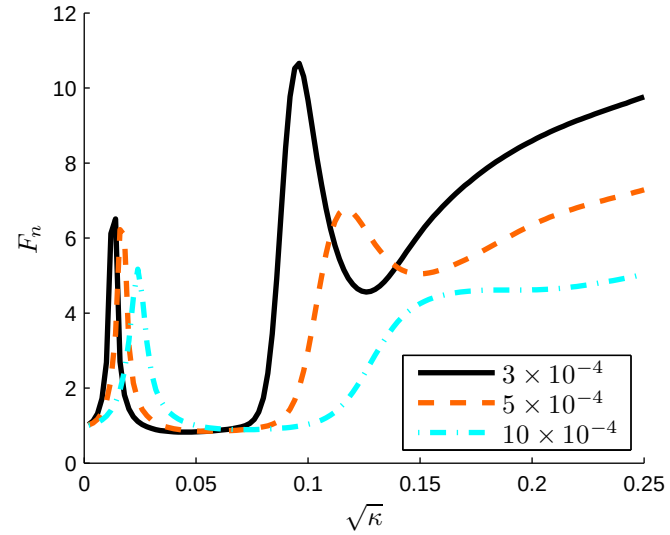

Figure 3.20. F_n as a function of the coupling for 3 values of the external damping. The parameters are the same as figure 3.19. A transition is seen for $\sqrt{\kappa} \simeq 0.12$ that becomes sharper for reduced $\gamma_{\rm ext}$

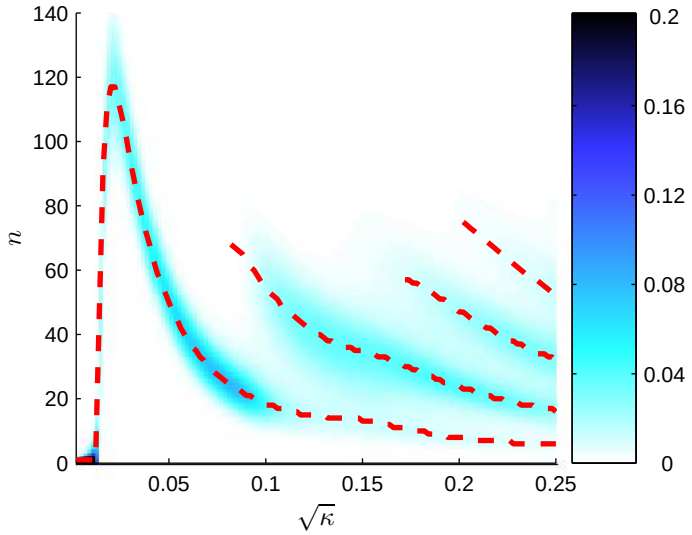

Figure 3.21. Changing $P(n)$ distribution as a function of the coupling for $\gamma_{\text{ext}} = 3 \times 10^{-4}\,\Gamma$. The other parameters are given in figure 3.19. Dashed lines indicate the locations of peaks in the distribution.

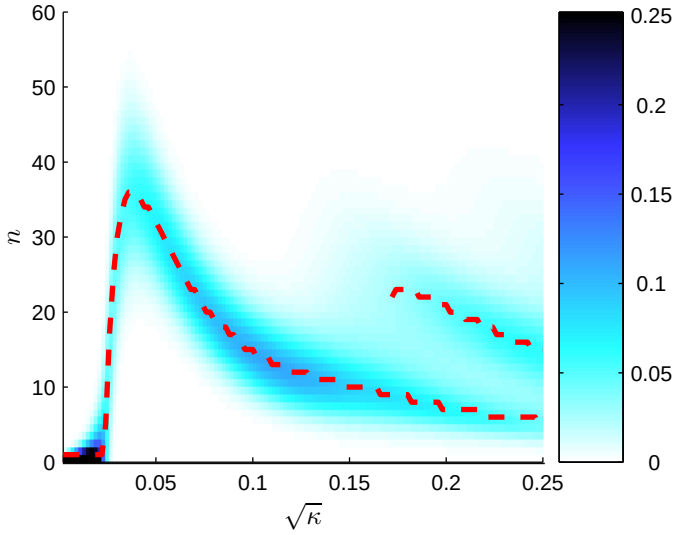

Figure 3.22. Changing $P(n)$ distribution as a function of the coupling for $\gamma_{\text{ext}} = 0.001\,\Gamma$. The other parameters are given in figure 3.19. Dashed lines indicate the locations of peaks in the distribution.

The origin of the co-existing limit cycle states was explained in terms of the semi-classical dynamics of the system in [22]. The driving of the resonator by the SSET can be described by an effective damping rate. A stable limit cycle solution occurs when this effective damping matches the external damping by the resonator bath. The effective damping is an oscillating function with the amplitude of the resonator and so a number of solutions can co-exist.

Chapter 4

Resonator in a Thermal State

In the previous chapter we gave an overview of the behaviour of the system for a range of parameters. In this chapter we remain in the regime of weak coupling between the SSET and resonator so that the resonator remains in the fixed point state throughout. In this regime the SSET acts as an effective thermal bath for the resonator as described in Section 4.1. We focus on just one of the frequency regimes introduced in the previous chapter, that of $\Omega \ll \Gamma$, where the effective bath parameters have a simple analytical form. When this is the case the current and current noise can be described using much simpler models than the solution of the full master equation. The first of these, which is described in Section 4.2, calculates the current and current noise by assuming that the gate voltage fluctuates with statistics given by the thermal bath model of Section 4.1. This simple model accurately describes the current, but not the current noise. A full description of the system in this regime can be obtained from a set of mean field equations as shown in Section 4.3. The mean field equations for this system do not form a closed set, but they can be truncated with little error in the thermal regime by making sensible approximations. The final model, described in Section 4.4, attempts to capture the part of the current noise due to the dynamics of the resonator. Finally, in Section 4.5, the finite frequency current noise in this regime is calculated and to what extent its behaviour is captured by the simple models is discussed.

4.1 SSET as an effective thermal bath

For sufficiently weak coupling, the steady-state of the resonator can be described analytically. Based on the Born-Markov master equation that was described in Section 2.4 the SSET degrees of freedom can be traced over and the state of the resonator found [18]. Alternatively general linear response methods [80] can be applied to the system to describe the resonator [19].

The result from these two approaches is that for weak coupling and small mechan-

ical displacement the SSET acts on the resonator as an effective thermal bath. The thermal bath is characterized by three parameters, an effective damping, γ_{SSET}, an effective occupation number, $\bar{n}_{\mathrm{SSET}}$, and a renormalization of the resonator frequency to Ω_R. Using either the Born-Markov or linear response methods the values of these parameters in the regime $\Omega \ll \Gamma$ are [18, 19],

$$\gamma_{\mathrm{SSET}} = \frac{16 m x_s^2 \Omega^4 E_J^2 \Delta E}{\Gamma} \left[\frac{4\Delta E^2 + 13\hbar^2\Gamma^2 + 10E_J^2}{\left(4\Delta E^2 + \hbar^2\Gamma^2 + 3E_J^2\right)^3} \right], \tag{4.1.1}$$

$$\bar{n}_{\mathrm{SSET}} = \frac{\hbar^2\Gamma^2 + 4\Delta E^2}{16\Delta E \hbar \Omega}, \tag{4.1.2}$$

$$\Omega_R^2 = \Omega^2 \left(1 - \frac{48 m \Omega^2 x_s E_J^2 \Delta E}{\left(4\Delta E^2 + \hbar^2\Gamma^2 + 3E_J^2\right)^2} \right). \tag{4.1.3}$$

We focus on the $\Omega \ll \Gamma$ regime here where the parameters have the simple form above. However, the effective thermal bath description can be extended to all frequency regimes, so long as the coupling is weak [81].

In the same manner as a resonator coupled to a standard thermal bath, the steady-state of the resonator will have the form of a thermal state (i.e. the Wigner function will take a Gaussian form). In practice there is also the thermal bath due to the resonators surroundings and the average occupation number of the resonator, $\bar{n}$, is found from a weighted average of the two baths [57],

$$\bar{n} = \frac{\gamma_{\mathrm{ext}} \bar{n}_{\mathrm{ext}} + \gamma_{\mathrm{SSET}} \bar{n}_{\mathrm{SSET}}}{\gamma_{\mathrm{ext}} + \gamma_{\mathrm{SSET}}}. \tag{4.1.4}$$

The total damping rate of the resonator, γ, is given by a sum of the damping due to the SSET and the external damping due to the resonators surroundings,

$$\gamma = \gamma_{\mathrm{ext}} + \gamma_{\mathrm{SSET}} \tag{4.1.5}$$

In figure 4.1 the shape of γ_{SSET} and $\bar{n}_{\mathrm{SSET}}$ are shown as a function of the detuning. γ_{SSET} is negative for $\Delta E < 0$ and so in this region the total damping of the resonator is reduced. For sufficiently strong coupling the total damping can become negative and this weak coupling description clearly breaks down since the fluctuations in the position of the resonator are no longer small. To ensure that the model accurately describes the state of the resonator we require that $\gamma_{\mathrm{ext}} > |\gamma_{\mathrm{SSET}}|$. $\bar{n}_{\mathrm{SSET}}$ is also negative for $\Delta E < 0$ so the product $\gamma_{\mathrm{SSET}} \bar{n}_{\mathrm{SSET}}$ appearing in equation 4.1.4 is always positive. When $\Delta E < 0$ the coupling with the SSET must increase the value of $\bar{n}$ above $\bar{n}_{\mathrm{ext}}$. However, for $\Delta E > 0$, $\bar{n}$ can be reduced due to the coupling with the SSET and so the resonator can be cooled [18, 19, 21].

The coupling to the SSET also leads to a shift in the average position of the resonator which has a simple relationship to the average charge on the SSET island,

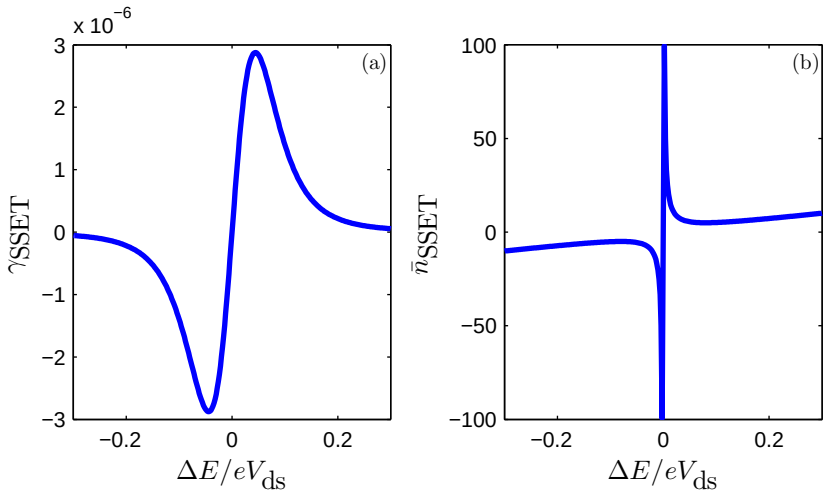

Figure 4.1. (a) γ_{SSET} (b) $\bar{n}_{\mathrm{SSET}}$ as a function of ΔE as calculated from equations 4.1.1 and 4.1.2. Parameters are $\kappa = 1 \times 10^{-4}$, $\Omega = 0.05\,\Gamma$, $E_J = 1/16\,eV_{\mathrm{ds}}$, $\gamma_{\mathrm{ext}} = 1 \times 10^{-4}\,\Gamma$ and $\bar{n}_{\mathrm{ext}} = 2$

which is in turn proportional to the average (steady-state) current flowing through the SSET [18, 22]. The average displacement is given by,

$$\langle x \rangle = -\frac{3x_s}{2e\Gamma} \langle I \rangle . \tag{4.1.6}$$

In Section 4.3 we derive this relationship using the mean field equations.

For weak SSET-resonator coupling the changes in the transport properties of the SSET due to the resonator are relatively small so it makes sense to examine just the difference between the values for the coupled and uncoupled cases. The uncoupled current, $\langle I \rangle^{\kappa=0}$, and zero frequency current Fano factor, $F_I^{\kappa=0}(0)$, were given in equations 3.2.1 and 3.2.2 respectively.

The change in the SSET current due to the coupling with the resonator (calculated numerically) is shown in figure 4.2. We consider a slow resonator $\Omega \ll \Gamma$ and very weak coupling so that although the SSET has quite a strong influence on the resonator state, the resonator nevertheless remains in a thermal state which is well described by equations 4.1.1–4.1.5. From figure 4.2 we see that near the centre of the resonance the current is suppressed by the resonator, but on either side of this there is an enhancement. The current noise is modified in a similar way to the current, but in the opposite sense, as shown in figure 4.3, thus there is an increase in the noise near to the resonance with a decrease on either side.

Although it is relatively easy to calculate the current and current noise numerically it is helpful to develop simple analytical models of the coupled system so that the results can be better understood. The starting point for these models is that a thermal

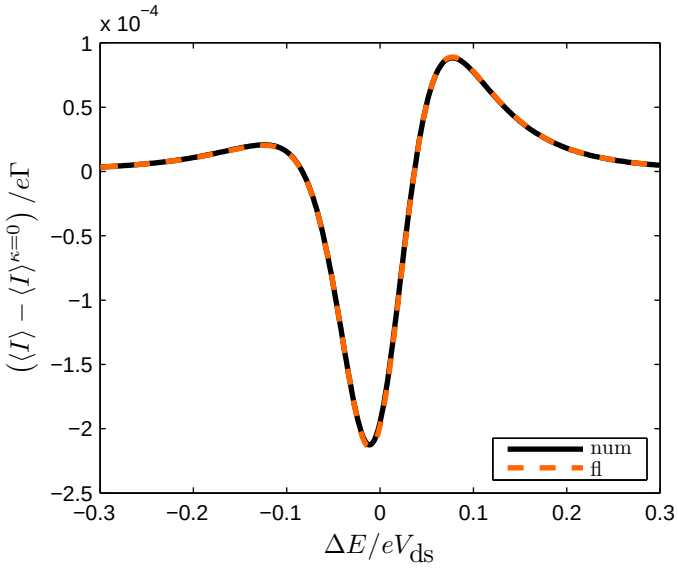

Figure 4.2. Change in current through the SSET as a function of ΔE. The curves are labelled as *num* for the numerical results and *fl* for the change in the current calculated using equation 4.2.3. The parameters used are the same as in figure 4.1. [Note that for these parameters $\bar{n}$ varies from a value of 2 far from resonance to a peak value of 2.28 at $\Delta E = -0.01\, eV_{\rm ds}$. $\gamma_{\rm SSET}/\gamma_{\rm ext}$ has maxima and minima of ± 0.029 at $\Delta E = \pm 0.044\, eV_{\rm ds}$.]

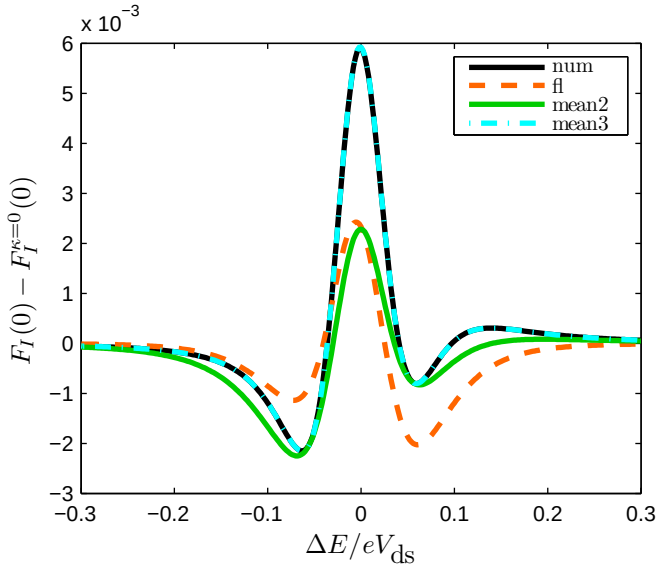

Figure 4.3. Change in the zero frequency current Fano factor of the SSET due to the resonator. The curves are labelled as *num* for the numerical results, *fl* is obtained from equation 4.2.6, *mean2* is calculated using the second order mean field equations and *mean3* using the third order mean field equations. The parameters used are the same as in figure 4.1.

state has a Gaussian distribution in position and momentum space [82]. A Gaussian distribution is entirely described by second order moments, a fact which we can use to our advantage.

4.2 Fluctuating gate model

The simplest way of including the influence of the resonator on the SSET is to include the effect of fluctuations in the position of the resonator on the current [24]. Because the resonator acts as a gate for the SSET island, a shift of the position of the resonator leads to an effective change in the detuning energy ΔE (equation 2.4.3). Hence, when the resonator position fluctuates so will the detuning energy. We can incorporate the effect of the mechanical motion into the expression for the current, equation 3.2.1, by calculating it for a fixed position before averaging over the resonator state, an approach that was also used in [83]. We make the replacement $\Delta E \rightarrow \Delta E + 2m\Omega^2 x_s x$ to obtain the current,

$$\begin{aligned} I(x) &= \frac{2eE_J^2\Gamma}{4\left(\Delta E + 2m\Omega^2 x_s x\right)^2 + \hbar^2\Gamma^2 + 3E_J^2} \\ &= \frac{2eE_J^2\Gamma}{\beta + \alpha(x)} \end{aligned} \tag{4.2.1}$$

where we have defined $\beta \equiv 4\Delta E + \hbar^2\Gamma^2 + 3E_J^2$ and $\alpha(x) = 16m\Omega^2 x_s(\Delta E x + m\Omega^2 x_s x^2)$. Assuming the shift term is small, we perform a Taylor expansion of the current about $\alpha(0) = 0$ to second order.

$$I(x) \simeq I(0) + \alpha \left.\frac{\partial I(x)}{\partial \alpha(x)}\right|_{\alpha(x)=0} + \alpha^2 \left.\frac{\partial^2 I(x)}{\partial \alpha(x)^2}\right|_{\alpha(x)=0}, \tag{4.2.2}$$

and then take the average over the resonator position. Keeping terms up to order x_s^2 we obtain,

$$\begin{aligned} \langle I \rangle_{fl} &= I(0)\left[1 - \frac{16m\Omega^2 x_s}{\beta}\left\{\Delta E \langle x\rangle + m\Omega^2 x_s \langle x^2\rangle \left(1 - \frac{16\Delta E^2}{\beta}\right)\right\}\right] \\ &= I(0)\frac{\beta^2 - 16(m\Omega^2 x_s)^2 \langle x^2\rangle \left(\beta - 16\Delta E^2\right)}{\beta^2 - 48m\Omega^2 x_s^2 \Delta E E_J^2}, \end{aligned} \tag{4.2.3}$$

where the averages are taken over the (Gaussian) steady state probability distribution of the resonator. In the second line we have used equation 4.1.6 to eliminate $\langle x\rangle$. The value of $\langle x^2\rangle \simeq \langle \bar{x}^2\rangle$ is calculated using equation 4.1.4. Although we have eliminated $\langle x\rangle$ we can also approximate it to high accuracy using the uncoupled current in place of the actual current in equation 4.1.6.

It is clear from figure 4.2 that equation 4.2.3 accurately describes the modification

to the current due to the presence of the resonator. Thus in this weak coupling regime where the resonator remains in a thermal state, the modification of the current is simply due to two affects. A shift in the resonator's position gives an asymmetric shape. From equation 4.1.6 this position shift will be negative so from equation 4.2.3 the current will increase for $\Delta E > 0$ and decrease for $\Delta E < 0$. Secondly a smearing out of the JQP current peak due to fluctuations in the resonator position will tend to reduce the current near to the peak and increase it either side. We see from equation 4.2.3 that the decrease will be when $12\Delta E^2 < \hbar^2\Gamma^2 + 3E_J^2$.

For the current noise we naively replace $\Delta E \to \Delta E + 2m\Omega^2 x_s x$ in equation 3.2.2 to obtain,

$$\begin{aligned} S_I(x) &= 4eI(x) - \frac{32e^2E_J^4\Gamma\left(E_J^2 + 2\hbar^2\Gamma^2\right)}{\left(4\left(\Delta E + 2m\Omega^2 x_s x\right)^2 + \hbar^2\Gamma^2 + 3E_J^2\right)^3} \\ &= 4eI(x) - \frac{4e^2E_J^2\Gamma\phi}{\left(\beta + \alpha(x)\right)^3}, \end{aligned} \tag{4.2.4}$$

where $\phi \equiv 8E_J^2\left(E_J^2 + 2\hbar^2\Gamma^2\right)$. As for the current this expression is expanded about $\alpha(0)$ keeping terms up to second order in x_s and then the resonator position averaged over.

$$\begin{aligned} S_{I,I}^{fl}(0) =& 4e\left\langle I\right\rangle_{fl} \\ &- \frac{4e^2E_J^2\Gamma\phi}{\beta^3}\left[1 - \frac{48m\Omega^2x_s}{\beta}\left\{\Delta E\left\langle x\right\rangle - m\Omega^2x_s\left\langle x^2\right\rangle\left(1 - \frac{32\Delta E^2}{\beta}\right)\right\}\right], \end{aligned} \tag{4.2.5}$$

$$\begin{aligned} =& 4e\left\langle I\right\rangle_{fl}\left[1 - \frac{72m\Omega^2x_s^2E_J^2\phi\Delta E}{\beta^4}\right] \\ &- \frac{4e^2E_J^2\Gamma\phi}{\beta^5}\left[\beta^2 - 48\left(m\Omega^2x_s\right)^2\left\langle x^2\right\rangle\left(\beta - 32\Delta E^2\right)\right] \end{aligned} \tag{4.2.6}$$

The modification to the current noise is similar to that of the current in that there is an asymmetry due to a shift in the position of the resonator and a smearing out due to fluctuations in the resonator position. However, since $F_I(0)$ is a dip rather than a peak the changes in the current noise are in the opposite sense.

In contrast to the current, it can be seen from figure 4.3 that for the Fano factor, equation 4.2.6 does not capture the behaviour correctly. Although the qualitative shape is the same with a central peak with dips either side, the curves do not match and the asymmetry of the numerical curve is in the opposite direction to that predicted by the simple model.

The reason for the disagreement in the current noise is that the simple model of a fluctuating gate neglects both the correlations between the electrical and mechanical

motion and the dynamics of the resonator. The current noise (in contrast to the average current) is sensitive to the correlations between the SSET charge and the resonator motion and hence to describe it accurately we need to include them in some way.

4.3 Mean field equations

A straightforward and systematic way to include correlations and information about the resonator dynamics are the mean field equations of the system, namely the equations of motion for the expectation values of the SSET and resonator operators. The mean field equations are generated in turn by multiplying the master equation by an operator (or product of operators) and taking the trace over the full system [22].

For the SSET operators we have the five equations,

$$\langle \dot{p_0} \rangle_t = i\frac{E_J}{2\hbar}\Big(\langle c \rangle_t - \langle c^\dagger \rangle_t \Big) + \Gamma \langle p_1 \rangle_t \,, \tag{4.3.1}$$

$$\langle \dot{p_1} \rangle_t = -\Gamma \langle p_1 \rangle_t + \Gamma \langle p_2 \rangle_t \,, \tag{4.3.2}$$

$$\langle \dot{p_2} \rangle_t = -i\frac{E_J}{2\hbar}\Big(\langle c \rangle_t - \langle c^\dagger \rangle_t \Big) - \Gamma \langle p_2 \rangle_t \,, \tag{4.3.3}$$

$$\langle \dot{c} \rangle_t = \left(-i\frac{\Delta E}{\hbar} - \frac{\Gamma}{2}\right)\langle c \rangle_t + i\frac{E_J}{2\hbar}\Big(\langle p_0 \rangle_t - \langle p_2 \rangle_t \Big) - i\frac{2m\Omega^2 x_s}{\hbar} \langle xc \rangle_t \,, \tag{4.3.4}$$

$$\left\langle \dot{c^\dagger} \right\rangle_t = \left(i\frac{\Delta E}{\hbar} - \frac{\Gamma}{2}\right)\langle c^\dagger \rangle_t - i\frac{E_J}{2\hbar}\Big(\langle p_0 \rangle_t - \langle p_2 \rangle_t \Big) + i\frac{2m\Omega^2 x_s}{\hbar} \langle xc^\dagger \rangle_t \,, \tag{4.3.5}$$

where $\langle O \rangle_t = \mathrm{Tr}\left[O\rho(t)\right]$. The coupling to the resonator appears in the last two of these equations. We can also write down equations of motion for the resonator operators, given here up to second order,

$$\langle \dot{x} \rangle_t = \langle v \rangle_t \,, \tag{4.3.6}$$

$$\langle \dot{v} \rangle_t = -\Omega^2 \langle x \rangle_t - x_s\Omega^2\Big(\langle p_1 \rangle_t + 2\langle p_2 \rangle_t \Big) - \gamma_{ext} \langle v \rangle_t \,, \tag{4.3.7}$$

$$\left\langle \dot{x^2} \right\rangle_t = \langle xv \rangle_t + \langle vx \rangle_t \,, \tag{4.3.8}$$

$$\begin{aligned}\left\langle \dot{v^2} \right\rangle_t = &-\Omega^2\Big(\langle xv \rangle_t + \langle vx \rangle_t \Big) - 2x_s\Omega^2\left(\langle vp_1 \rangle_t + 2\langle vp_2 \rangle_t\right) \\ &- 2\gamma_{ext}\left\langle v^2 \right\rangle_t + \frac{\gamma_{ext}\hbar\Omega}{m}\left(1 + 2\bar{n}_{ext}\right),\end{aligned} \tag{4.3.9}$$

$$\begin{aligned}\langle \dot{xv} \rangle_t + \langle v\dot{x} \rangle_t = &\, 2\left\langle v^2 \right\rangle_t - 2\Omega^2\left\langle x^2 \right\rangle_t - 2x_s\Omega^2\Big(\langle xp_1 \rangle_t + 2\langle xp_2 \rangle_t \Big) \\ &- \gamma_{ext}\Big(\langle xv \rangle_t + \langle vx \rangle_t \Big).\end{aligned} \tag{4.3.10}$$

From these equations we can derive some useful relationships and obtain equation 4.1.6. From a trace over the charge and right hand junction current operators in the steady-

state (equations 2.7.3 and 2.7.8) we find,

$$\langle Q \rangle = e\left(\langle p_1 \rangle + 2\langle p_2 \rangle\right), \tag{4.3.11}$$

$$\langle I \rangle = e\Gamma\left(\langle p_1 \rangle + \langle p_2 \rangle\right). \tag{4.3.12}$$

Equation 4.3.2 gives that $\langle p_1 \rangle = \langle p_2 \rangle$ in the steady-state so the current and charge are related by,

$$\langle Q \rangle = \frac{3}{2\Gamma}\langle I \rangle. \tag{4.3.13}$$

Then, from equations 4.3.6 and 4.3.7, the relationship between the average position and average charge in the steady-state is established,

$$\langle x \rangle = -\frac{x_s}{e}\langle Q \rangle, \tag{4.3.14}$$

which when combined with equation 4.3.13, leads immediately to equation 4.1.6.

No matter what order we go to the set of mean field equations for the SSET-resonator system never forms a closed set. The equation for $\langle \dot{c} \rangle$ (equation 4.3.4) contains the second order term $\langle xc \rangle$. Calculating the the equation of motion for $\langle xc \rangle$ then introduces a term $\langle x^2 c \rangle$ (see equation C.0.4) and so forth.

One approach to form a closed set of equations is to perform the semi-classical approximation from quantum optics. In this approximation correlations between the SSET and resonator are neglected (atom and field in quantum optics). The replacement $\langle xc \rangle \rightarrow \langle x \rangle\langle c \rangle$ would therefore be made. It is known as the semi-classical approximation since the set of equations now describe a quantum mechanical device coupled to a classical harmonic oscillator. The semi-classical approximation was used to investigate the SSET-resonator system in [22].

In making the semi-classical approximation we remove some of the noise in the system [22, 84]. From the mean field equations it is clear that higher order moments of the resonator such as $\langle x^2 \rangle$ will not be involved. It is essential to include $\langle x^2 \rangle$ since we know from the fluctuating gate model, in the previous section, that it is required to describe the current. The state of the resonator is Gaussian to a very good approximation in the thermal regime. Any third order cumulants of resonator operators must therefore be zero. It therefore seems sensible to extend the approximation to include the correlations of pairs of operators. In analogy to the semi-classical approximation, in which it is assumed that second order cumulants of the system operators are zero, we instead assume that third order cumulants are zero. The resulting replacements are of the kind,

$$\langle x^2 c \rangle_t \rightarrow 2\langle x \rangle_t \langle xc \rangle_t + \left(\langle x^2 \rangle_t - 2\langle x \rangle_t^2\right)\langle c \rangle_t. \tag{4.3.15}$$

Crucially the correlations between products of two operators are retained. Further details of the method and the resulting second order mean field equations are given in

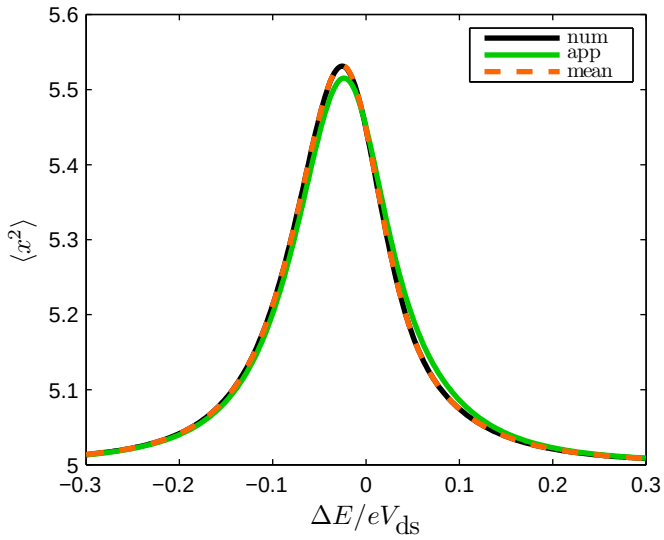

Figure 4.4. Value of $\langle x^2 \rangle$ in the steady-state as given by the full numerical solution (*num*), solving the second order non-linear mean field equations (*mean*) and from the analytical expression in equation 4.1.4 (app). The parameters used are the same as in figure 4.1.

Appendix C.

The resulting set of equations is closed, but is non-linear because of the terms generated by the approximation. The steady-state of the system can be found by numerically solving the set of equations. In figure 4.4 it is shown that the state of the resonator as given by the value of $\langle x^2 \rangle$ is the same for the mean field equations as the full numerical solution. Also shown in figure 4.4 is the predicted value from equation 4.1.4 ($\langle x^2 \rangle = x_{\mathrm{zp}}^2 (1 + 2\bar{n})$ for a thermal state), which also shows good agreement. The value of the current in the steady-state obtained from the mean field equations is indistinguishable from the results of the full numerical solution and fluctuating gate models, shown in figure 4.2, so is not shown here.

Although the set of non-linear equations fully describe the evolution of the system the calculation of the current noise can be simplified by forming a set of linear equations. With a linear set of equations we can use a method equivalent to that described in Section 2.6 to find the noise spectrum. We can also calculate the eigenvalues of the evolution, which we make use of below.

The non-linearity in the equations comes from the use of the cumulants to break correlations in the system. Without breaking these correlations the evolution of the SSET variables does not depend on equations for resonator operators alone. This suggests that the equations of motion for the resonator variables alone are not required to capture the resonator dynamics. The evolution of the resonator is included in the equa-

tions of the form $\langle \dot{x}c \rangle$. To recover a set of linear equations we replace the expectation values of resonator operators alone by their steady-state values. The steady-state values can be determined either from the non-linear set of equations, the numerical results or the thermal bath model described in Section 4.1.

The new set of linear equations retains the correlations between the SSET operators and position of the resonator and the dynamics of the resonator position. However, the set of second order non-linear equations also contained the dynamics of $\langle x^2 \rangle_t$. To include the same dynamics in the linearized equations we therefore have to extend the equations to third order, so that the dynamics of $\langle x^2 \rangle_t$ are included in terms such as $\left\langle \dot{x^2}c \right\rangle_t$. We then apply the approximation to products of four operators. Note that this extension to higher order is only to include the correct dynamics of the resonator it is not because the resonator state is not Gaussian (we still use only second order moments to describe the resonator state). The third order set of linearized equations includes both the dynamics and correlations that are present in the set of second order non-linear equations.

The linearized equations can be written in the form,

$$\dot{\boldsymbol{p}}(t) = A\boldsymbol{p}(t), \tag{4.3.16}$$

where $\boldsymbol{p}(t)$ is a vector of the moments of the system and A is a matrix that describes the evolution. The moments should be in a dimensionless form so that A then has dimensions of $time^{-1}$. The form of this equation is similar to equation 2.4.1 with A analogous to the Liouvillian, $\mathcal{L}$. Both equations describe the evolution of the same system but equation 4.3.16 describes the evolution of a number of mean quantities and is approximate. The steady-state of the linear equations is given by the null right hand eigenvector of A, $\boldsymbol{r_0}$, and should of course have the same result as the second order non-linear equations.

The calculation of the charge noise spectrum and current noise spectrum for the left hand junction can be carried out by use of the quantum regression theorem. For the right hand junction we use an electron counting variable approach [36, 61, 85] that we previously used in [24]. In Appendix C we describe in detail the approach for the charge noise spectrum and give the relevant operators for the current noise spectrum at

each of the junctions. The resulting spectra are,

$$S^m_{Q,Q}(\omega) = 4\Re\left[\sum_{p=1}^{30} \frac{\boldsymbol{l_0}^T Q^m \boldsymbol{r_p} \boldsymbol{l_p}^T Q^m \boldsymbol{r_0}}{-i\omega - \lambda_p^m}\right], \tag{4.3.17}$$

$$S^m_{I_L,I_L}(\omega) = 4\Re\left[\sum_{p=1}^{30} \frac{\boldsymbol{l_0}^T I_L^m \boldsymbol{r_p} \boldsymbol{l_p}^T I_L^m \boldsymbol{r_0}}{-i\omega - \lambda_p^m}\right], \tag{4.3.18}$$

$$S^m_{I_R,I_R}(\omega) = 2e\boldsymbol{l_0}^T I_R^m \boldsymbol{r_0} + 4\Re\left[\sum_{p=1}^{30} \frac{\boldsymbol{l_0}^T I_R^m \boldsymbol{r_p} \boldsymbol{l_p}^T I_R^m \boldsymbol{r_0}}{-i\omega - \lambda_p^m}\right], \tag{4.3.19}$$

where λ_p^m are the eigenvalues of A with associated right and left eigenvectors $\boldsymbol{r_p}$ and $\boldsymbol{l_p}$. Q^m, I_L^m and I_R^m are matrices that act as charge and current operators on the mean field equations. Equations 4.3.17–4.3.19 are analogous to equations 2.7.4, 2.7.7 and 2.7.10 for the full system.

In figure 4.3 the zero frequency current noise as predicted by the mean field model is shown. The first thing to note is that the set of third order mean field equations (*mean3* in the plot) reproduce the numerical values exactly. Also shown for comparison is the current noise as predicted by the set of linearized second order equations (*mean2*), which only include the first order dynamics of the resonator. It can be seen that in comparison to the fluctuating gate model they get the correct symmetry but quantitative agreement is lacking. However, we also note that reducing the coupling reduces the importance of the higher order dynamics which the second order mean field calculation neglects. Figure 4.5 provides a clear illustration of this as it shows that the second order calculation becomes accurate for low enough κ.

If the mean field model is an accurate description of the system then the eigenvalues of A will be a small subset of those of the full system. The eigenvalues from the expansion give the time-scales of the system and can be used to understand the mean field equations better.

The eigenvalues for a resonator in a thermal state can be calculated exactly [86]. The first few of which are given in table 4.1. The SSET eigenvalues can also be calculated but they do not have a simple analytic form. In the interacting system the eigenvalues are somewhat modified and further eigenvalues will be introduced. However, the eigenvalues can be separated into two groups based on the real part of the eigenvalues. SSET eigenvalues have a real part $\sim \Gamma$ and resonator eigenvalues have a real part $\sim \gamma_{\text{ext}}$. We always have $\Gamma \gg \gamma_{\text{ext}}$ for our system and so there is a clear separation.

The linearized third order mean field equations include the resonator dynamics up to second order and so, as shown in table 4.1, we should expect A to contain the resonator eigenvalues $-\frac{\gamma}{2} \pm i\Omega_R$, $-\gamma$ and $-\gamma \pm 2i\Omega_R$. The total damping, γ, and renormalized frequency in the eigenvalues are given by equations 4.1.5 and 4.1.3.

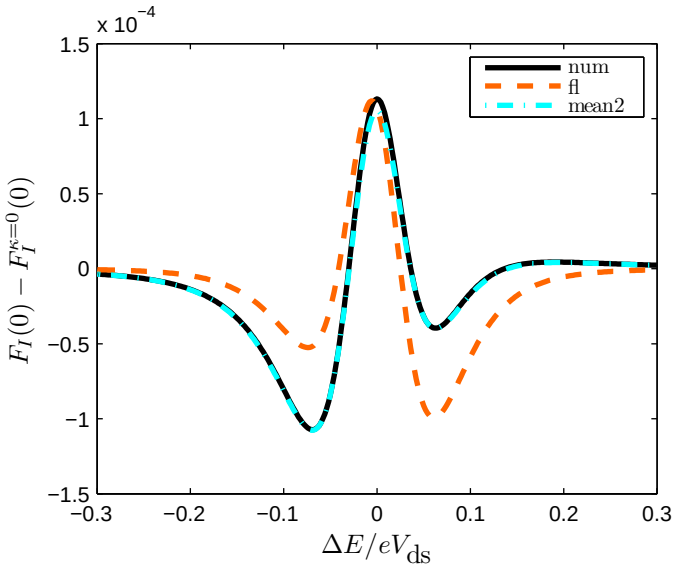

Figure 4.5. Change in the zero frequency Fano factor of the SSET due to the resonator for $\kappa = 5 \times 10^{-6}$. All other parameters and labelling of curves are the same as in figure 4.1.

Order	Eigenvalues		
0	0		
1	$-\frac{\gamma}{2} \pm i\Omega_R$		
2	$-\gamma$	$-\gamma \pm i2\Omega_R$	
3	$-\frac{3\gamma}{2} \pm i\Omega_R$	$-\frac{3\gamma}{2} \pm i3\Omega_R$	
4	-2γ	$-2\gamma \pm i2\Omega_R$	$-2\gamma \pm i4\Omega_R$

Table 4.1. Eigenvalues for a damped harmonic oscillator. First order describes the dynamics of $x(t)$ and $v(t)$, second order $x^2(t)$, $v^2(t)$ and $\{x, v\}(t)$, etc...

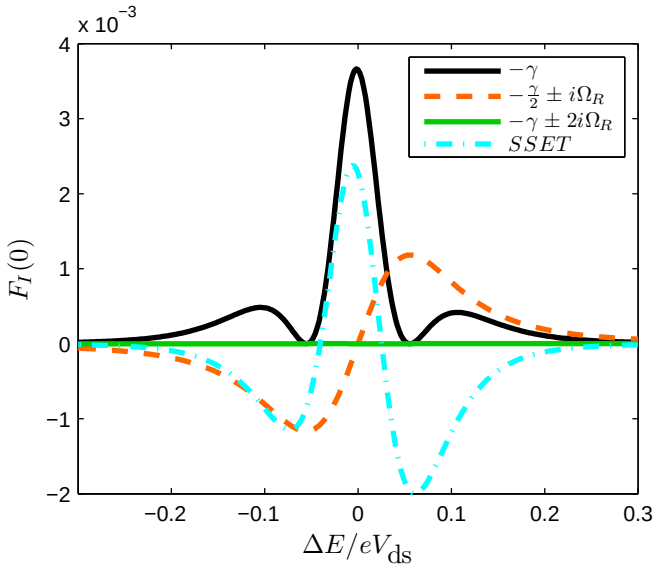

Figure 4.6. Contributions to the current noise from different eigenvalues using *mean3* model. $-\gamma$, $-\frac{\gamma}{2} \pm i\Omega_R$ and $-\gamma \pm 2i\Omega_R$ are the resonator eigenvalues and $SSET$ is the total contribution from the SSET eigenvalues. The parameters are the same as in figure 4.1.

In figure 4.6 we plot the contributions to the current noise due to each of these eigenvalues. The eigenvalues $-\frac{\gamma}{2} \pm i\Omega_R$ give an asymmetry in the zero frequency current noise. Complex eigenvalues correspond to features at finite frequency, which is better understood by looking at the finite frequency current noise spectrum, which we do in Section 4.5. The eigenvalue $-\gamma$ also has an important contribution to the current noise and is the energy relaxation rate of the resonator. The eigenvalues $-\gamma \pm 2i\Omega_R$ have a negligible contribution to the zero frequency noise since they correspond to a noise feature far from $\omega = 0$. The second order linearized mean field equations include only the $-\frac{\gamma}{2} \pm i\Omega_R$ eigenvalues which explains why they get the correct asymmetry but not quantitative agreement for the zero frequency current noise.

Also shown in figure 4.6 is the contribution from the rest of the terms in the expansion of the current noise. The other eigenvalues are of the SSET type and have a contribution equal to equation 4.2.6 (the fluctuating gate model). This shows that the fluctuating gate model accurately captures the modification to the SSET current noise that that occurs on the SSET time-scale, $1/\Gamma$.

4.4 Simple model of the resonator contribution to the current noise

The mean field equations as described in Section 4.3 provide a complete description of the system in the thermal regime. Using the fluctuating gate model described in Section 4.2 we can fully understand the part of the current noise that acts on the SSET time-scale. In this section we develop a simple model to describe the part of the current noise on the resonator time-scale. In terms of the mean field equations we would like to capture the part of the current noise due to the resonator eigenvalues $-\gamma$, $-\frac{\gamma}{2} \pm i\Omega_R$ and $-\gamma \pm 2i\Omega_R$.

In the thermal regime the resonator undergoes small fluctuations about some average position $x_{\rm fp} = \langle x \rangle$. We assume that the current is just a function of the position of the resonator, and time, and perform an expansion about $x_{\rm fp}$. We work to second order in position, which is sufficient due to the Gaussian nature of the resonator state.

$$I(x,t) = I(x_{\rm fp},t) + \bar{x}(t)\left.\frac{\partial I(x,t)}{\partial x(t)}\right|_{x(t)=x_{\rm fp}} + \frac{1}{2}\bar{x}(t)^2\left.\frac{\partial^2 I(x,t)}{\partial x(t)^2}\right|_{x(t)=x_{\rm fp}}, \quad (4.4.1)$$

where $\bar{x}(t) = x(t) - x_{\rm fp}$ as usual. We make the assumption that the gradient of the current is a constant in the steady-state and use the notation,

$$I' \equiv \lim_{t\to\infty}\left.\frac{\partial I(x,t)}{\partial x(t)}\right|_{x(t)=x_{\rm fp}},$$
$$I'' \equiv \lim_{t\to\infty}\left.\frac{\partial^2 I(x,t)}{\partial x(t)^2}\right|_{x(t)=x_{\rm fp}}. \quad (4.4.2)$$

I' gives the response of the current to a change in the position of the resonator (i.e. the linear response). I'' is the response of the current due to position fluctuations of the resonator. To obtain expressions for I' and I'' we differentiate equation 4.2.1 and retain terms up to second order in x_s,

$$I' = -\frac{32eE_J^2\Gamma m\Omega^2 x_s}{\beta^2}\left(\Delta E + 2m\Omega^2 x_s x_{\rm fp}\right) \quad (4.4.3)$$

$$I'' = -\frac{64eE_J^2\Gamma\left(m\Omega^2 x_s\right)^2}{\beta^2}\left(1 - \frac{16\Delta E^2}{\beta}\right) \quad (4.4.4)$$

where as before $\beta \equiv 4\Delta E^2 + \hbar^2\Gamma^2 + 3E_J^2$. I' has a zero at $\Delta E = -2m\Omega^2 x_s x_{\rm fp}$, which is near to the peak in the JQP current, since $x_{\rm fp}$ is small. I'' has two zeros when,

$$\Delta E = \pm\sqrt{\frac{1}{12}\left(\hbar^2\Gamma^2 + E_J^2\right)}. \quad (4.4.5)$$

Performing an average over equation 4.4.1, in the steady-state, we obtain the average

current, $\langle I \rangle_{ex}$,

$$\langle I \rangle_{ex} = \langle I(x_{\rm fp}) \rangle + \frac{1}{2} \langle \bar{x}^2 \rangle I''. \tag{4.4.6}$$

If $\langle I(x_{\rm fp}) \rangle$ is also expanded to second order in x_s then this equation is exactly equation 4.2.3 for the fluctuating gate model. However, we have retained the dynamics of the resonator in equation 4.4.1 and so can directly calculate the current noise from the relevant correlation function. The current noise is defined for operators about their steady-state value and so we subtract equation 4.4.6 from equation 4.4.1 to obtain,

$$\bar{I}(x,t) = \bar{I}(x_{\rm fp},t) + \bar{x}(t)I' + \frac{1}{2}\bar{x^2}(t)I'', \tag{4.4.7}$$

Note that the last term now contains $\bar{x^2}(t) = x^2(t) - \langle x^2 \rangle$ rather than $\bar{x}(t)^2 = (x(t) - \langle x \rangle)^2$. We now perform the expansion of the current correlation function used in the current noise,

$$\begin{aligned}
\langle \{\bar{I}(x,t+\tau), \bar{I}(x,t)\} \rangle &= \langle \{\bar{I}(x_{\rm fp},t+\tau), \bar{I}(x_{\rm fp},t)\} \rangle \\
&+ I'^2 \langle \{\bar{x}(t+\tau), \bar{x}(t)\} \rangle + \frac{1}{4} I''^2 \langle \{\bar{x^2}(t+\tau), \bar{x^2}(t)\} \rangle \\
&+ I' \Big[\langle \{\bar{I}(x_{\rm fp},t+\tau), \bar{x}(t)\} \rangle + \langle \{\bar{x}(t+\tau), \bar{I}(x_{\rm fp},t)\} \rangle \Big] \\
&+ \frac{1}{2} I'' \Big[\langle \{\bar{I}(x_{\rm fp},t+\tau), \bar{x^2}(t)\} \rangle + \langle \{\bar{x^2}(t+\tau), \bar{I}(x_{\rm fp},t)\} \rangle \Big] \\
&+ \frac{1}{2} I' I'' \Big[\langle \{\bar{x}(t+\tau), \bar{x^2}(t)\} \rangle + \langle \{\bar{x^2}(t+\tau), \bar{x}(t)\} \rangle \Big].
\end{aligned} \tag{4.4.8}$$

For a resonator in a thermal (Gaussian) state $x(t)$ and $x^2(t)$ are uncorrelated so the last line here is zero. To obtain a simple model we also neglect the third and fourth lines, which means neglecting the correlations between the SSET and resonator. By neglecting correlations we are also neglecting the back action contribution. For the model to be valid any fluctuations that are caused in the resonator due to the SSET must be dissipated in the external bath of the resonator rather than be reflected back to the SSET. This condition is satisfied for a large external temperature and large external damping of the resonator. Performing the required integration we obtain the current noise spectrum,

$$S^{ex}_{I,I}(\omega) = S_{I(x_{\rm fp}),I(x_{\rm fp})} + I'^2 S_{x,x}(\omega) + \frac{1}{4} I''^2 S_{x^2,x^2}(\omega). \tag{4.4.9}$$

The calculation of $S_{x,x}(\omega)$ and $S_{x^2,x^2}(\omega)$ for a thermal state is straightforward though

somewhat involved, it is described in Appendix D. We obtain the following spectra,

$$S_{x,x}(\omega) = \frac{4\gamma\Omega_R^2 \left\langle x^2 \right\rangle}{\left(\omega^2 - \Omega_R^2\right)^2 + \omega^2\gamma^2}, \tag{4.4.10}$$

$$S_{x^2,x^2}(\omega) = \frac{16\gamma\Omega_R^2 \left(\omega^2 + 4\gamma^2 + 4\Omega_R^2\right)\left[\left\langle x^2 \right\rangle^2 - \left\langle x \right\rangle^4\right]}{\left(\omega^2 + \gamma^2\right)\left(\left(4\Omega_R^2 - \omega^2\right)^2 + 4\omega^2\gamma^2\right)}. \tag{4.4.11}$$

$S_{x,x}(\omega)$ consists of a peaks at $\omega = \pm\Omega_R$ and $S_{x^2,x^2}(\omega)$ of peaks at $\omega = 0, \pm 2\Omega_R$. The positions of these peaks are the same as we expect for the resonator eigenvalues, $-\frac{\gamma}{2} \pm i\Omega_R$, $-\gamma$ and $-\gamma \pm 2i\Omega_R$. In Section 4.3 we noted that the $-\frac{\gamma}{2} \pm i\Omega_R$ eigenvalues describe the first order dynamics of the resonator whilst the $-\gamma$ and $-\gamma \pm 2i\Omega_R$ eigenvalues describe the second order dynamics (table 4.1). Similarly $S_{x,x}(\omega)$ is the spectrum of position fluctuations and $S_{x^2,x^2}(\omega)$ the spectrum of x^2 fluctuations.

It is helpful to study the behaviour of $S_{x^2,x^2}(\omega)$ near to $\omega = 0$ so that its contribution to the zero frequency current noise can be better understood. We can use the fact that $\left\langle x^2 \right\rangle^2 \gg \left\langle x \right\rangle^4$, since the displacement of the resonator must be small. For our system it is always the case, from our choice of parameters, that $\gamma \ll \Omega_R$. Near to $\omega = 0$ it will also be true that $\omega \ll \Omega_R$. The bracket on the top of $S_{x^2,x^2}(\omega)$ can therefore be reduced to $4\Omega_R^2$ and the right hand bracket on the bottom can be reduced to $16\Omega_R^4$ since all other terms added to these will be much smaller. With these approximations the peak around $\omega = 0$ is given by,

$$S_{x^2,x^2}^{\omega\simeq 0}(\omega) = \frac{4\gamma}{\omega^2 + \gamma^2}\left\langle x^2 \right\rangle^2, \tag{4.4.12}$$

which is a Lorentzian of width γ and height $4\left\langle x^2 \right\rangle^2/\gamma$. For the zero frequency current noise the contribution from the $-\gamma$ eigenvalue term should be compared with $I''^2\left\langle x^2 \right\rangle^2/\gamma$. In figure 4.7 it can be seen that good agreement is obtained. Notice that $I'' = 0$ at the steepest point on the JQP current curve, which from equation 4.4.5 is at $\Delta E = \pm 0.056\, eV_{\rm ds}$ for these parameters. At this point the current noise is insensitive to fluctuations in the noise of the resonator. This means that the current noise loses some of the strong dependence on the variance in the resonator position. The effect of the smearing out of the current noise peak as captured by the fluctuating gate model in Section 4.2 will still be present but we will lose the part due to the energy relaxation of the resonator described by the $-\gamma$ eigenvalue.

A striking example of this behaviour is shown in figures 3.13 and 3.14 for a low frequency resonator. Observe that there are two minima in $F_I(0)$ in the thermal regime. The minimum for $\Delta E < 0$ extends upwards in coupling through the transition to the limit cycle regime. In contrast F_n is increasing here as the coupling is increased and the transition to limit cycle occurs. Although we do not prove this here, it would appear

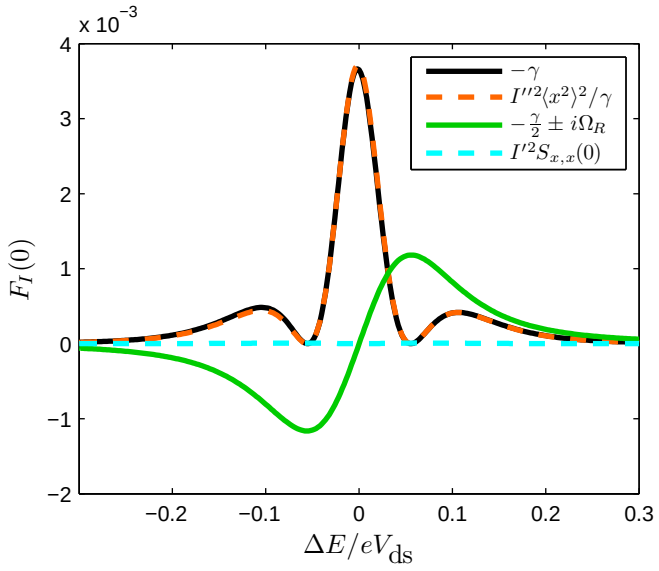

Figure 4.7. Eigenvalue contributions to the zero frequency current noise. $-\gamma$ and $-\frac{\gamma}{2} \pm i\Omega_R$ are from the *mean3* model and $I'' \left\langle x^2 \right\rangle^2 / \gamma$ and $I'^2 S_{x,x}(0)$ are the predictions for the same contributions using equation 4.4.9. The parameters are the same as in figure 4.1

that the result holds through the transition even though the state is no longer thermal. A similar feature can also be observed in the strongly interacting regime as shown in figures 3.17 and 3.18.

As shown by figure 4.6, the other important contribution to $F_I(0)$ to include is from the $-\frac{\gamma}{2} \pm i\Omega_R$ eigenvalues. In this model the term $I'^2 S_{x,x}(0)$ is the relevant approximation. However, as shown in figure 4.7 this term goes no way towards describing the feature in the zero frequency noise. This is unsurprising since $I'^2 S_{x,x}(0)$ is always positive so can clearly not describe a decrease in the noise. In the following section we will study the finite frequency noise spectrum to better understand the reasons for this.

4.5 Finite frequency current noise in the thermal state

Based on the mean field equations and the simple model in Section 4.4 we expect 5 peaks in the current noise spectrum as a result of the interaction with the resonator. These correspond to the eigenvalues $-\frac{\gamma}{2} \pm i\Omega_R$, $-\gamma$ and $-\gamma \pm 2i\Omega_R$. Since the spectrum is symmetric we will just investigate the $\omega > 0$ peaks, of which there should be 3. An example of the current noise spectrum calculated numerically (using the method described in Section 2.7) is shown in figure 4.8a. Just like the zero frequency current noise, the finite frequency current noise shows only weak modifications from the case of an uncoupled SSET. We have therefore subtracted the current noise spectrum for an

uncoupled SSET from the results. See [17, 47] for a discussion of the finite frequency current noise of a SSET at the JQP resonance.

In figures 4.8b–d we compare the full numerical solution with the current noise spectrum obtained from the third order mean field equations. It can be seen that good agreement is obtained for all 3 peaks. To further confirm that each of the peaks can be associated with a single term in the eigenfunction expansion we should look at the shape of the peak due to a single term,

$$S^p_{I,I}(\omega) = \frac{\gamma_p \Re[m^p_I(\omega)] + (\Omega_p - \omega)\Im[m^p_I(\omega)]}{\gamma_p^2 + (\Omega_p - \omega)^2} \tag{4.5.1}$$

where $\gamma_p = -\Re[\lambda_p]$, $\Omega_p = -\Im[\lambda_p]$ and,

$$\begin{aligned} m^p_I(\omega) = 2\langle\langle l_0|\mathcal{I}_L|r_p\rangle\rangle\langle\langle l_p|\mathcal{I}_L|r_0\rangle\rangle + 2\langle\langle l_0|\mathcal{I}_R|r_p\rangle\rangle\langle\langle l_p|\mathcal{I}_R|r_0\rangle\rangle \\ - \omega^2\langle\langle l_0|\mathcal{Q}|r_p\rangle\rangle\langle\langle l_p|\mathcal{Q}|r_0\rangle\rangle \end{aligned} \tag{4.5.2}$$

This expression is obtained by taking equation 2.7.2 and then adding a single term in the eigenfunction expansions of $S_{Q,Q}(\omega)$, $S_{I_L,I_L}(\omega)$ and $S_{I_R,I_R}(\omega)$ given in equations 2.7.4, 2.7.7 and 2.7.10. The feature described by $S^p_{I,I}(\omega)$ will have a width γ_p. For the resonator eigenvalues γ_p is small and so the dependence of $m^p_I(\omega)$ on ω can be neglected. The feature consists of a Lorentzian peak of height $\Re[m^p_I(\omega)]/\gamma_p$ and width γ_p and a resonance anti-resonance shape, which has a size given by the imaginary part of $m^p_I(\omega)$. If λ_p is real then m^p_I must also be real so that overall the current noise is symmetric. From equation 4.5.1 if the peak at $\omega = 0$ is described by the single eigenvalue, $-\gamma$ then it should have a Lorentzian shape of width γ, which we confirm in figure 4.9.

In addition to the three peaks there is a slowly varying background, which we associate with the modification to the SSET eigenvalue terms, that was captured in the zero frequency noise by the fluctuating gate model of Section 4.2. The background contribution is essentially constant over the width of the peaks in the spectrum (since $\Gamma \gg \gamma$) but varies with ΔE. In the following results we remove this shift as well and just show the contributions from the resonator eigenvalues.

We now investigate the change in the peaks with varying ΔE. Figure 4.10 shows the $\omega = 0$ peak, which we established in figure 4.9 to be a Lorentzian shape of width γ. This peak is entirely described by the simple model of Section 4.4, which predicted a Lorentzian peak of width γ and from an investigation of the zero frequency noise (see figure 4.7) we established that the model also correctly captures the height of the peak. The shape in figure 4.10 is therefore a Lorentzian of width γ and height $I''^2\left\langle x^2\right\rangle^2/\gamma$.

The peak at $\omega = \Omega_R$ is related to the position noise of the resonator. As shown by figure 4.8c it does not have the simple Lorentzian shape predicted by the simple model,

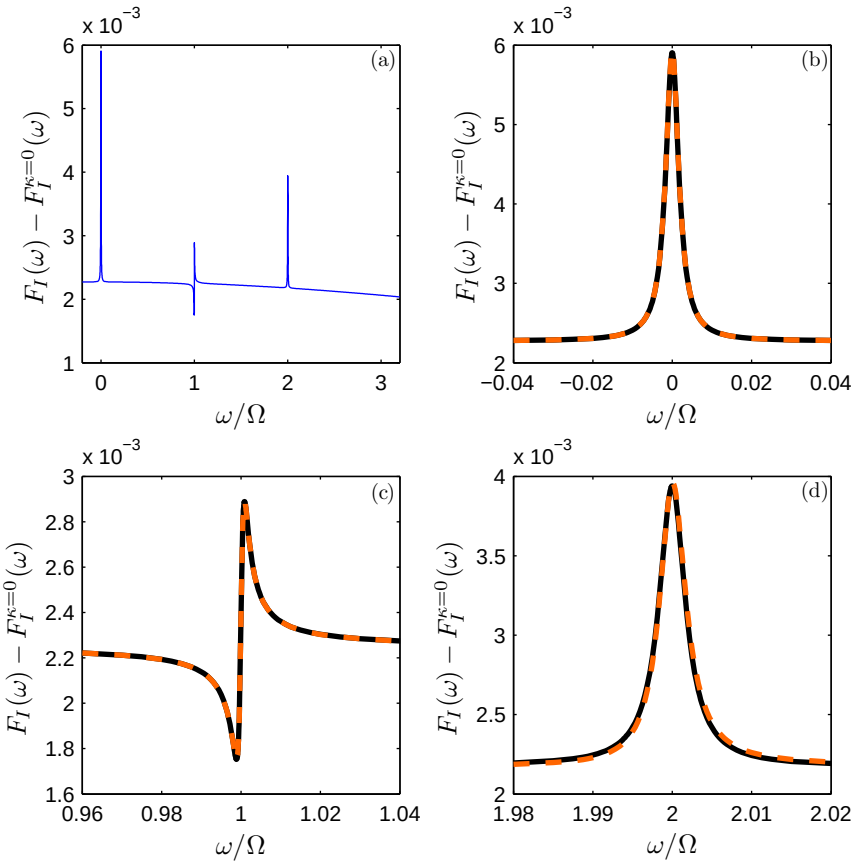

Figure 4.8. Finite frequency current noise spectrum for thermal state resonator for $\Delta E = 0$ with the other parameters the same as in figure 4.1. The finite frequency current noise spectrum for an uncoupled SSET has been subtracted from the results. (a) shows the full range calculated numerically and (b–d) show the numerical solution (–) and third order mean field equations solution (- -) around each of the peaks

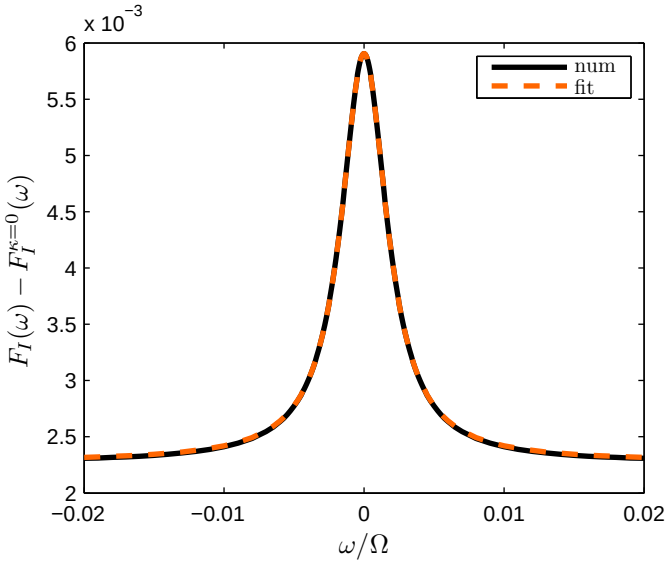

Figure 4.9. Peak at $\omega = 0$ comparing the full numerical solution (*num*) with a Lorentzian fit (*fit*). Here $\Delta E = 0$ and the other parameters are the same as in figure 4.1. The eigenvalue gives a width $-\gamma = 10.0 \times 10^{-5}\,\Gamma$ and the Lorentzian fit has a width $9.95 \times 10^{-5}\,\Gamma$.

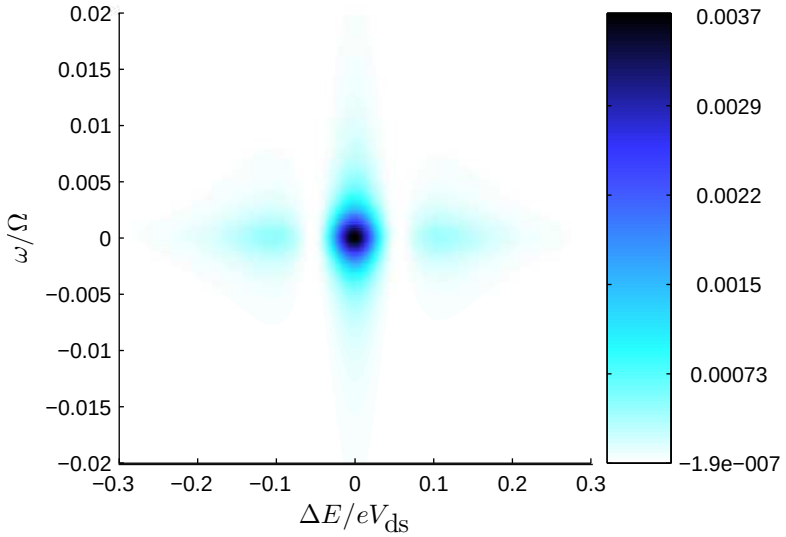

Figure 4.10. $F_I(\omega)$ peak at $\omega = 0$ for varying ΔE from the third order mean field equations. Only the contribution from the $-\gamma$ eigenvalue is shown. The parameters are the same as in figure 4.1

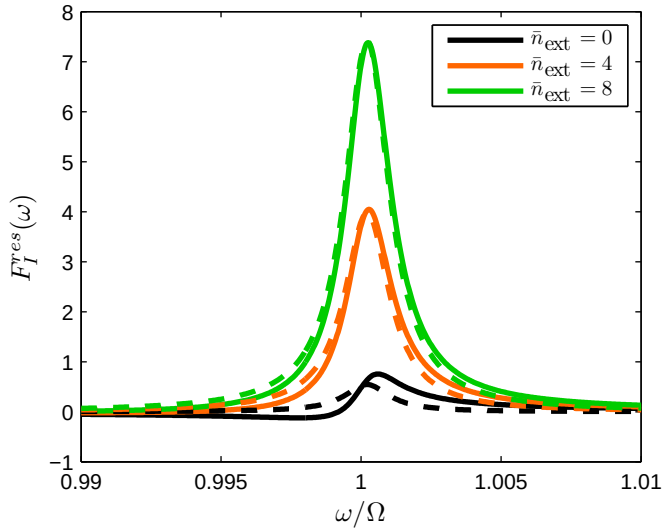

Figure 4.11. $\omega = \Omega_R$ peak for increasing $\bar{n}_{ext}$. $\Delta E = -0.055\, eV_{\rm ds}$ and the other parameters are the same as in figure 4.1. Solid lines are the $-\gamma/2 - i\Omega_R$ eigenvalue contribution to the current noise calculated from the third order mean field equations and the dashed lines are from the corresponding term from the simple model ($I'^2 S_{x,x}(\omega)$).

$I'^2 S_{x,x}(\omega)$. However, the shape is given by a single term in the eigenvalue expansion so the shape is described by equation 4.5.1. The peak consists of a resonance part and a resonance anti-resonance part. In [87] this feature was explained as a resonance peak at the renormalized resonator frequency and an anti-resonance at the bare frequency of the resonator. The anti-resonance part is due to the back-action of the resonator on the SSET in the system, which was neglected in the simple model. The effects of the back-action can be reduced by increasing the external temperature or external damping of the resonator. As shown in figure 4.11 by increasing the temperature we can accurately describe the peak using the term $I'^2 S_{x,x}(\omega)$.

In figure 4.12 we investigate the $\omega = \Omega_R$ peak for varying detuning. As shown from equation 4.1.3 the renormalized frequency is less than the bare resonator frequency when $\Delta E > 0$ and larger for $\Delta E < 0$. Although the change in frequency is small here the change in the asymmetry of the peak is evidence for the frequency shift. The peak vanishes at $\Delta E \simeq 0$, which is predicted by the simple model as due to the vanishing linear response (i.e. $I' = 0$). Note that in figure 4.8a we are very near this point so the $\omega = \Omega_R$ peak appears quite small. By comparing figures 4.10 and 4.12 it can be seen that in general the $\omega = \Omega_R$ peak is much larger than the one at $\omega = 0$.

In terms of the zero frequency current noise, we can now understand the effect of the $-\gamma/2 \pm i\Omega_R$ eigenvalue terms that was shown in figure 4.6. The variation in the

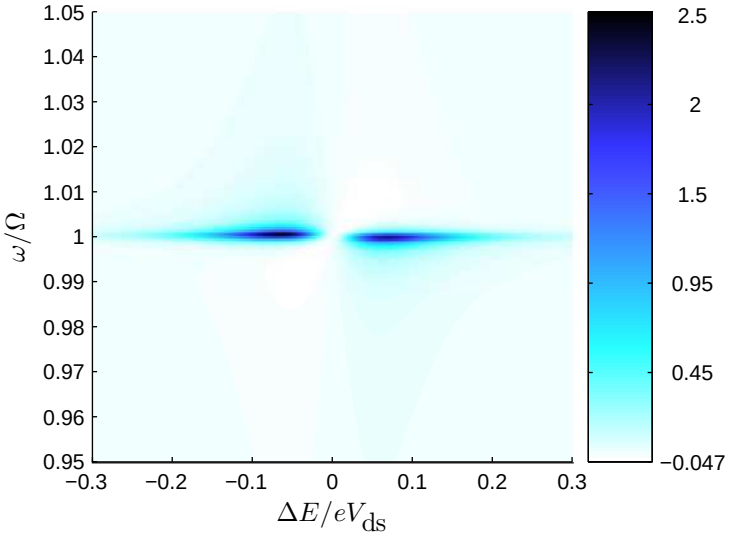

Figure 4.12. $F_I(\omega)$ peak at $\omega = \Omega_R$ for varying ΔE from the third order mean field equations. Only the contribution from the $-\frac{\gamma}{2} - i\Omega_R$ eigenvalue is shown. The parameters are the same as in figure 4.1

noise is mainly due to the strong back-action for these parameters. As the asymmetry of the peak changes this results in either an increase or decrease in the current noise at zero frequency.

The peak at $\omega = 2\Omega_R$ remains small in the thermal state, as shown in figure 4.13. It does show some asymmetry like the $\omega = \Omega_R$ peak but the effect is smaller. The asymmetry of the peak is not so apparent near to $\Delta E = 0$ since the frequency of the resonator is unchanged here. The height of the peak as a function of ΔE varies due to I''^2 just like the $\omega = 0$ peak. As shown in figure 4.14 the simple model describes the peak to a good approximation, which shows that the back-action effects are much weaker for this peak than the $\omega = \Omega_R$ peak.

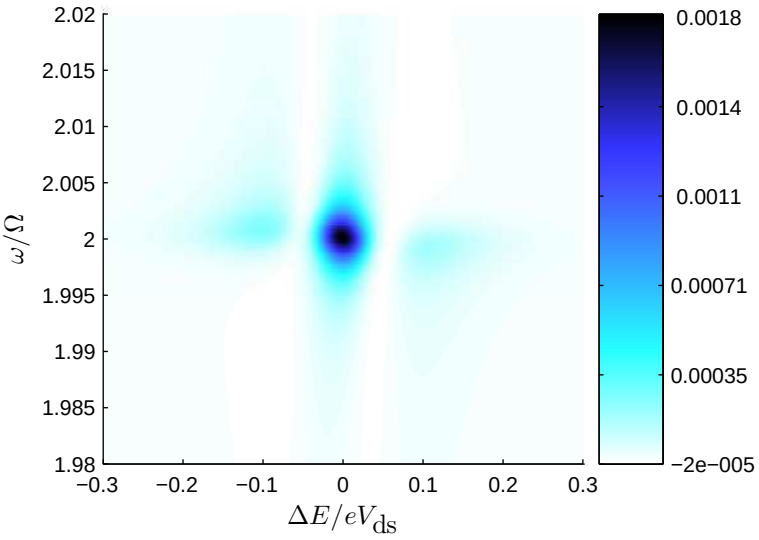

Figure 4.13. $F_I(\omega)$ peak at $\omega = 2\Omega_R$ for varying ΔE from the third order mean field equations. Only the contribution from the $-\gamma - 2i\Omega_R$ eigenvalue is shown. The parameters are the same as in figure 4.1

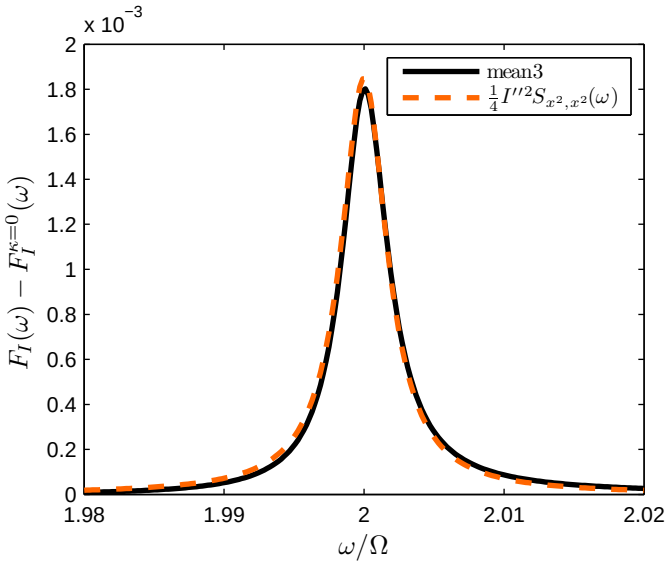

Figure 4.14. Peak at $\omega = 2\Omega_R$ comparing the $-\gamma - 2i\Omega_R$ term from the third order mean field equations (mean3) with the corresponding term from the simple model ($\frac{1}{4}I''^2 S_{x^2,x^2}(\omega)$) at $\Delta E = 0$ with the other parameters the same as in figure 4.1.

Chapter 5

Transitions in the Dynamical State of the Resonator

In Chapter 4 we investigated the regime of weak coupling, where the resonator remained in a thermal state, and found that the features seen in the current noise could be understood entirely. In this chapter we no longer restrict ourselves to weak coupling and investigate the regime where the SSET drives the resonator into states of self-sustained oscillations. We focus mainly on the zero frequency current noise, in particular, we discuss the transition regions in detail.

In Section 5.1 we give a brief review of transitions that occur and the types of states for the three frequency regimes of interest by looking at plots of the current and current noise. It will become apparent that the current noise in the bistable state is particularly simple. The noise properties of a generic bistable system are given in Section 5.2. The results of Section 5.2 are applied to our system in Section 5.3 to show that we have a true bistability for certain choices of the parameters. The quantum trajectories method (described in Appendix B) can be used to model an experiment on an individual quantum system. In Section 5.4 this method is applied to the SSET-resonator system. Finally in Section 5.5 we generalise some of the results from the bistable transition to better understand the current noise at the continuous transition and in the limit cycle state. In doing so we form a better understanding of the eigenfunction expansion of the Liouvillian.

5.1 A review of the behaviour of the system for moderate coupling

In this section we review the behaviour of the system in the three frequency regimes by calculating the current and current noise for some typical parameters as a function of

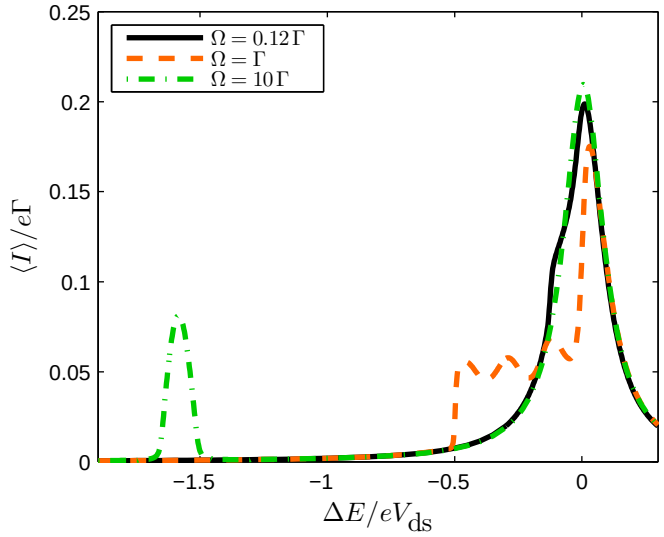

Figure 5.1. Current as a function of ΔE for different resonator frequencies $\Omega/\Gamma = 0.12, 1, 10$. In each case the values of κ and $\gamma_{\rm ext}$ have been chosen to ensure that the system reaches the limit cycle state for at least some values of ΔE whilst still remaining at low enough energies to allow a numerical calculation. For $\Omega = 0.12\,\Gamma$, $\kappa = 1.5 \times 10^{-3}$ and $\gamma_{\rm ext} = 1 \times 10^{-4}\,\Gamma$; for $\Omega = \Gamma$, $\kappa = 5 \times 10^{-3}$ and $\gamma_{\rm ext} = 8 \times 10^{-4}\,\Gamma$; and for $\Omega = 10\,\Gamma$, $\kappa = 3 \times 10^{-3}$ and $\gamma_{\rm ext} = 3 \times 10^{-4}\,\Gamma$. The other parameters are the same throughout: $E_J = 1/16\,eV_{\rm ds}$, $r = 1$ and $\bar{n}_{\rm ext} = 0$.

the detuning. We do this for moderate coupling, by which we mean that the parameters are such that the resonator is driven into the limit cycle state for $\Delta E < 0$ but the coupling is insufficient to form any of the more complex states such as the multiple limit cycles discussed in Section 3.7. The current is shown in figure 5.1 for resonator frequencies of $\Omega = 0.12\,\Gamma$, $\Omega = \Gamma$ and $\Omega = 10\,\Gamma$. The current for $\Omega = 10\,\Gamma$ and $\Omega = 0.12\,\Gamma$ are slices through the 2D plots in figures 3.8 and 3.12 respectively.

For $\Omega = 10\,\Gamma$ the current is almost unmodified around the JQP peak and on the scale of the plot can be taken as the uncoupled current, when considering the other frequency regimes. At $\Delta E \simeq -1.55\,eV_{\rm ds}$ the resonance corresponding to the absorption of one photon per Cooper pair tunnelling is observed. The resonator is in a limit cycle state near to the resonance, which is reached via a continuous transition on either side.

For $\Omega = 0.12\,\Gamma$ the current is suppressed near to resonance and enhanced for larger negative detuning. This behaviour is the same as seen for the weak coupling case in Chapter 4, but the change is much larger, particularly for $\Delta E < 0$. For negative detuning the resonator is in a limit cycle state in the region where the current is seen to be strongly modified (the location of the transition will become clearer shortly). The transition between the fixed point and limit cycle states occurs via a continuous

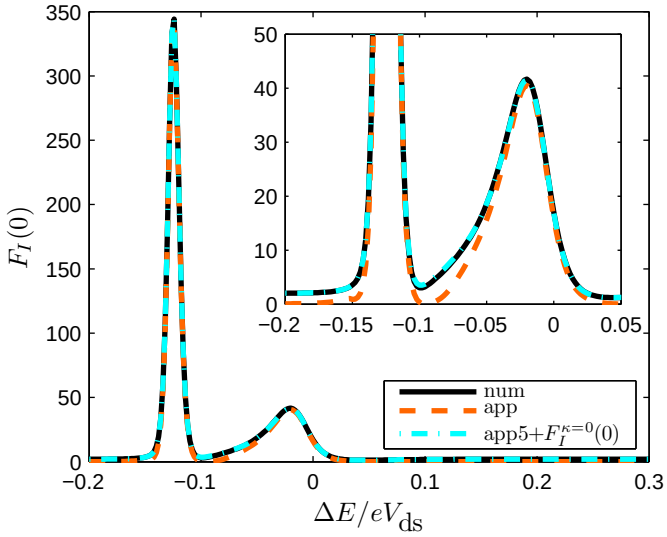

Figure 5.2. $F_I(0)$ for $\Omega = 0.12\,\Gamma$, with the other parameters given in figure 5.1. The curve labelled *num* shows the numerical value of the noise, *app* is the approximate value of the noise using the first term in equation 5.3.2, and *app5*+$F_I^{\kappa=0}(0)$ is the first five terms plus $F_I(0)$ for an uncoupled SSET (equation 5.5.2).

transition for $\Delta E \simeq 0$ and a bistable transition at $\Delta E \simeq 0.12\,eV_{\rm ds}$. The current is also modified on the positive detuning side but the change is much smaller and so not apparent in figure 5.1. The state of the resonator on the $\Delta E > 0$ side is thermal and so the models of Chapter 4 can be applied.

For $\Omega = \Gamma$ the JQP current is strongly altered for $\Delta E < 0$. There is a strong suppression of the JQP peak and peaks are seen corresponding to the 1, 2 and 3 photon resonances. The resonator is driven into a limit cycle state on the $\Delta E < 0$ side. Similar to the $\Omega = 0.12\,\Gamma$ case this transition occurs via a continuous transition at $\Delta E \simeq 0$. A bistable transition is then seen at $\Delta E \simeq -0.5\,eV_{\rm ds}$ corresponding to a sharp change in the current.

Figures 5.2–5.4 show the current noise calculated numerically for the same parameters. For $\Omega = 0.12\,\Gamma$ and $\Omega = \Gamma$ the two peaks in the current noise correspond in both cases to a continuous transition from a fixed point state to a limit cycle at $\Delta E \simeq 0$ and the presence of a region of bistability near the second (larger) peak in $F_I(0)$. In between these two peaks the system is in a limit cycle state. For the $\Omega = 10\,\Gamma$ case the two peaks in $F_I(0)$ both correspond to continuous transitions (from fixed point to limit cycle state) with the resonator in a limit cycle state between the peaks. Also shown on the plots are various approximations to the current noise that are introduced later in this chapter.

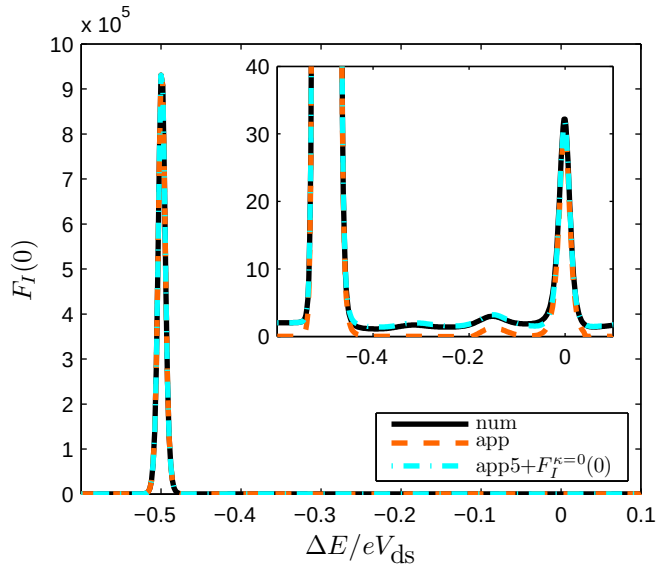

Figure 5.3. $F_I(0)$ for $\Omega = \Gamma$, with the other parameters given in figure 5.1. The curve labelled *num* shows the numerical value of the noise, *app* is the approximate value of the noise using the first term in equation 5.3.2, and *app5*+$F_I^{\kappa=0}(0)$ is the first five terms plus $F_I(0)$ for an uncoupled SSET (equation 5.5.2).

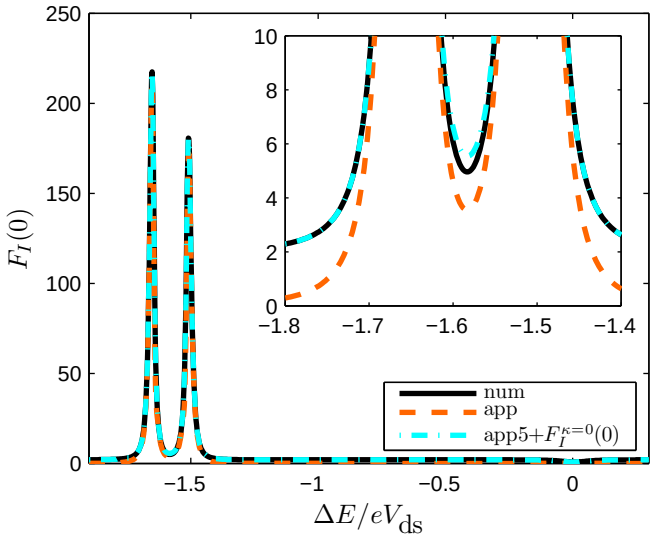

Figure 5.4. $F_I(0)$ for $\Omega = 10\,\Gamma$, with the other parameters given in figure 5.1. The curve labelled *num* shows the numerical value of the noise, *app* is the approximate value of the noise using the first term in equation 5.3.2, and *app5*+$F_I^{\kappa=0}$ is the first five terms plus $F_I(0)$ for an uncoupled SSET (equation 5.5.2).

5.2 A model of a generic bistable system

The current noise for bistable regions in nanoelectromechanical systems, such as the charge shuttle, have been studied extensively [88–91]. Before discussing the bistable region for the SSET-resonator system we describe, in this section, the features of a generic system that has two current states. This generic bistable system is truly bistable in the sense that there are only two accessible internal states as opposed to the SSET-resonator system, where this can only ever be approximately true. The current characteristics of a bistable system can be described by a model specified in terms of four parameters, which are the currents associated with the two states I_1 and I_2, and the switching rates between them of Γ_{12} and Γ_{21}. The current and current noise for this two-state model take the simple form [90, 92],

$$\langle I \rangle_{bi} = \frac{\Gamma_{21} I_1 + \Gamma_{12} I_2}{\Gamma_{21} + \Gamma_{12}}, \tag{5.2.1}$$

$$S^{bi}_{I,I}(\omega) = \frac{4 \left\langle \bar{I}^2 \right\rangle (\Gamma_{21} + \Gamma_{12})}{\omega^2 + (\Gamma_{21} + \Gamma_{12})^2}, \tag{5.2.2}$$

where $\left\langle \bar{I}^2 \right\rangle = \Gamma_{21}\Gamma_{12}(I_1 - I_2)^2/(\Gamma_{21} + \Gamma_{12})^2$, is the *variance* in the steady-state current. It is helpful here to make a distinction between the variance of the current and the current noise. The variance of the current is the second cumulant of the steady-state current. The zero frequency current noise on the other hand is the zero frequency limit of the spectrum of current fluctuations. The latter includes information about dynamics of the system since it considers correlations in the current at two times.

The simple two-state model can be applied to a more complex system if it can be described by two metastable states that are well enough separated such that the switching rate between the states is much slower than the other relevant time-scales [90, 91]. From equation 5.2.2 we can see how slow switching rates between the two states can lead to a large value for the current noise in this regime. However, we also note that when the two metastable states give rise to very different currents the large variance that results can also make an important contribution to the current noise.

To test the applicability of the simple two state model we can use the current and zero frequency current noise together with estimates of the current in the two states to calculate the switching rates from equations 5.2.1 and 5.2.2. In order to confirm that the model then works we need a third expression. The current noise involves a two time correlation function of the current. We can extend this to higher orders and define a three time current correlation function. Calculating a double Fourier transform over this correlation function will result in the third order current noise,

$$S^3_I(\omega_1, \omega_2) = \lim_{t\to\infty} \int_{-\infty}^{\infty} d\tau_1 \int_{-\infty}^{\infty} d\tau_2 \left\langle \{\bar{I}(t+\tau_2), \bar{I}(t+\tau_1), \bar{I}(t)\} \right\rangle e^{i\omega_1\tau_1} e^{i\omega_2\tau_2}, \tag{5.2.3}$$

where $\{\cdot,\cdot,\cdot\}$ is the symmetrized combination of the three operators. The result will in general depend on two frequencies and although calculable the interpretation is difficult [93]. Here we require only the zero frequency limit of the the third order current noise, which we will denote $\langle\langle I^3 \rangle\rangle$ following the notation of [90].

$$\langle\langle I^3 \rangle\rangle = \lim_{\substack{\omega_1 \to 0 \\ \omega_2 \to 0}} S_I^3(\omega_1, \omega_2) \tag{5.2.4}$$

Just like $S_{I,I}(0)$, $\langle\langle I^3 \rangle\rangle$ is independent of the junction, at which it is measured. For a bistable system $\langle\langle I^3 \rangle\rangle_{bi}$ is given by [90, 92],

$$\langle\langle I^3 \rangle\rangle_{bi} = \frac{6\left\langle \bar{I}^2 \right\rangle (I_1 - I_2)(\Gamma_{12} - \Gamma_{21})}{(\Gamma_{21} + \Gamma_{12})^3}. \tag{5.2.5}$$

Agreement between the bistable model and a calculation of $\langle\langle I^3 \rangle\rangle$ provides good evidence that the system is bistable [90].

Another prediction of equation 5.2.2 is that the finite frequency current noise peak, at $\omega = 0$ is a Lorentzian of width $\Gamma_{21} + \Gamma_{12}$. The presence of such a feature provides further evidence of a bistability [91, 94].

5.3 Proving the presence of a bistability

In this section we use the methods developed in the previous section in order to prove the presence of a bistability in the SSET-resonator system. We then go on to show how this relates to the eigenvalue expansion of the current noise. The required parameters for the two state model can be extracted numerically as follows. The relative probabilities of the two states $\Gamma_{21}/(\Gamma_{21}+\Gamma_{12})$ and $\Gamma_{12}/(\Gamma_{21}+\Gamma_{12})$ are obtained by inspection of the steady state probability distribution $P(n)$. Setting those elements of the steady state density matrix, which correspond to just one of the two states, to zero and recalculating the current then allows the currents I_1 and I_2 to be obtained. Finally, the sum of the rates $\Gamma_{12}+\Gamma_{21}$, and hence the individual rates, can be determined by comparing the current noise (calculated numerically) with equation 5.2.2.

To calculate $\langle\langle I^3 \rangle\rangle$ we use the result given in [90], which is valid for the right hand junction,

$$\begin{aligned}\langle\langle I_R^3 \rangle\rangle = \langle\langle l_0 | \mathcal{I}_R | r_0 \rangle\rangle - 6\langle\langle l_0 | \mathcal{I}_R \mathcal{R}(0) \mathcal{I}_R | r_0 \rangle\rangle + 6\langle\langle l_0 | \mathcal{I}_R \mathcal{R}(0) \mathcal{I}_R \mathcal{R}(0) \mathcal{I}_R | r_0 \rangle\rangle \\ - 6\langle\langle l_0 | \mathcal{I}_R \mathcal{R}(0) \mathcal{R}(0) \mathcal{I}_R | r_0 \rangle\rangle \langle\langle l_0 | \mathcal{I}_R | r_0 \rangle\rangle\end{aligned} \tag{5.3.1}$$

where $\mathcal{R}(\omega)$ and $\mathcal{I}_R$ were defined in equations 2.6.12 and 2.7.8 respectively. We can only apply the two state model when two meta-stable states can unambiguously be defined (i.e. the $P(n)$ distribution for the resonator steady state should have two peaks

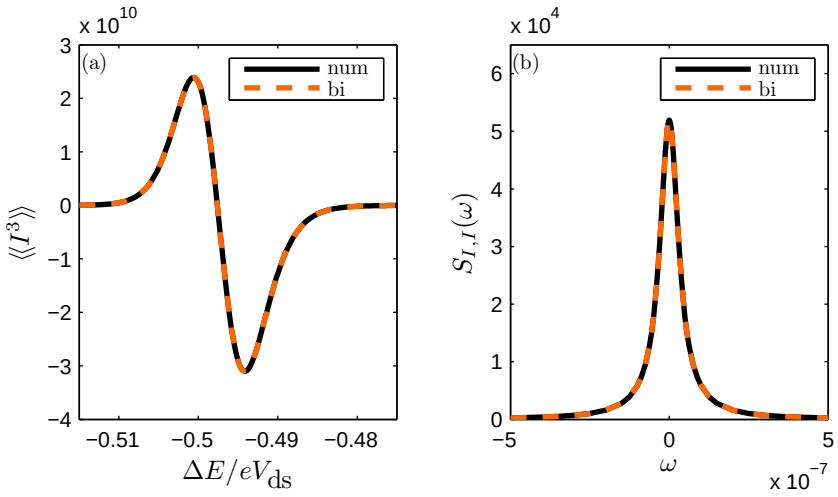

Figure 5.5. Comparison of numerical results (*num*) with the predictions for a bistable system (*bi*) for $\Omega = \Gamma$, with the other parameters given in figure 5.1. (a) Value of $\langle\langle I^3 \rangle\rangle$ as a function of ΔE. (b) Finite frequency current noise peak around $\omega = 0$ for $\Delta E = -0.497$.

with a vanishingly small probability for some range of n values in between). If this is not the case then it is not possible to separate the density matrix into parts corresponding to each of the states. Generally we can apply the method when $\Omega \gtrsim \Gamma$. The method can be applied to the bistable state seen at $\Delta E \simeq -0.5\, eV_{\rm ds}$ in figure 5.3 ($\Omega = \Gamma$) but not to the bistable state at $\Delta E \simeq -0.12\, eV_{\rm ds}$ in figure 5.2 ($\Omega = 0.12\,\Gamma$), where there is significant overlap between the limit cycle and fixed point states.

In figure 5.5a we compare the value of $\langle\langle I^3 \rangle\rangle$ obtained numerically with the two state model by following the above procedure. It can be seen that the values obtained for the third cumulant from the full numerical solution and the bistable model are in agreement. Shown in figure 5.5b is the finite frequency current noise peak calculated numerically at $\omega = 0$ (see Section 2.7) compared with a Lorentzian given by equation 5.2.2, for a value of ΔE near the middle of figure 5.5a, which is also in agreement. These results show that the simple two state model is valid for this set of parameters.

To better understand the bistable model it is helpful to use the eigenfunction expansion of the current noise (see Section 2.7). For the zero frequency current noise at the left hand junction this is (see equation 2.7.7),

$$S_{I_L I_L}(0) = -4 \sum_{p=1}^{\infty} \frac{1}{\lambda_p} \langle\langle l_0 | \mathcal{I}_L | r_p \rangle\rangle \langle\langle l_p | \mathcal{I}_L | r_0 \rangle\rangle \,. \tag{5.3.2}$$

For comparison a similar expansion of the variance in the steady-state current, also for

the left hand junction, is,

$$\left\langle \bar{I_L}^2 \right\rangle = \left\langle I_L^2 \right\rangle - \left\langle I_L \right\rangle^2$$
$$= \sum_{p=1}^{\infty} \langle\langle l_0 | \mathcal{I}_L | r_p \rangle\rangle \langle\langle l_p | \mathcal{I}_L | r_0 \rangle\rangle \,. \tag{5.3.3}$$

The variance is given by a sum over the same matrix elements as the current noise, but this time unmodified by the eigenvalues, λ_p. Each of the eigenvectors of the Liouvillian $|r_p\rangle\rangle$ describe a change to (or fluctuation away from) the steady state that decays with a purely exponential rate $-\mathrm{Re}(\lambda_p)$ (see equation 2.5.3). Thus, the matrix element $\langle\langle l_0 | \mathcal{I}_L | r_p \rangle\rangle \langle\langle l_p | \mathcal{I}_L | r_0 \rangle\rangle$ can be thought of as the *variance in the current due to a fluctuation of type* p. We then see that the current noise consists of a sum over the variances due to each type of fluctuation, each divided by the rate at which that fluctuation decays.

It is clear from equation 5.3.2 that if $|\lambda_1| \ll |\lambda_2|$, then we expect the current noise to be dominated by the first term, which corresponds to the slowest time-scale in the system. This is in indeed what happens when the system has a well-defined bistability. In this case an obvious connection can be made with the two state model described in Section 5.2 (i.e. equation 5.2.2). The smallest eigenvalue corresponds to the sum of the rates $-\lambda_1 = \Gamma_{12} + \Gamma_{21}$ and the numerator gives the current variance, $\langle\langle l_0 | \mathcal{I}_L | r_1 \rangle\rangle \langle\langle l_1 | \mathcal{I}_L | r_0 \rangle\rangle = \left\langle \bar{I}^2 \right\rangle$.

The relationship between the two state model and eigenfunction expansion also extends to the finite frequency current noise. The first term of the expansion of the finite frequency current noise at the left hand junction is (see equation 2.7.7 and discussion below equation 4.5.1),

$$S^1_{I_L,I_L}(\omega) = -\frac{4\lambda_1}{\lambda_1^2 + \omega^2} \langle\langle l_0 | \mathcal{I}_L | r_1 \rangle\rangle \langle\langle l_1 | \mathcal{I}_L | r_0 \rangle\rangle \tag{5.3.4}$$

Using $-\lambda_1 = \Gamma_{12} + \Gamma_{21}$ and $\langle\langle l_0 | \mathcal{I}_L | r_1 \rangle\rangle \langle\langle l_1 | \mathcal{I}_L | r_0 \rangle\rangle = \left\langle \bar{I}^2 \right\rangle$ this is identical to equation 5.2.2.

Although we have used the current noise at the left hand junction here an identical result can be obtained for the right hand junction. This is because $S_{I_L,I_L}(0) = S_{I_R,I_R}(0)$ so if a single term of the expansion describes $S_{I_L,I_L}(0)$ then we must have $\langle\langle l_0 | \mathcal{I}_L | r_1 \rangle\rangle \langle\langle l_1 | \mathcal{I}_L | r_0 \rangle\rangle = \langle\langle l_0 | \mathcal{I}_R | r_1 \rangle\rangle \langle\langle l_1 | \mathcal{I}_R | r_0 \rangle\rangle$. The $2e\langle I \rangle$ part of $S_{I_R,I_R}(\omega)$ can be neglected when the current noise is large.

5.4 Quantum trajectories

In an experiment, on the SSET-resonator system in the bistable regime, one would hope to be able to monitor the current with sufficient time resolution to observe the slow

switching between two distinct values of the current directly. By using the method of quantum trajectories we can model what might occur in an ideal experiment [32, 95, 96].

A full description of the method is given in Appendix B. The basics of the method are that we have an ideal detector that can detect when a quasi-particle tunnels across the right hand junction. By use of the quantum trajectories method we can obtain a density matrix conditioned on a particular measurement record (i.e. the times at which detections are made). The measurement record could be obtained from an experiment but, as described in the appendix we can make use of random numbers to perform a simulation. We will first use the example of a SSET alone to illustrate how information is gained about the system based on the detection of quasi-particles.

In figure 5.6a we show the values of $\langle p_1 \rangle_t$ and $\langle p_2 \rangle_t$ for the beginning of a typical trajectory. We assume that the experiment is set up at $t = -\infty$ and then the detector is switched on at $t = 0$ so that the initial density matrix is the steady-state density matrix of the system. The probabilities for the two states are initially the same, since this is the case for a steady-state. Then over time the probability to be in the $|1\rangle$ state rapidly decays. The reason for this is that there is no way of accessing the $|1\rangle$ state except for a quasi-particle tunnelling and so unless a quasi-particle is detected the probability of this state must decay away. The probability for the $|2\rangle$ state shows strongly damped oscillations before coming to a steady value. These oscillations are due to the Josephson coupling between the $|0\rangle$ and $|2\rangle$ states and are damped by the quasi-particle tunnelling.

At $t = 19.2\,\Gamma$ a quasi-particle is detected. The detection of a quasi-particle tunnelling event corresponds to a rapid change in our knowledge of the state of the system. Before the quasi-particle tunnelled across the junction the SSET must have been either in the $|1\rangle$ or the $|2\rangle$ state (see figure 2.5). After the quasi-particle tunnelling the SSET must now be either in the $|0\rangle$ or the $|1\rangle$ state. The expectation values of the charge states are changed according to,

$$\langle p_0 \rangle_{t+dt} = \frac{\langle p_1 \rangle_t}{\langle p_1 \rangle_t + \langle p_2 \rangle_t}, \quad \langle p_1 \rangle_{t+dt} = \frac{\langle p_2 \rangle_t}{\langle p_1 \rangle_t + \langle p_2 \rangle_t}, \quad \langle p_2 \rangle_{t+dt} = 0, \tag{5.4.1}$$

where the terms on the bottom ensure the density matrix remains normalized. Since before the jump $\langle p_1 \rangle_t$ was small the SSET is most likely in the $|1\rangle$ state following the first jump. A second quasi-particle is detected a short time later ($t = 20.4\,\Gamma$). Following the second jump the SSET is most likely to be in the state $|0\rangle$ state since before the jump $\langle p_1 \rangle_t$ was large. In between the pairs of quasi-particles we again see strongly damped oscillations of $\langle p_2 \rangle_t$ due to the Josephson effect, which are strongly damped due to the large dissipation.

It can be seen in figure 5.6a that after detecting a small number of quasi-particles we can be sure of when the SSET is in the $|1\rangle$ state and when it is in a superposition of the $|0\rangle$ and $|2\rangle$ states. In a more realistic experiment we should also include things

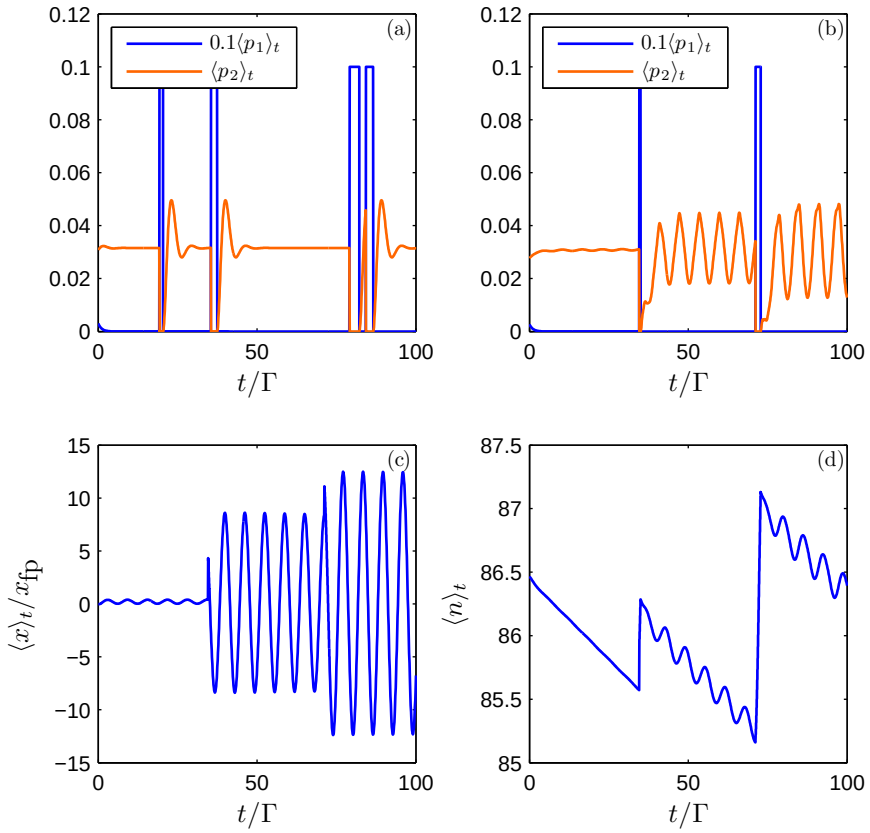

Figure 5.6. Quantum trajectories: (a) $\langle p_1\rangle_t$ and $\langle p_2\rangle_t$ for SSET alone, (b) $\langle p_1\rangle_t$ and $\langle p_2\rangle_t$ with resonator, (c) and (d) $\langle x\rangle_t$ and $\langle n\rangle_t$ for the same trajectory as (b). Parameters for (a) are $\Delta E = -0.15\,eV_{\rm ds}$, $E_J = 1/16\,eV_{\rm ds}$ and $r = 1$. Parameters for (b–c) are $\Delta E = -0.45\,eV_{\rm ds}$, $\kappa = 0.005$, $\Omega = \Gamma$, $E_J = 1/16\,eV_{\rm ds}$, $\gamma_{\rm ext} = 8\times10^{-4}\,\Gamma$, $r = 1$ and $\bar{n}_{\rm ext} = 0$.

such as the efficiency of the detector [97], which would lead to some uncertainty in the state of the SSET.

The method can be extended to include the resonator as well. We could assume that each photon or phonon that is absorbed and emitted by the resonator can be detected. For a superconducting stripline resonator the main loss mechanism is through the capacitors at the ends of the resonator so this detection might be feasible experimentally. For a mechanical resonator, however, the losses cannot be detected and so this would be an unrealistic model. We therefore assume that we have the same detector but the evolution now includes the resonator also. Calculating the expectation values of resonator operators will tell us the information we have gained about the state of the resonator from the detection of quasi-particles.

In figure 5.6b we again show $\langle p_1 \rangle_t$ and $\langle p_2 \rangle_t$ for the beginning of the evolution but now with coupling to the resonator. For the parameters chosen the resonator is in a limit cycle state. $\langle p_1 \rangle_t$ behaves as before by initially going rapidly to zero and between the two quasi-particle tunnellings during each cycle to a value of one. However, $\langle p_2 \rangle_t$ now shows continual oscillations rather than the strongly damped oscillations observed in the uncoupled case. These oscillations become more apparent following the detection of the quasi-particles. We can understand this from the nature of the coupling in the device. The charge of the island is coupled to the position of the oscillator. The resonator therefore oscillates about a different fixed point depending on the charge of the island. Any knowledge we gain about the island charge must therefore give us some information about the position of the resonator. As seen in figure 5.6c $\langle x \rangle_t$ is initially zero since we have no knowledge about the phase of the oscillator. From the initial changes in the island charge we gain some knowledge about the phase of the resonator so we see oscillations in $\langle x \rangle_t$. The position of the resonator modifies the detuning of the SSET so the oscillations are also present in $\langle p_2 \rangle_t$. Following the detection of a quasi-particle we see much larger oscillations in the $\langle x \rangle_t$ since we gain additional knowledge about the phase of the oscillations due to our increased knowledge of the charge. Finally we can investigate the average energy of the resonator shown in figure 5.6d. For these parameters $\bar{n}_{\text{ext}} = 0$ so the resonator can only gain energy from the SSET. We therefore observe an initial decay of $\langle n \rangle_t$. The current through the SSET here would be almost zero in the absence of coupling to the resonator so following the detection of the first quasi-particle in the cycle it is very likely that some energy is transferred from the SSET to the resonator. We therefore see a jump in the energy following the detection of the first quasi-particle but not the second since this does not give us any further information.

We now investigate the case of a bistable region. The currents for the limit cycle and fixed point states are very different, which leads to a large variance in the overall current as seen in the previous sections. In terms of the trajectories, the limit cycle state has higher energy than the fixed point state, which must be sustained by the detection of a large number of quasi-particles. Conversely for a fixed point state there must be a sufficient gap between tunnelling events in order for the resonator to relax. The limit cycle state is therefore the state with the higher current. The two states here are less well separated here than the bistability we studied in Section 5.3. The reason being that numerical time evolution is slow and needs to be carried out for a long enough time that a large number of switches between the fixed point and limit cycle occur. In figure 5.7a we show the evolution of $\langle n \rangle_t$ for these parameters and the associated $P(n)$ distribution in figure 5.7b. The value of $\langle n \rangle_t$ spends time mainly around $n = 0$ and $n = 25$, which correspond to the peaks in the $P(n)$ distribution, this confirms that the quasi-particle detection tells us when the resonator is in the fixed point or limit cycle states.

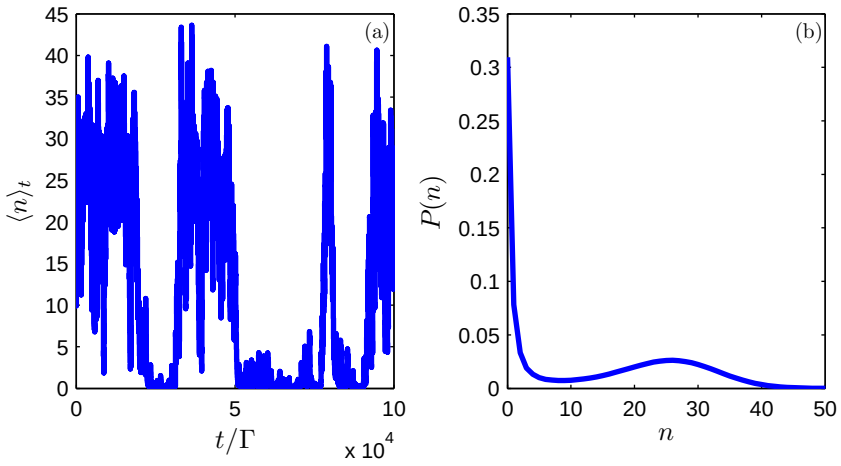

Figure 5.7. (a) Quantum trajectory of $\langle n \rangle_t$ for bistable region. (b) Associated $P(n)$ distribution. Parameters are $\Delta E = -0.473\, eV_{\rm ds}$, $\kappa = 0.016$, $\Omega = \Gamma$, $E_J = 1/16\, eV_{\rm ds}$, $\gamma_{\rm ext} = 0.003\,\Gamma$, $r = 1$ and $\bar{n}_{\rm ext} = 0$.

The trajectory of $\langle n \rangle_t$ can be used to calculate the waiting times in the limit cycle and fixed point states and hence calculate the switching rates between the two. As seen in figure 5.7a it is not always clear which state the system is in. By choosing a better separated bistable state the situation is improved, however, the tunnelling rate between the two states can then become very slow and so the length of time taken to simulate the trajectory is too long. First the centre of each state is determined, either from the $P(n)$ distribution or estimated from the trajectory. The system is then said to have entered the state when $\langle n \rangle_t$ passes this mid-point.

The tunnelling rate out of a state is given by the inverse of the average time the system spends in the state. Adding up the number of quasi-particles detected while in each state gives an estimate of the current in each of the states. This provides another method of determining the rates and currents in equations 5.2.1 and 5.2.2. Using the parameters in figure 5.7 we obtain the following results from the trajectories.

$$\begin{aligned} I_1 &= 0.0127 & I_2 &= 0.049 \\ \Gamma_{12} &= 6.99 \times 10^{-5} & \Gamma_{21} &= 5.13 \times 10^{-5} \end{aligned} \tag{5.4.2}$$

Then by use of equations 5.2.1 and 5.2.2 we can calculate,

$$\begin{aligned} \langle I \rangle_{bi} &= 0.034 & S^{bi}_{I,I}(0) &= 10.66 \\ \Gamma_{12} + \Gamma_{21} &= 1.21 \times 10^{-4} \end{aligned} \tag{5.4.3}$$

The numerically obtained values are,

$$\begin{aligned} \langle I \rangle &= 0.033 & S_{I,I}(0) &= 14.5 \\ -\lambda_1 &= 1.20 \times 10^{-4} \end{aligned} \tag{5.4.4}$$

The bistability here is not sufficiently good to get the correct current noise but we obtain good agreement for the current and between the eigenvalue and sum of the switching rates.

5.5 Transitions and time-scales

In general, we cannot describe our system in the vicinity of the dynamical transitions by a simple two-state model. As we have seen, even where the transition involves a region of coexistence between the limit cycle and fixed point states the states may not be well enough separated for a two-state model to apply. Near the continuous transitions between the limit cycle and fixed point states there are clearly not just two states involved. However, one element of the two state model which might be expected to apply more widely is the emergence of a single very slow time-scale, which dominates the current noise. In the case of the continuous transition such a slow time-scale might result from the vanishing effective damping ($\gamma_{\mathrm{sset}} + \gamma_{\mathrm{ext}}$) of the system at the transition. In what follows we use the eigenfunction expansion of the Liouvillian to investigate the extent to which the current noise can be described by a single term of this expansion.

More generally, it is not just a slow time-scale that is important. For a single term in the eigenfunction expansion (equation 5.3.2) to accurately describe the noise, the *matrix element divided by the eigenvalue* $\langle\langle l_0 | \mathcal{I}_L | r_p \rangle\rangle \langle\langle l_p | \mathcal{I}_L | r_0 \rangle\rangle / \lambda_p$ for $p = 1$ must be much larger than for all $p \geq 2$. In figures 5.2–5.4 we compare the full current Fano factor with approximations using just the first term in equation 5.3.2. The peaks at the transitions are described quite well by just the first term in the eigenfunction expansion. Away from the peaks, however, we find that the noise is not captured by the approximation based on the first term. It is particularly clear in figure 5.4 that something is missing from this approximation. The features that are simply due to the SSET alone are not captured, such as the dip at $\Delta E = 0$ and the Fano factor of 2 far from resonance. We can understand this better by considering the meaning of the eigenvectors and eigenvalues of the Liouvillian [64, 86]. The meaning of the eigenvalues when the resonator can be described by a thermal state was previously discussed in Chapter 4. We repeat some of this here for clarity.

In the limit $\kappa \to 0$ the SSET-resonator system becomes uncoupled and the eigenvectors and eigenvalues of the system can be expressed in terms of those of the individual subsystems, namely the SSET and the resonator. When the resonator is decou-

pled from the SSET it still remains coupled to the external bath and its smallest (non-zero) eigenvalues are integer multiples of γ_{ext} (Section 4.3) [86]. Thus the smallest of these eigenvalues corresponds to the energy relaxation rate of the resonator, $-\gamma_{\mathrm{ext}}$, and hence we can infer that the corresponding eigenfunction describes fluctuations in the resonator's energy. There are also a set of eigenfunctions (and corresponding eigenvalues) that describe fluctuations in the SSET charge state. In the uncoupled regime the current noise of the SSET can be obtained using equation 5.3.2, with the sum running over just the SSET eigenvalues, though we already know the result will be given by equation 3.2.2.

For the coupled SSET-resonator system we can still identify the eigenvalues and eigenvectors as corresponding to one or other of the subsystems by looking at their behaviour for large detunings (i.e. large $|\Delta E|$) where the systems are effectively decoupled. The first few eigenvalues, which correspond to the resonator, are shown (for the slow resonator case $\Omega = 0.12\,\Gamma$) in figure 5.8 as a function of ΔE. These first few eigenvalues indeed converge towards $-\gamma_{\mathrm{ext}}$, $-2\gamma_{\mathrm{ext}}$, ... for large detunings. Thus at least for large detunings the first eigenstate, $|r_1\rangle\!\rangle$, should therefore represent fluctuations which change the resonator energy. This can be confirmed by performing an eigenfunction expansion of the variance in the resonator energy,

$$\left\langle \bar{n}^2 \right\rangle = \sum_{p=1} \langle\!\langle l_0 | \mathcal{N} | r_p \rangle\!\rangle \langle\!\langle l_p | \mathcal{N} | r_0 \rangle\!\rangle \,, \tag{5.5.1}$$

where $\mathcal{N}\,|\rho(t)\rangle\!\rangle \equiv n\rho(t) = a^\dagger a \rho(t)$. As before we plot the resonator Fano factor, $F_n = \left\langle \bar{n}^2 \right\rangle / \langle n \rangle$, rather than the variance. The full numerical calculation of the energy variance is compared with approximations based on the first term and first 5 terms in the eigenfunction expansion in figure 5.9. It is clear that only the first term is needed to describe the energy fluctuations for large detunings as we expect. However, the approximation based on the first term also describes the energy fluctuations rather well at the peaks where the transitions occur, but not in between where the resonator is in a limit cycle state. However, figure 5.9 also shows that we can describe the energy fluctuations throughout by using more terms in the eigenfunction expansion.

We are now in a position to understand why the calculation of the current noise using just the first term of the eigenvector expansion works as well as it does and to see how this can be easily improved upon. Comparing figures 5.2 and 5.9 it is clear that the single-term approximation to the current noise matches the numerical results well around the two peaks marking the transitions (between the fixed point and limit cycle states) where the first term in the eigenfunction expansion also describes the energy fluctuations in the resonator accurately. The fact that the first term in the expansion does not capture the current noise far from resonance is not surprising as it only describes fluctuations in the resonator state and does not include the fluctuations of the

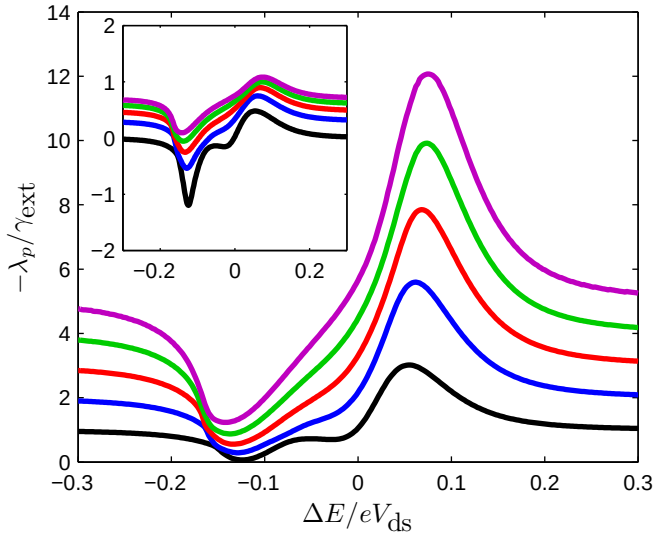

Figure 5.8. The five smallest (non-zero) eigenvalues as a function of the detuning, ΔE for $\Omega = 0.12\,\Gamma$, with the other parameters given in figure 5.1. The inset shows $\log_{10}(-\lambda_p/\gamma_{\rm ext})$. The eigenvalues differ from each other by less than one order of magnitude throughout and converge towards integer multiples of $\gamma_{\rm ext}$ for large $|\Delta E|$.

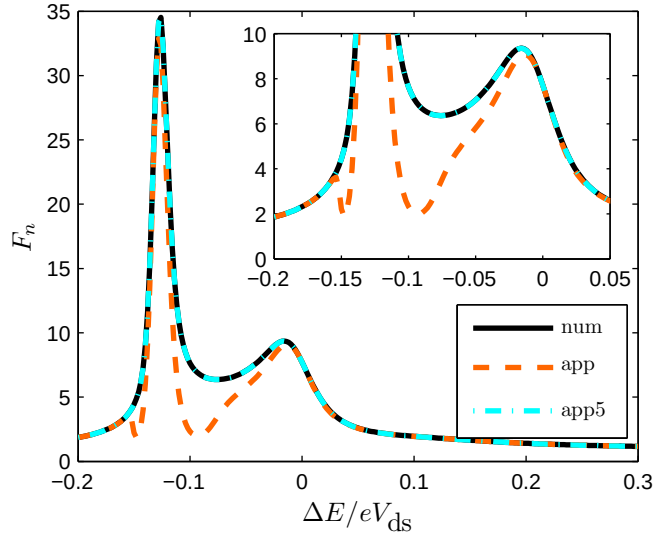

Figure 5.9. Energy fluctuations of the resonator, F_n, as a function of ΔE for $\Omega = 0.12\,\Gamma$, with the other parameters given in figure 5.1. The three curves show the full numerical calculation, *num*, and approximations using just the first term, *app* and the first five terms, *app5*, of the eigenfunction expansion (equation 5.5.1) respectively.

SSET degrees of freedom. We can easily obtain better agreement for large detunings by extending our approximation to include the contribution of an uncoupled SSET, $F_I^{\kappa=0}(0)$, given by equation 3.2.2. Better agreement within the limit cycle region can be attained by using sufficient terms in our approximation to ensure that the fluctuations in the resonator energy are described accurately. Thus we arrive at our final approximate expression for the zero frequency current noise

$$F_I(0) \simeq F_I^{\kappa=0} - 2\sum_{p=1}^{m} \frac{\langle\langle l_0|\mathcal{I}_L|r_p\rangle\rangle\langle\langle l_p|\mathcal{I}_L|r_0\rangle\rangle}{\lambda_p e\,\langle I\rangle}, \tag{5.5.2}$$

where m should be large enough so that the corresponding number of terms can be used to calculate $\langle\bar{n}^2\rangle$ accurately (via equation 5.5.1). In this case we find $m = 5$ is sufficient, and the current noise calculated this way agrees very well at almost all points as shown in figures 5.2–5.4. The one area where good agreement is still lacking using equation 5.5.2 is within the limit cycle region for $\Omega = 10\,\Gamma$, shown in figure 5.4. This is because we have approximated the contribution to the current noise arising from the SSET terms by the uncoupled value. In fact these SSET terms are strongly modified due to the resonant absorption of energy by the resonator from the Cooper pairs at this point.

From these approximations it is clear that in the vicinity of the resonator transitions the current noise is largely determined by the slow fluctuations in the energy of the resonator. This is because the current depends in the first instance on the resonator position and hence on the latter's energy (as this is slowly changing compared to its period). Thus the current fluctuations depend strongly on the fluctuations of the resonator energy, rather than those of higher moments of the resonator. Thus when $\langle\bar{n}^2\rangle$ depends on more than one term in the expansion, the current noise does also.

It is important to note that even in the regions where including just the first term in the eigenfunction expansion describes the current noise fairly well this is not simply because the associated eigenvalue is very much smaller than all the others. We can see from figure 5.8 that (for these parameters) an overwhelming difference between the slowest two eigenvalues never develops and from figure 5.10, that the relative size of the corresponding matrix elements is important in causing the first term in the eigenfunction expansion to dominate.

The other frequency regimes also show interesting features in the expansion of the resonator Fano factor. As shown in figure 5.11 we again require more than one term to fully describe F_n in the limit cycle region for the case of $\Omega = \Gamma$. In the low frequency regime (figure 5.9) there was a smooth deviation of the one term approximation from the actual value in the limit cycle region. In the inset of figure 5.11 it is clear that instead there are abrupt changes seen in the one term approximation, at $\Delta E \simeq -0.2\,eV_{\rm ds}$ and also just to the right of $\Delta E = 0$. Note that these changes are also seen in the one term

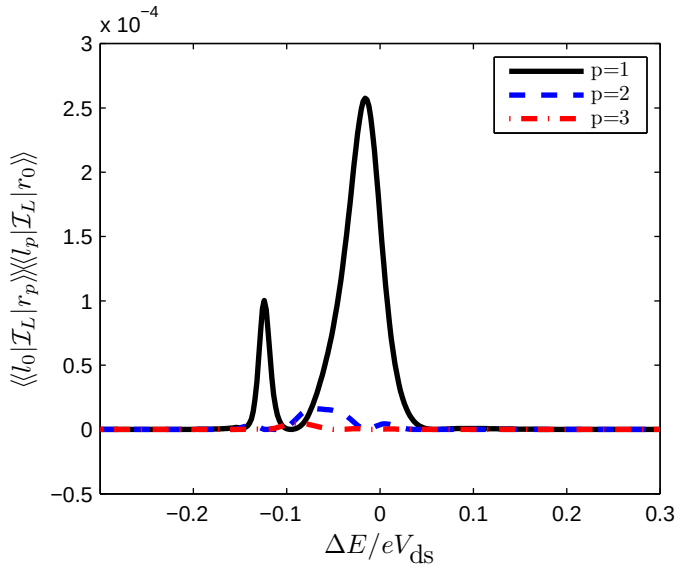

Figure 5.10. Variance part of the current noise for the first 3 terms of the expansion (equation 5.3.2) for $\Omega = 0.12\,\Gamma$, with the other parameters given in figure 5.1. The $p = 1$ variance is much larger in the same regions as the peaks in the corresponding plot of the current noise, figure 5.2.

approximation of the current noise, although they cannot be clearly seen in figure 5.3. The reason for this can be understood from a plot of the eigenvalues that correspond to the terms used in the expansion. As shown in figure 5.12 there are a number of crossings present in the eigenvalues. There is a crossing at $\Delta E \simeq -0.2\,eV_{\rm ds}$ and also for $\Delta E > 0$ (although less clear). The point at which the single term approximation fails corresponds exactly to these crossings.

From a plot of the first few terms in the eigenfunction expansion of F_n, which is shown in figure 5.13, it can be seen that for the majority of the limit cycle region only one term is required. However, this term does not necessarily correspond to the smallest magnitude eigenvalue. At the crossing for $\Delta E \simeq -0.2\,eV_{\rm ds}$ the new smallest eigenvalue develops into the bistable switching rate and correctly captures the noise in the bistable region. However, when the system is not bistable it is not the correct term to describe F_n or $F_I(0)$. It can be seen from figures 5.12 and 5.13 that it is the same eigenvalue that leads to the correct single term approximation to F_n but that it undergoes a number of crossings.

For the case of $\Omega = 10\,\Gamma$, as shown in figure 5.14, the smallest eigenvalue is sufficient to capture F_n except for near to the transitions. The eigenvalues do not cross at this point, as shown in figure 5.15, but the smallest two become close. During the transition region the first few terms have an important contribution. The one term approximation to the current noise at the transition was still quite good since the first

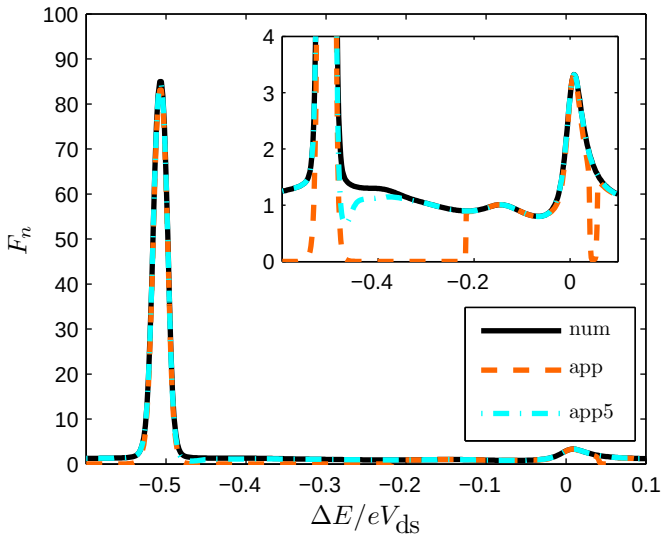

Figure 5.11. Energy fluctuations of the resonator, F_n, as a function of ΔE for $\Omega = \Gamma$, with the other parameters given in figure 5.1. The three curves show the full numerical calculation, *num*, and approximations using just the first term, *app* and the first five terms, *app5*, of the eigenfunction expansion (equation 5.5.1) respectively.

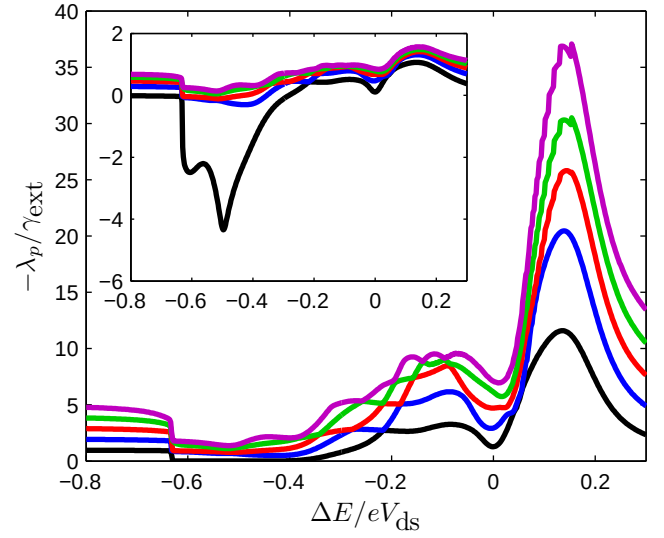

Figure 5.12. The five smallest (non-zero) eigenvalues as a function of the detuning, ΔE for $\Omega = \Gamma$, with the other parameters given in figure 5.1. The inset shows $\log_{10}(-\lambda_p/\gamma_{\rm ext})$. A clear separation of eigenvalues can be seen in the bistable region.

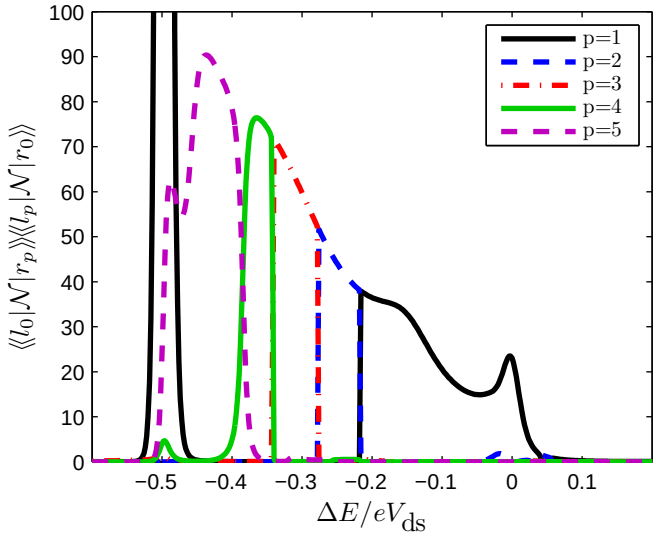

Figure 5.13. First five terms in the expansion of $\langle \bar{n}^2 \rangle$ (equation 5.5.1) for $\Omega = \Gamma$, with the other parameters given in figure 5.1. One term generally dominates but it does not always correspond to the smallest eigenvalue.

term captures most of the peak and the eigenvalues provide a large scaling. The state of the system during the transition is similar to that in the limit cycle for $\Omega = 0.12\,\Gamma$ where more than one term was also required to describe F_n. The state of the resonator at these points was previously described in Section 3.4 where a discussion of the state of the resonator during the continuous transition was made. In these cases the $P(n)$ distribution consists of a Gaussian like shape with a sharp cut-off at $n = 0$ due to the width being larger than $\langle n \rangle$, an example of which was shown in figure 3.9. For $\Omega = 10\,\Gamma$ and $\Omega = \Gamma$ we obtain 'good' limit cycle states (i.e. $P(0) \simeq 0$) in the regions where only one term is required to describe F_n. For $\Omega = 0.12\,\Gamma$ this is not the case for the parameters used here.

In conclusion, for the regimes studied in this chapter, the majority of states of the system have a value of F_n that can be described by a single term in an eigenfunction expansion of the Liouvillian. The exception to this is limit cycle states where $P(0) \not\simeq 0$. The corresponding term in an eigenfunction expansion of the current noise also describes the dominant contribution to $F_I(0)$ that is different from the current noise of an uncoupled SSET.

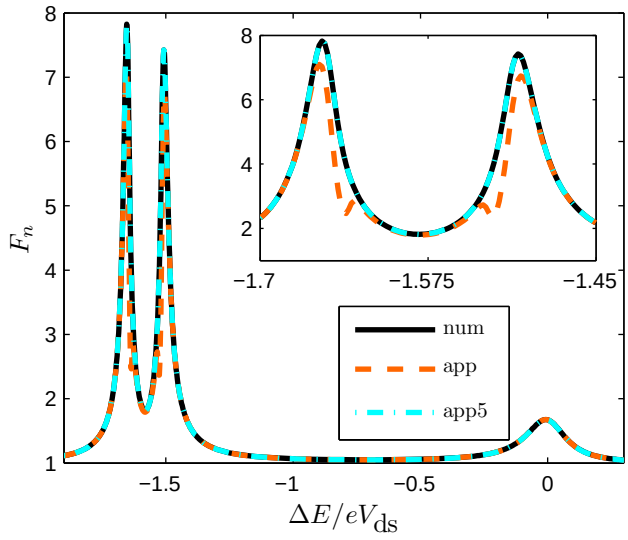

Figure 5.14. Energy fluctuations of the resonator, F_n, as a function of ΔE for $\Omega = 10\,\Gamma$, with the other parameters given in figure 5.1. The three curves show the full numerical calculation, *num*, and approximations using just the first term, *app* and the first five terms, *app5*, of the eigenfunction expansion (equation 5.5.1) respectively.

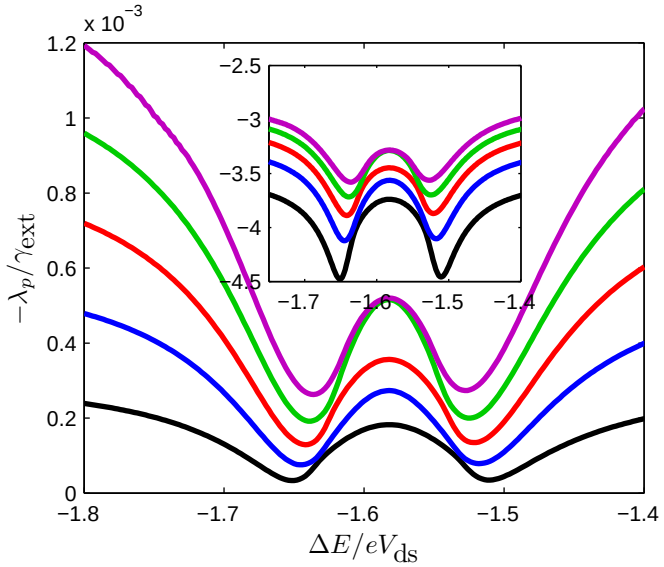

Figure 5.15. The five smallest (non-zero) eigenvalues as a function of the detuning, ΔE for $\Omega = 10\,\Gamma$, with the other parameters given in figure 5.1. The inset shows $\log_{10}(-\lambda_p/\gamma_{\rm ext})$.

Chapter 6

Finite Frequency Resonator Noise Spectra

In this chapter we discuss the dynamics of the limit cycle region in some more detail. In order to do this we make use of several finite frequency noise spectra of resonator operators. Throughout we make comparisons between the SSET-resonator system and a laser. In particular we investigate the linewidth of the resonator, which is introduced in Section 6.1. We show that as for a laser the linewidth in the limit cycle region is dominated by phase diffusion. In Sections 6.2 and 6.3 we give the results for the $\Omega \gg \Gamma$ and $\Omega \simeq \Gamma$ regimes respectively.

6.1 Calculation of the resonator linewidth

The linewidth of a laser, γ_Ω, is defined as the width of the peak in the emission spectrum, at the frequency of the resonator [77]. Above threshold the linewidth of a laser becomes very narrow indicating an almost monochromatic light source. The emission spectrum is defined as,

$$S_{a,a^\dagger}(\omega) = \lim_{t\to\infty} \int_{-\infty}^{\infty} d\tau \left\langle \{\bar{a}(t+\tau), \bar{a^\dagger}(t)\} \right\rangle e^{i\omega\tau}. \tag{6.1.1}$$

The numerical calculation of spectra such as these was described in Section 2.6. We could equally use $S_{a^\dagger,a}(\omega)$, in the definition of the emission spectrum, since for symmetrized noise $S_{a,a^\dagger}(\omega) = S_{a^\dagger,a}(-\omega)$. We choose $S_{a,a^\dagger}(\omega)$, since it has the peak for $\omega > 0$. The correlation function, in the emission spectrum, corresponds to putting in a photon at time t then removing it at $t + \tau$. The spectrum was measured in the experiment of a SSET coupled to a superconducting stripline resonator [30]. To do this a small microwave drive was applied to the cavity and the emission from the cavity was

measured as the frequency of the drive was varied.

We can identify two sources of noise in the resonator that contribute to the finite linewidth. These are the amplitude noise and the phase noise. The amplitude noise is characterized by the amplitude relaxation rate, γ_n. In the limit cycle region the amplitude noise leads to the finite width of of the ring in the Wigner distribution (figure 3.1b). The phase noise is characterized by the phase diffusion rate, γ_ϕ. In a laser the phase noise is due to jumps in phase associated with spontaneous emission [77]. The equivalent process in the SSET-resonator system is the energy exchange between the Cooper pairs and resonator.

The linewidth can depend on one or both of the diffusion rates. In order to show, on which one it depends it is helpful to be able to calculate the two rates independently. The amplitude relaxation rate can be found from the spectrum of amplitude fluctuations,

$$S_{n,n}(\omega) = \lim_{t\to\infty} \int_{-\infty}^{\infty} d\tau \left\langle \{\bar{n}(t+\tau), \bar{n}(t)\} \right\rangle e^{i\omega\tau}, \tag{6.1.2}$$

which will have a peak at $\omega = 0$ with a width γ_n.

In order to calculate the spectrum of phase fluctuations we must first define an operator for the phase. There is much debate over the correct form for the phase operator [73]. We choose to use the Susskind-Glogower operators [98, 99], which are valid so long as the occupation of the vacuum state is negligible [73]. This condition is not restrictive since for a limit cycle state, where the phase is of interest, the condition must be met. The two operators are analogous to the exponential phase factors, $e^{\pm i\phi}$, and are defined,

$$\begin{aligned} p &\equiv (n+1)^{-\frac{1}{2}} a = (aa^\dagger)^{-\frac{1}{2}} a = \sum_{N=0}^{\infty} |N\rangle\langle N+1| \,, \\ p^\dagger &\equiv a^\dagger (n+1)^{-\frac{1}{2}} = a^\dagger (aa^\dagger)^{-\frac{1}{2}} = \sum_{N=0}^{\infty} |N+1\rangle\langle N| \,. \end{aligned} \tag{6.1.3}$$

We define the phase noise spectrum in a similar manner to the emission spectrum,

$$S_{p,p^\dagger}(\omega) = \lim_{t\to\infty} \int_{-\infty}^{\infty} d\tau \left\langle \{\bar{p}(t+\tau), \bar{p^\dagger}(t)\} \right\rangle e^{i\omega\tau}. \tag{6.1.4}$$

For a laser above threshold the linewidth is dominated by the phase noise [77]. In order to show that this is also true for the SSET-resonator system we derive a relationship between the emission and phase noise spectra that is valid for a laser. Under the assumption that $\gamma_\phi \ll \gamma_n$, the amplitude relaxation occurs on a much faster time-scale than the phase relaxation. If this is true then we can neglect fluctuations in the amplitude and assume that it takes its steady-state value. The following relationship between

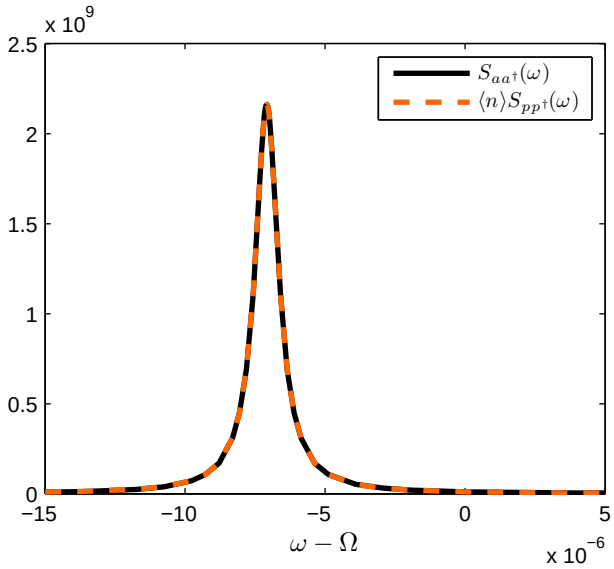

Figure 6.1. Shows that $S_{aa^\dagger}(\omega) = \langle n \rangle S_{pp^\dagger}(\omega)$ which means that amplitude and phase noise are uncorrelated as discussed around equation 6.1.5. Parameters are $\Omega = 10\,\Gamma$, $\Delta E = -1.58\,eV_{\rm ds}$, $\kappa = 0.003$, $\gamma_{\rm ext} = 3 \times 10^{-4}\,\Gamma$, $E_J = 1/16\,eV_{\rm ds}$, $r = 1$ and $\bar{n}_{\rm ext} = 0$

the emission and phase noise spectra in the limit cycle region can then be derived,

$$\begin{aligned} S_{a,a^\dagger}(\omega) &= \lim_{t\to\infty} \int_{-\infty}^{\infty} d\tau \left\langle \{(n(t+\tau)+1)^{1/2}\bar{p}(t+\tau), (n(t)+1)^{1/2}\bar{p^\dagger}(t+\tau)\} \right\rangle e^{i\omega\tau} \\ &= \lim_{t\to\infty} \int_{-\infty}^{\infty} d\tau \left\langle \{\langle n\rangle^{1/2}\,\bar{p}(t+\tau), \langle n\rangle^{1/2}\,\bar{p^\dagger}(t+\tau)\} \right\rangle e^{i\omega\tau} \\ &= \langle n \rangle\, S_{p,p^\dagger}(\omega). \end{aligned} \tag{6.1.5}$$

In the first line we have used the definition of the phase operators given in equation 6.1.3 to replace a and $a^\dagger$. In the second line we have replaced $n(t)$ and $n(t+\tau)$ with the steady-state value, $\langle n \rangle$, and additionally assumed $\langle n \rangle \gg 1$, which is true for the limit cycle state. Removing $\langle n \rangle$ from the integral then leads directly to the final line. In figure 6.1 we show the relationship to hold for the SSET-resonator system for a set of parameters in the limit cycle region. Below we will show in a different manner that the relationship holds throughout the limit cycle region.

It can also be seen in figure 6.1 that the peak in the emission spectrum is symmetric. We would expect this to be the case for all peaks in resonator spectra. The reason for this is that, as discussed in Section 4.5, the asymmetric shape in the current noise peaks is due to the back-action of the resonator on the SSET. The asymmetry was removed by the addition of a large external damping or temperature for the resonator. Since the dissipation in the SSET is large (due to the large value of Γ in comparison to other time-

scales) any back-action effects will be removed and peaks in the spectra of resonator operators will be symmetric. A small renormalization of the resonator frequency to the value Ω_R can also be seen in the figure.

6.2 Phase Diffusion for $\Omega \gg \Gamma$

In Section 5.5 we found that the $\langle \bar{n}^2 \rangle$ could be described by a single term of an eigenfunction expansion when the resonator was in a fixed point or good limit cycle state. If this is true then $S_{n,n}(\omega)$ is also described by a single term in an eigenfunction expansion since the same matrix element part will appear. Where the single term approximation is valid, $S_{n,n}(\omega)$ will be given by a Lorentzian peak of the form,

$$\begin{aligned} S_{n,n}(\omega) &= 4\Re \sum_{p=1}^{\infty} \frac{1}{-i\omega - \lambda_p} \langle\langle l_0 | \mathcal{N} | r_p \rangle\rangle \langle\langle l_p | \mathcal{N} | r_0 \rangle\rangle \\ &\simeq 4\Re \left[\frac{1}{-i\omega - \lambda_1} \right] \langle\langle l_0 | \mathcal{N} | r_1 \rangle\rangle \langle\langle l_1 | \mathcal{N} | r_0 \rangle\rangle \\ &= \frac{4 \langle \bar{n}^2 \rangle \gamma_n}{\omega^2 + \gamma_n^2}. \end{aligned} \tag{6.2.1}$$

If the single term approximation is valid then $-\lambda_1 = \gamma_n$ and so the amplitude diffusion rate can be calculated without resorting to a calculation of the full spectrum of amplitude fluctuations. In figure 6.2 we compare the width of the $\omega = 0$ peak in the $S_{n,n}(\omega)$ spectrum as determined from a Lorentzian fit to the smallest non-zero eigenvalue of the Liouvillian. They are in agreement except for around the transition region where we do not expect the expansion to work (see Section 5.5).

Similarly the peak in the emission spectrum is also likely to be described by a Lorentzian with a width determined by the real part of the eigenvalue nearest $-i\Omega$. The emission spectrum will be of the form,

$$\begin{aligned} S_{a,a^\dagger}(\omega) &= 4\Re \sum_{p=1}^{\infty} \frac{1}{-i\omega - \lambda_p} \langle\langle l_0 | \mathcal{A} | r_p \rangle\rangle \langle\langle l_p | \mathcal{A}^\dagger | r_0 \rangle\rangle \\ &\simeq 4\Re \left[\frac{1}{-i\omega - \lambda_1} \right] \langle\langle l_0 | \mathcal{A} | r_1 \rangle\rangle \langle\langle l_1 | \mathcal{A}^\dagger | r_0 \rangle\rangle \\ &= \frac{4 \langle n \rangle \gamma_\Omega}{(\omega - \Omega_R)^2 + \gamma_\Omega^2}. \end{aligned} \tag{6.2.2}$$

where $\mathcal{A} |\rho(t)\rangle\rangle = \frac{1}{2}(a\rho(t) + \rho(t)a)$. As shown in figure 6.2 the width of the peak in the emission spectrum is in agreement with the eigenvalue. If the single term approximation is valid we should also find that $m_e^1 = \langle\langle l_0 | \mathcal{A} | r_1 \rangle\rangle \langle\langle l_1 | \mathcal{A}^\dagger | r_0 \rangle\rangle = \langle n \rangle$, which is confirmed in figure 6.3a. For both $S_{n,n}(\omega)$ and $S_{a,a^\dagger}(\omega)$ we can also check the size of the next term in the eigenfunction expansion to ensure that it is small. For the results

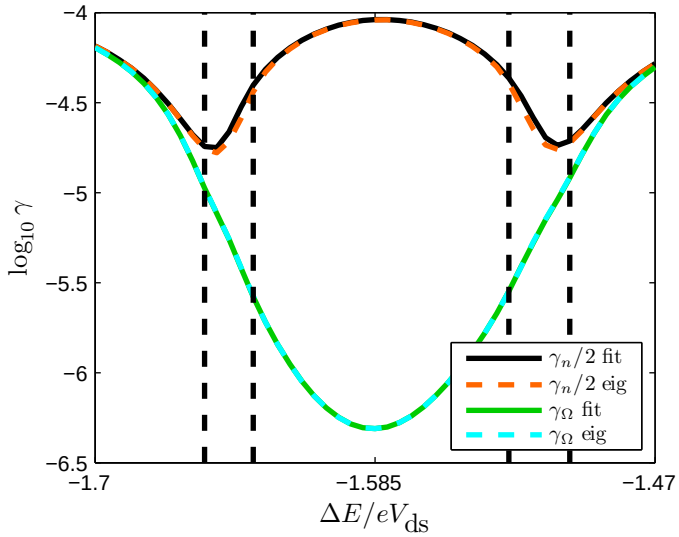

Figure 6.2. Width of zero frequency peak in the $S_{n,n}(\omega)$ spectrum as determined from a Lorentzian fit ($\gamma_n/2$ fit) and from the smallest nonzero eigenvalue ($\gamma_n/2$ eig). Linewidth of the resonator as determined from a Lorentzian fit (γ_Ω fit) and from the eigenvalue (γ_Ω eig). Parameters are the same as in figure 6.1. Within the pairs of vertical dashed lines the $P(n)$ distribution has a peak at $n \neq 0$ but $P(0) \geq 1 \times 10^{-5}$, which we define here as the transition regions.

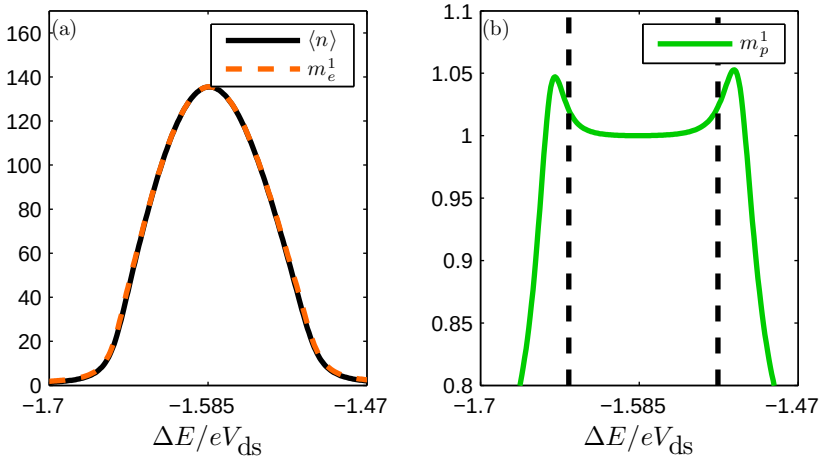

Figure 6.3. (a) shows the agreement of $\langle n \rangle$ and m_e^1 as explained in the text. (b) shows $m_p^1 = 1$ and the vertical dashed lines indicate the good limit cycle region as defined in figure 6.2. Parameters are the same as in figure 6.1.

in this chapter, unless otherwise stated, this check has been made and the contributions from other terms can be neglected.

For a thermal state (which is the case away from the resonance peak) we expect, from Section 4.3, that $\gamma_\Omega = \gamma_n/2$. At the edges of figure 6.2 it can be seen that this is indeed the case. Within the limit cycle region there is a separation between γ_n and γ_Ω of at least one order of magnitude. Additionally following the transition γ_n increases while γ_Ω continues to decrease to a minima at the resonance.

Within the limit cycle region we can also perform an eigenfunction expansion of $S_{p,p^\dagger}(\omega)$. Just like for $S_{n,n}(\omega)$ and $S_{a,a^\dagger}(\omega)$ only a single term is required. We obtain,

$$\begin{aligned} S_{p,p^\dagger}(\omega) &= 4\Re \sum_{p=1} \frac{1}{-i\omega - \lambda_p} \langle\langle l_0 | \mathcal{P} | r_p \rangle\rangle \langle\langle l_p | \mathcal{P}^\dagger | r_0 \rangle\rangle \\ &\simeq \frac{4 \left\langle pp^\dagger \right\rangle \gamma_\Omega}{(\omega - \Omega_R)^2 + \gamma_\Omega^2}, \end{aligned} \tag{6.2.3}$$

where $\mathcal{P} \, |\rho(t)\rangle\rangle = \frac{1}{2}(p\rho(t) + \rho(t)p)$. Clearly we must have $\gamma_\Omega = \gamma_\phi$ within the limit cycle region for both $S_{p,p^\dagger}(\omega)$ and $S_{a,a^\dagger}(\omega)$ to be described by a single term in the expansion. As further confirmation of the relationship in equation 6.1 we should also find that $m_p^1 = \langle\langle l_0 | \mathcal{P} | r_1 \rangle\rangle \langle\langle l_1 | \mathcal{P}^\dagger | r_0 \rangle\rangle = \left\langle pp^\dagger \right\rangle = 1$, which is shown in figure 6.3b. Note that the value of m_p^1 has no meaning outside the limit cycle region.

In figure 6.4 we again show γ_n and γ_Ω. Also shown is the real part of the next closest eigenvalue to $-i\Omega$ (labelled $\gamma_\Omega(2)$). It can be seen that outside the limit cycle

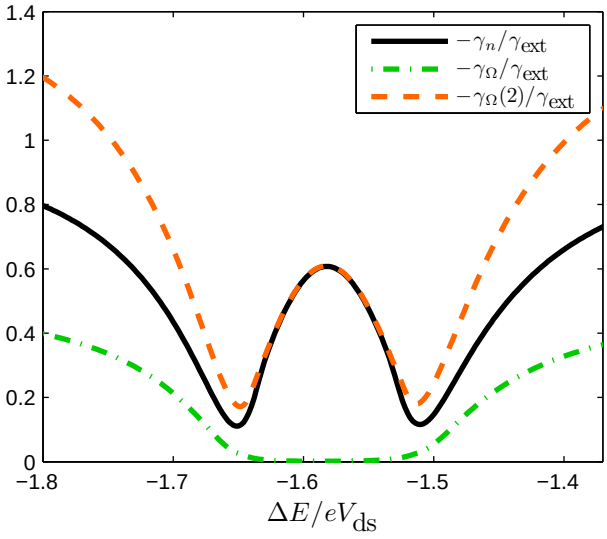

Figure 6.4. Amplitude relaxation rate γ_n and the real part of the two eigenvalues nearest $-i\Omega$, γ_Ω and $\gamma_\Omega(2)$. Parameters are the same as in figure 6.1

region it approaches the expected value, from Section 4.3, of $-\frac{3}{2}\gamma_n$. Within the limit cycle region it is equal to γ_n. This suggests that this next term in the expansion is the contribution to the linewidth due to the amplitude noise in the limit cycle, which is small due to the large separation of the eigenvalues.

For a laser the phase diffusion rate has a particularly simple form [48],

$$\gamma_\phi^{laser} = \frac{G}{8\langle n\rangle}, \tag{6.2.4}$$

where G is the gain of the laser. However, it is not entirely clear what the gain is for the SSET-resonator system and $\langle n\rangle$ cannot be varied independently from the parameters of the system, on which the gain will depend. However, we can at least show qualitatively that there is an inverse relationship between $\langle n\rangle$ and γ_ϕ. In figures 6.5 and 6.6 we show $\langle n\rangle$ and γ_ϕ for varying values of κ and $\gamma_{\rm ext}$. The detuning is chosen to be at the one photon resonance in the centre of figure 6.2. It can be seen that as $\langle n\rangle$ increases γ_ϕ does indeed reduce.

In examining the off-resonant behaviour of $\langle n\rangle$ and γ_ϕ we observe a striking deviation from the expected relationship between the two values. We now fix $\gamma_{\rm ext}$ and vary the detuning about the one photon resonance for a range of coupling strengths. Similar plots were produced in figure 3.8 but here we go to higher coupling strengths. The value of $\langle n\rangle$ is shown in figure 6.7. For increasing coupling $\langle n\rangle$ reaches a maximum and then shows a decrease. The peak also becomes wider for larger coupling as this

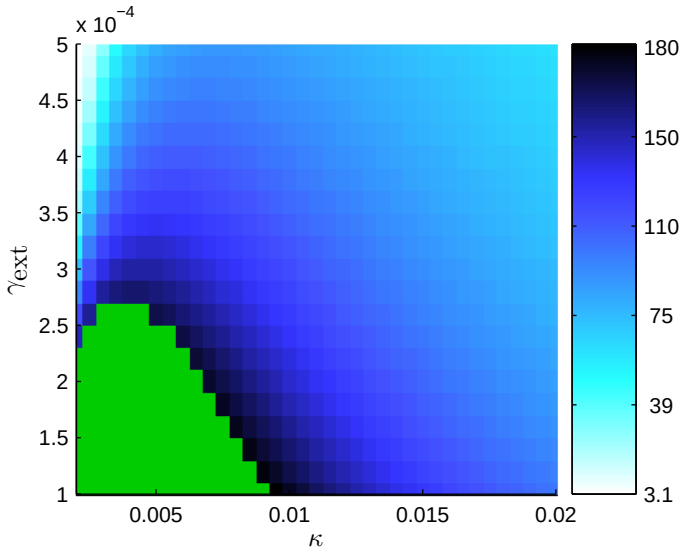

Figure 6.5. Value of $\langle n \rangle$ as a function of the coupling and external damping with the other parameters given in figure 6.1. The green region in the bottom left has no results due to an insufficient number of resonator states. Except for a small strip for large γ_{ext} and small κ (top left) the resonator is in the limit cycle state.

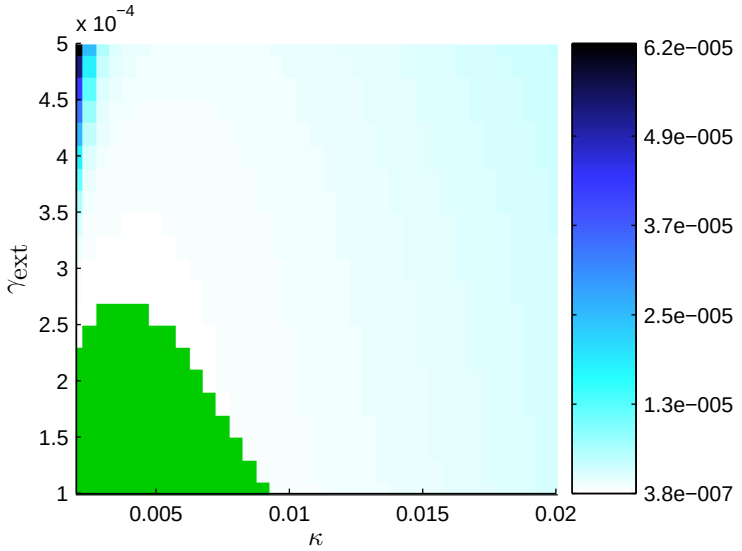

Figure 6.6. Value of $-\Re\lambda_\Omega$ as a function of the coupling and external damping with the other parameters given in figure 6.1. The green region in the bottom left has no results due to an insufficient number of resonator states. Except for a small strip for large γ_{ext} and small κ (top left) the resonator is in the limit cycle state and so $-\Re\lambda_\Omega = \gamma_\phi$.

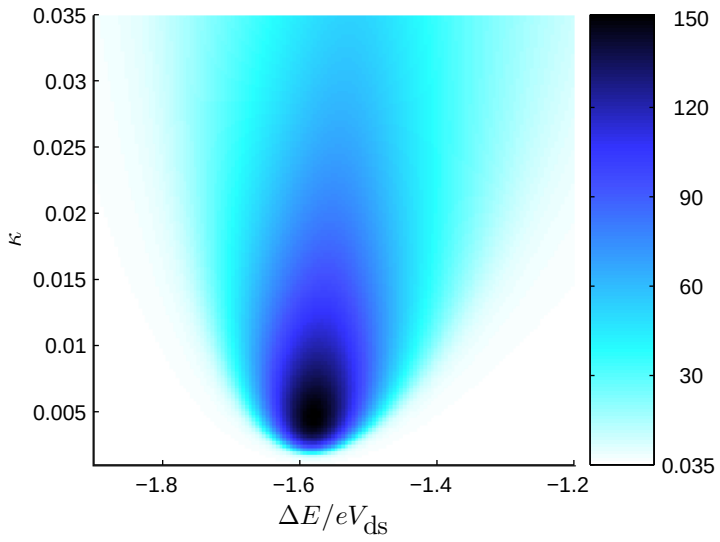

Figure 6.7. Value of $\langle n \rangle$ for varying ΔE and κ with the other parameters given in figure 6.1.

maximum is approached.

In figure 6.8 the value of F_n is shown for the same parameters. Peaks are seen in F_n at the transitions between fixed point and limit cycle behaviour as discussed in previous chapters. Beyond the peak in $\langle n \rangle$ the value of F_n continues to decrease and in doing so drops below one. This corresponds to a sub-Poissonian $P(n)$, which is also observed in the micromaser (see Section 3.7) but not a conventional laser.

In figure 6.9 the linewidth, γ_Ω, as calculated from the eigenvalues is shown. Within the limit cycle region this can be interpreted as γ_ϕ where we focus our attention. The region in which $\gamma_\Omega = \gamma_\phi$ is indicated in figure 6.9. For low coupling the peak in $\langle n \rangle$ corresponds to a minimum in γ_ϕ. But for large coupling we see a deviation from this behaviour. Two minima are seen in γ_ϕ with the peak in $\langle n \rangle$ now corresponding to a local maximum in γ_ϕ.

For the parameters here the single term approximation, given in equation 6.2.2, always describes the peak in the emission spectrum. We show the effect of the changing eigenvalue on the height of the peak in the emission spectrum in figure 6.10. It can be seen that the increased coupling causes a splitting of the peak in the emission spectrum. This splitting is not responsible for the double peak seen in the emission spectrum of the experiment [30]. In the experiment a matching feature was observed in the current, which is not the case here (the current follows $\langle n \rangle$ as discussed in Section 3.4). Note also that the splitting is only as a function of the detuning, there is still just a single Lorentzian peak in the emission spectrum.

The amplitude relaxation rate, shown in figure 6.11, does not show any unexpected

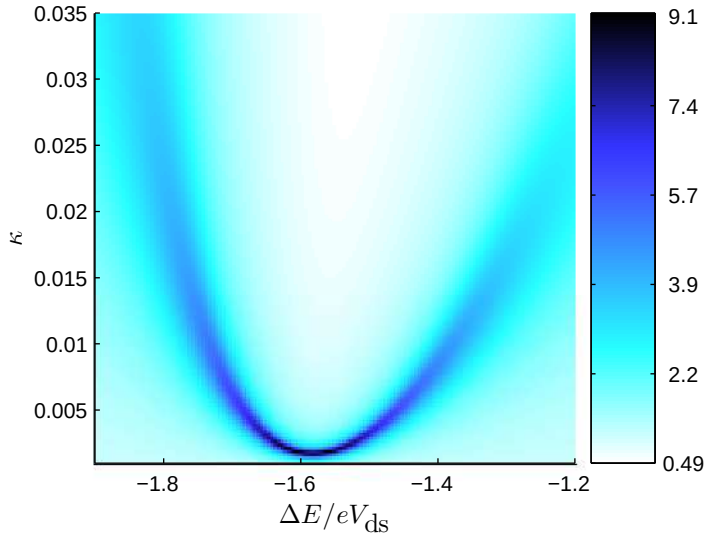

Figure 6.8. Value of F_n for varying ΔE and κ with the other parameters given in figure 6.1.

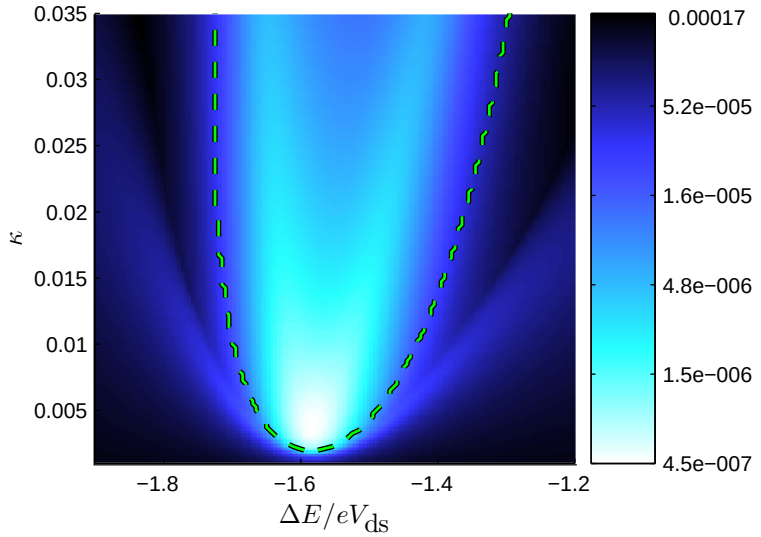

Figure 6.9. Linewidth of the resonator, γ_Ω, for varying ΔE and κ with the other parameters given in figure 6.1. Colours are on a $\log_{10}$ scale. Within the region given by the dashed lines the resonator is in a limit cycle state and $P(0) \leq 1 \times 10^{-5}$ so $\gamma_\Omega = \gamma_\phi$.

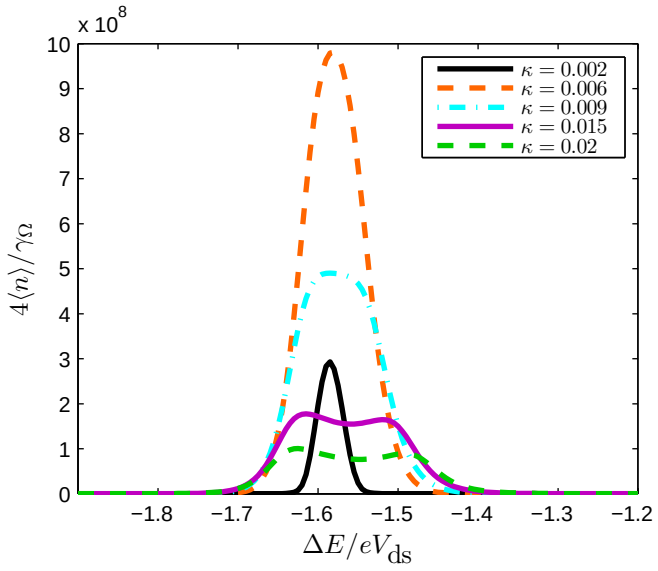

Figure 6.10. Height of peak in emission spectrum given by $4\langle n\rangle/\gamma_\Omega$ for a few values of κ as a function of the detuning with the other parameters given in figure 6.1.

behaviour and shows an increase with increasing coupling. The fast relaxation rate can be associated with the low value of F_n. We know the term associated with γ_n to be responsible for the modifications to the zero frequency current noise in the limit cycle region as discussed in Section 5.5. It may then be surprising that as shown in figure 6.12 there is a clear splitting of the minimum in $F_I(0)$ into two minima as the coupling is increased. The variance part of the current noise must therefore depend on the phase diffusion rate, which leads to an experimental signature of this behaviour.

6.3 Phase Diffusion in the $\Omega \simeq \Gamma$ regime

In this section we look at the finite frequency eigenvalues and phase diffusion for the strongly interacting regime. We do not investigate phase diffusion in the slow resonator case since, as discussed at the end of Section 5.5, we do not obtain a good limit cycle and so cannot define a phase operator in this regime. In figure 6.13 we repeat figure 6.3 but this time for $\Omega = \Gamma$. The figure confirms that the emission spectrum can be described by a single term in the eigenfunction expansion and that the linewidth in the limit cycle region will be given by the phase diffusion rate.

Figure 6.14 shows the real part of the eigenvalues nearest to $-i\Omega$ for $\Omega = \Gamma$. The parameters are chosen to be the same as those used in Chapter 5 for easy comparison. In particular the smallest few real eigenvalues, shown in figure 5.12, should be compared with figure 6.14. It can be observed in figure 6.14 that within the limit cycle region there

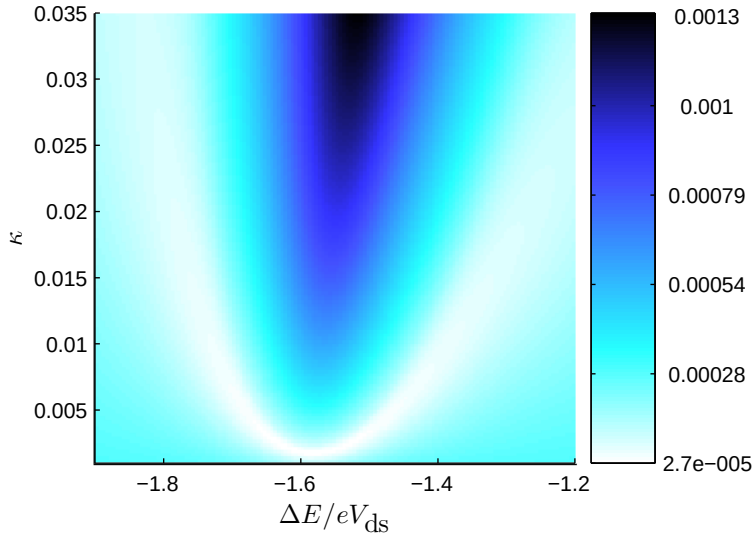

Figure 6.11. Value of γ_n for varying ΔE and κ with the other parameters given in figure 6.1.

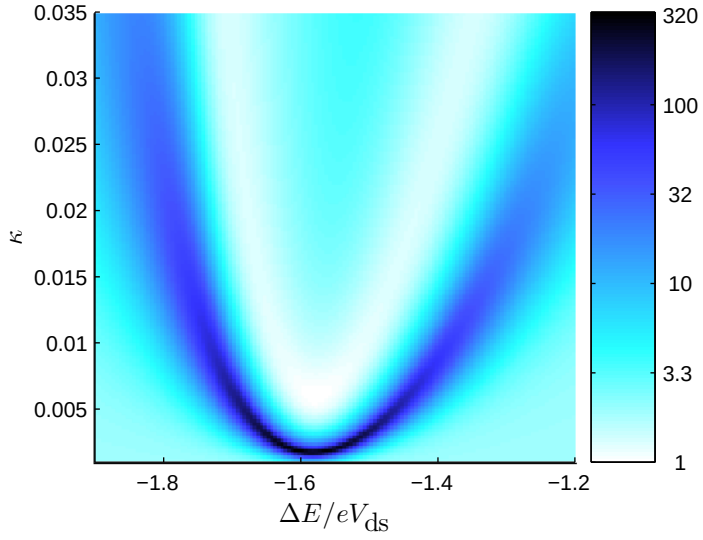

Figure 6.12. Value of $F_I(0)$ for varying ΔE and κ with the other parameters given in figure 6.1. Colours are on a $\log_{10}$ scale

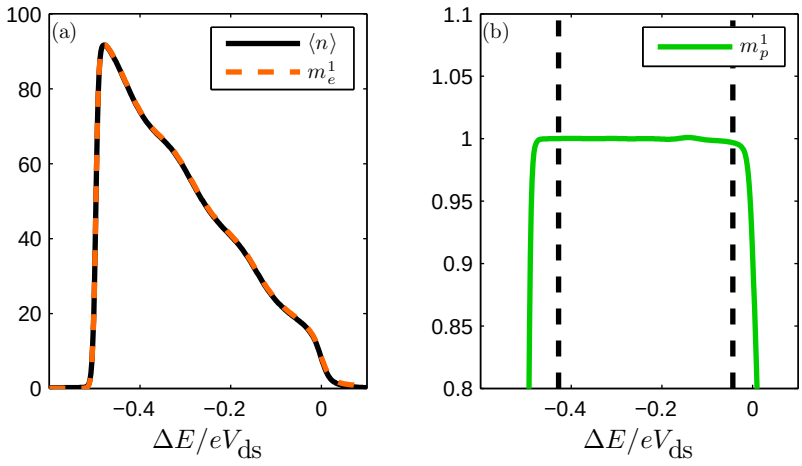

Figure 6.13. (a) shows the agreement of $\langle n \rangle$ and m_e^1 as explained in the text. (b) shows $m_p^1 = 1$ and the vertical dashed lines indicate the good limit cycle region as previously defined. $\Omega = \Gamma$ with the other parameters given in figure 5.1.

is a large separation between one of the eigenvalues and the rest. We can associate this eigenvalue with the phase diffusion rate. The other eigenvalues can be associated in some way with the energy relaxation eigenvalues in that they show crossings in the same places.

For decreasing ΔE, $\langle n \rangle$ increases and γ_ϕ is seen to decrease as for the $\Omega \gg \Gamma$ case. Unlike for $\Omega \gg \Gamma$ there is a large overlap between resonances so that it cannot be seen if γ_ϕ shows an increase for increasing $\langle n \rangle$ at any point. However, figures 3.17 and 3.18 provide some evidence for the behaviour. Along the one photon resonance F_n becomes sub-Poissonian and $F_I(0)$ shows a peak in same region in a similar manner to figures 6.8 and 6.12.

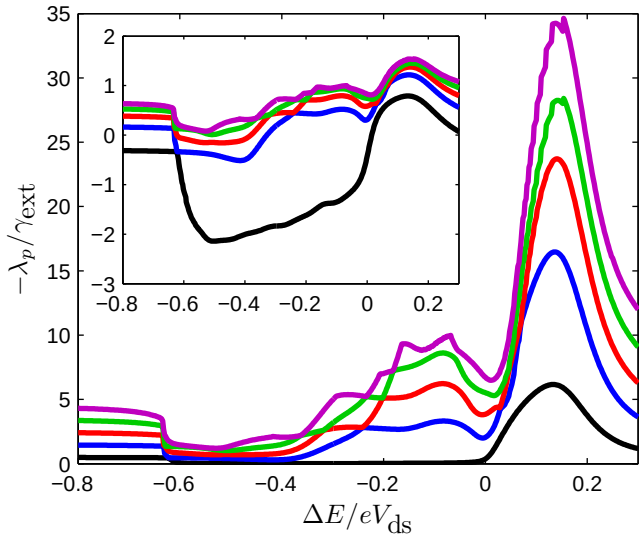

Figure 6.14. $-\Re\lambda_p$ for the 5 eigenvalues closest in magnitude to $-i\Omega$ as a function of the detuning for $\Omega = \Gamma$ with the other parameters given in figure 5.1. Inset shows the same as the main plot but on a $\log_{10}$ scale.

Chapter 7

Conclusion

The subject of this thesis has been the study of a particular open quantum system consisting of a resonator coupled to a SSET at the JQP resonance. The device has a large parameter regime, of which we have restricted ourselves to where the tunnelling of quasi-particles through the device is the dominant source of decoherence, which is a common experimental regime [20, 21]. In Chapter 2 we introduced the SSET before describing how coupling to both mechanical and superconducting stripline resonators could be achieved. We also introduced the Born-Markov master equation description of the system. Throughout this thesis we have made use of the Liouville space formalism in our description of the system. This allows the complex superoperators that appear in Hilbert space to be replaced with matrices, although of large size. By making use of Liouville space we could derive expressions in a straight forward manner for the current noise in the system.

The energy exchange between the SSET and resonator in the system leads to a variety of different steady-states for the resonator. In Chapter 3 we explored the behaviour of the system as the relative frequencies of the two sub-systems, coupling and detuning from the JQP resonance were varied. We found that the resonator could be driven into states of self-sustained oscillations reminiscent of a laser and made some comparisons with the micromaser system.

In the weak coupling regime the SSET acts on the resonator like a thermal bath. In Chapter 4 we explored this regime in detail. We found that the current through the SSET in this regime could be captured by a very simple model with the result that the change in the current due to the coupling was a smearing out of the JQP peak due to fluctuations in the position of the resonator and a shift in the detuning due to a shift in the average position of the resonator. For the current noise, in the thermal regime, this same smearing and shift in the detuning was found to only describe part of the change due to the coupling with the resonator. We found that a simple set of mean field equations was sufficient to fully describe the system in this regime. By

looking at the eigenvalues of the Liouvillian we found that there was an important contribution to the current noise due to the energy relaxation of the resonator. This was confirmed in a further simple model that also included the dynamics of the resonator. We also investigated the finite frequency current noise in this regime and could explain the shape of the peaks seen at multiples of the resonator frequency in terms of the eigenfunction expansion of the current noise. For either a large external temperature or large external damping of the resonator, the finite frequency current noise was captured by our second simple model.

In Chapter 5 we investigated more closely the transitions between dynamical states of the resonator. In some situations where the system was bistable, we could use a model for a generic bistable system to describe the SSET-resonator system. We then found that the slow switching rate between the two metastable states was present in the eigenvalues of the system. We studied the behaviour of the eigenvalues in other regimes and found that the main change in the current noise due to the interaction with the resonator could usually be captured by a single term in an eigenfunction expansion of the current noise. In the chapter we also gave the results of some quantum trajectory simulations on the device. It was found that based on a detection of the tunnelling of quasi-particles the switching of the resonator between the two states of a bistability could be observed.

A characteristic feature of a laser is a narrow linewidth when above threshold. In Chapter 6 we investigated the linewidth of the resonator coupled to the SSET. We showed how it is not necessary to calculate the full emission spectrum to extract the linewidth, but that it could be obtained from the eigenvalues of the Liouvillian. We gave the criteria for when this could be done and showed that within the limit cycle region the linewidth was determined by the phase diffusion rate of the resonator. We then investigated the change of the linewidth with varying coupling and detuning around the one photon resonance in the high frequency resonator regime. In doing so, we found an anomalous result (in comparison to a laser), in that the linewidth was no longer smallest on the resonance but showed minima when detuned slightly. This feature showed up clearly in the current noise. We also investigated the linewidth in the regime of similar frequencies for the SSET and resonator.

Further work based on this thesis is to obtain an explanation of the features seen in the phase diffusion rate in Chapter 6. Also by making use of a high performance computing facility further results could be obtained from the quantum trajectories method. On the experimental side it would be interesting for measurements to be made of the current noise through the SSET-resonator system so that comparisons could be made.

Appendix A

Details of the Numerical Method

This appendix gives some more details on the numerical method that was used to find selected eigenvalues and the associated eigenvectors of the Liouvillian. Also described are the approximations made in order to simplify the problem.

To describe the system numerically, the basis of the resonator must be truncated. External damping sets a limit on the resonator energy. We therefore use a Fock state basis for the oscillator truncated to N states, where N is chosen to be large enough that the probability for the resonator to have an energy larger than $\hbar\Omega N$ is negligible. In Liouville space the density matrix is a vector and $\mathcal{L}$ is a matrix with dimensions $9N^2 \times 9N^2$. The quantum optics toolbox [100] can be used to investigate open quantum systems. However, for our purposes it was necessary to develop our own code in order to carry out different analyses and make the necessary approximations that we describe below.

To obtain the steady state density matrix we need to find the right hand eigenvector corresponding to the zero eigenvalue, or null eigenvector, of the Liouvillian. We also make use of some of the non-zero eigenvalues along with their accompanying left and right eigenvectors in Chapters 4–6. The solution of the full eigenspectrum is unnecessary and difficult due to the large size of the Liouvillian matrix. We make use of the *eigs* function in Matlab [101] to solve the eigen problem. The Matlab function makes use of the ARPACK linear solver [102], which is operated in the shift-invert mode, and UMFPACK [103] to carry out the matrix inversion. The Matlab function finds the few nearest eigenvalues in magnitude to a given number with the associated eigenvectors. It is important that the number given is not the exact eigenvalue as the matrix to invert then becomes singular.

To find the steady-state and eigenvalues near zero the function is used to find the few eigenvalues closest to a small number which should ideally be closer to zero than the smallest non-zero eigenvalue, λ_1, in order to achieve rapid convergence. A good starting value is $-\gamma_{\rm ext}/20$, since for the uncoupled system $\lambda_1 = -\gamma_{\rm ext}$. If a parameter

is being varied then the value can be updated to $\lambda_1/20$ each iteration. For complex eigenvalues a search is made to find eigenvalues closest to $-if$, where f is the frequency required (e.g. the resonator frequency). Apart from the zero eigenvalue there are no eigenvalues with zero real part so singularities are not a problem. The right hand eigenvectors of the Liouvillian are also returned by the *eigs* function. To find the left hand eigenvectors the function must be called a second time with the transpose of the Liouvillian.

In order to use the largest possible value of N we need to reduce the size of the Liouvillian matrix for a given value of N. If certain elements of the density matrix are known to be zero in the steady state then they can be omitted from the calculation by removing the appropriate rows and columns of the Liouvillian. These terms must also be rapidly decaying for the current noise not to be affected by their omission.

In the electronic basis the density matrix elements corresponding to the q_1, q_2, $q_1^\dagger$ and $q_2^\dagger$ operators can be neglected. As discussed below equation 2.2.10, there is no coherence generated between the $|1\rangle$ state and the $|0\rangle$ or $|2\rangle$ states of the SSET, so these elements must decay to zero in the steady state. That these operators do not affect the dynamics can clearly be seen in the mean field equations for the SSET (equations 4.3.1–4.3.5), in which the neglected operators do not play a role. Since these elements of the density matrix are effectively decoupled from the rest of the system and do not interact with the resonator they can be neglected with no approximation. Neglecting these elements reduces the dimensions of the Liouvillian to $5N^2 \times 5N^2$.

In terms of the oscillator basis neglecting terms results in an approximate solution. For a damped harmonic oscillator the steady-state density matrix is diagonal in the Fock state basis for weak damping. Coherence between Fock states is only generated by the coupling to the SSET. Since the coupling is linear the coherence must decrease as the energy separation is increased (i.e. the further from the main diagonal the smaller the value). Note that this is only the case for linear coupling (e.g. in the quantum shuttle device the coupling can be exponential in position [104] and this approximation cannot be used). Based on this reasoning elements of the oscillator density matrix far from the diagonal can be neglected. To check the validity of the approximation the largest value on the last included diagonal of the resonator density matrix is found and treated as the error. The maximum error allowed depends on the quantity being calculated, we generally find that so long as it is below 10^{-11} the results are found to be indistinguishable from the exact solution.

After making these approximations the problem can be solved for $N \gtrsim 200$ using the above method on a desktop computer. The exact value of N that can be used depends on the number of diagonals required as it is the size of the final matrix that is important, the limiting factor being the memory required to perform the matrix inversion.

Appendix B

Quantum Trajectories

In this appendix we introduce the concept of quantum trajectories [32, 96, 105, 106] and make use of them to calculate the current noise at the right hand junction of the SSET. In the theory of quantum trajectories measurements on the system are represented as operators. These operators describe the change in the system that must have occurred in order for the detector to have measured something. For example the detector may be a photon detector and the change in the system might be a particular transition between energy levels. A successful detection causes a rapid change in our knowledge of the system. Less obvious is that the absence of a detection can also tell us something about the state of the system. The quantum trajectories method tells us the state of the system conditioned on a particular set of measurement results, known as the measurement record.

For the SSET-resonator system we assume that we have a detector that can tell us when a quasi-particle tunnels across the right hand junction. Experiments of this type have been carried out by coupling a quantum point contact to a quantum dot which allowed the current noise to be measured to high order [107–109].

To introduce the quantum trajectory model we follow the introduction of [105], but in the context of the SSET. The detection of a quasi-particle is associated with the tunnelling operator,

$$C = \sqrt{\Gamma}\,(q_1 + q_2)\,. \tag{B.0.1}$$

The operator corresponds to the change in the system that leads to the detection of a quasi-particle. The operator is analogous to the destruction operator of a harmonic oscillator in that it does not tell us which transition occurred. The change to the density matrix due to the detection is written in terms of the superoperator, $\mathcal{L}_J$,

$$\mathcal{L}_J \,|\rho(t)\rangle\rangle = C\rho(t)C^\dagger \tag{B.0.2}$$

As would be expected the trace over this gives the current at a particular time,

$$\langle\langle l_0 | \mathcal{L}_J | \rho(t) \rangle\rangle = \left\langle C^\dagger C \right\rangle_t = \frac{\langle I \rangle_t}{e} \tag{B.0.3}$$

The superoperator $\mathcal{L}_J$ forms the first part of the quasi-particle tunnelling superoperator, $\mathcal{L}_{\text{qp}}$, in the master equation as defined in equation 2.4.4. We can split the full Liouvillian as $\mathcal{L} = \mathcal{L}_0 + \mathcal{L}_J$, where $\mathcal{L}_0 = \mathcal{L} - \mathcal{L}_J$. By making use of the generalized Dyson expansion [110] the evolution of the density matrix can be written as,

$$\begin{aligned} |\rho(t)\rangle\rangle &= e^{(\mathcal{L}_0+\mathcal{L}_J)t} \, |\rho(0)\rangle\rangle \\ &= \sum_{m=0}^{\infty} \int_0^t dt_m \ldots \int_0^{t2} dt_1 \, e^{\mathcal{L}_0(t-t_m)} \mathcal{L}_J \ldots \mathcal{L}_J e^{\mathcal{L}_0(t_2-t_1)} \mathcal{L}_J e^{\mathcal{L}_0 t_1} \, |\rho(0)\rangle\rangle \, . \end{aligned} \tag{B.0.4}$$

The expansion is valid for any choice of operators and would appear to make a relatively simple equation quite complicated. However, for the particular definition of $\mathcal{L}_J$ it has an important physical meaning. m gives the number of occurrences of $\mathcal{L}_J$ and the evolution operator $e^{\mathcal{L}_0 t}$ is the evolution of the density matrix when no quasi-particles are detected. The part under the integrals can therefore be interpreted as the un-normalized density matrix conditioned on a particular measurement record, $\mathcal{M}$. $\mathcal{M}$ consists of the detection of m quasi-particles in the non-overlapping time intervals, $[t_1, t_1 + dt_1), \ldots, [t_m, t_m + dt_m)$. We denote this density matrix $\tilde{\rho}_c^{\mathcal{M}}(t)$, which is defined,

$$\left|\tilde{\rho}_c^{\mathcal{M}}(t)\right\rangle\rangle = e^{\mathcal{L}_0(t-t_m)} \mathcal{L}_J \ldots \mathcal{L}_J e^{\mathcal{L}_0(t_2-t_1)} \mathcal{L}_J e^{\mathcal{L}_0 t_1} \, |\rho(0)\rangle\rangle \, , \tag{B.0.5}$$

The probability, $P(\mathcal{M})$, to obtain the measurement record $\mathcal{M}$ is [110],

$$P(\mathcal{M}) = \langle\langle l_0 | \tilde{\rho}_c^{\mathcal{M}}(t) \rangle\rangle, \tag{B.0.6}$$

which is just the normalization of $\tilde{\rho}_c^{\mathcal{M}}(t)$. We define the normalized conditioned density matrix as,

$$\left|\rho_c^{\mathcal{M}}(t)\right\rangle\rangle = \frac{\left|\tilde{\rho}_c^{\mathcal{M}}(t)\right\rangle\rangle}{\langle\langle l_0 | \tilde{\rho}_c^{\mathcal{M}}(t) \rangle\rangle} \tag{B.0.7}$$

using this definition, equation B.0.4 can be written in the form,

$$|\rho(t)\rangle\rangle = \sum_{m=0}^{\infty} \int_0^t dt_m \ldots \int_0^{t2} dt_1 \, P(\mathcal{M}) \, \left|\rho_c^{\mathcal{M}}(t)\right\rangle\rangle \, . \tag{B.0.8}$$

Written in this form $\rho_c^{\mathcal{M}}(t)$ can be interpreted as the actual state of the system given the measurement record $\mathcal{M}$. The unconditioned density matrix is then obtained by the

ensemble average of all the conditional density matrices weighted by the probability for each one to occur.

In practice we could set up an experiment a sufficiently long time ($t = -\infty$) before we switch on the detector at $t = 0$ then the initial density matrix will be the steady-state one. We would then aim to measure the times at which individual quasi-particles tunnel, which would form our measurement record and we can use the above to obtain the conditioned density matrix of the system.

We can perform a simulation of an experiment by making use of random numbers. From now on we will drop the superscript $\mathcal{M}$ and take $\rho_c(t)$ to be the density matrix conditioned on the previous measurement results. The probability for a quasi-particle to tunnel across the right hand junction between a time t and $t + dt$, will be given by,

$$P_J(t) = \langle\langle l_0 | \mathcal{L}_J | \rho_c(t) \rangle\rangle \, dt. \tag{B.0.9}$$

dt is chosen to be sufficiently small that the probability for two quasi-particles to tunnel across the junction in a single step is negligible. For each time step a random number R, between 0 and 1, is chosen. If the number is less than $P_J(t)$ then a quasi-particle is detected and the system is changed using $\mathcal{L}_J$, otherwise it evolves with $\mathcal{L}_0$,

$$|\rho_c(t+dt)\rangle\rangle = \begin{cases} \frac{\mathcal{L}_J|\rho_c(t)\rangle\rangle}{P_J(t)} & P_J < R \\ \frac{e^{\mathcal{L}_0 dt}|\rho_c(t)\rangle\rangle}{1-P_J(t)} & P_J > R \end{cases} \tag{B.0.10}$$

By following this procedure we can find a conditioned density matrix, where the measurement record has the correct statistics. The time evolution, by the operator $e^{\mathcal{L}_0 dt}$, is carried out using a 4-5 embedded Runge-Kutta method with adaptive step size control [111].

We can use the quantum trajectories method to find the correlation function required for the calculation of the current noise at the right hand junction, based on the theory presented in this appendix. An alternative derivation also using quantum trajectories can be found in [106] or using an electron counting variable in [63], which have the same solution. We require,

$$\lim_{t\to\infty} \langle \{ I_R(t+\tau), I_R(t) \} \rangle = \lim_{t\to\infty} 2e^2 \langle \mathcal{L}_J(t+\tau)\mathcal{L}_J(t) \rangle \, . \tag{B.0.11}$$

The ordering of the operators does not matter here so we can remove the anti-commutator. The correlation function is the ensemble average over all trajectories starting from the steady-state density matrix, in which a quasi-particle is detected at the times 0 and τ. The correlation function will be given by a trace over equation B.0.4 with $|\rho(0)\rangle\rangle = |r_0\rangle\rangle$ and both $t_1 = 0$ and $t_n = \tau$. Clearly there must be at least one quasi-particle detected in the time period so we can also neglect the $m = 0$ term. The

correlation function is,

$$\begin{aligned}
&\lim_{t\to\infty} 2e^2 \left\langle \mathcal{L}_J(t+\tau)\mathcal{L}_J(t)\right\rangle \\
&\quad = 2\sum_{m=1}^{\infty}\int_0^{\tau} dt_m \ldots \int_0^{t2} dt_1 \ \langle\langle l_0| e^{\mathcal{L}_0(\tau-t_m)}\mathcal{L}_J \ldots \mathcal{L}_J e^{\mathcal{L}_0 t_1}|r_0\rangle\rangle\, \delta(t_1)\delta(\tau-t_1) \\
&\quad = 2e^2\int_0^{\tau} dt_1 \, \langle\langle l_0| e^{\mathcal{L}_0(\tau-t_1)}\mathcal{L}_J e^{\mathcal{L}_0 t_1}|r_0\rangle\rangle\, \delta(t_1)\delta(\tau-t_1) \\
&\qquad + 2e^2\sum_{m=2}^{\infty}\int_0^{\tau} dt_{m-1} \ldots \int_0^{t2} dt_2 \ \langle\langle l_0|\mathcal{L}_J e^{\mathcal{L}_0(\tau-t_{m-1})}\mathcal{L}_J \ldots \mathcal{L}_J e^{\mathcal{L}_0 t_2}\mathcal{L}_J|r_0\rangle\rangle \\
&\quad = 2e^2\delta(\tau)\,\langle\langle l_0|\mathcal{L}_J|r_0\rangle\rangle + 2e^2\,\langle\langle l_0|\mathcal{L}_J e^{\mathcal{L}\tau}\mathcal{L}_J|r_0\rangle\rangle
\end{aligned} \tag{B.0.12}$$

where we have separated out the $m = 1$ contribution and used the expansion from equation B.0.4 in reverse to get the final line.

Appendix C

Mean Field Equations

The mean field equations up to first order in the system operators were calculated in [22]. The equations for the SSET operators alone were given in equations 4.3.1–4.3.5 and the equations for the resonator operators alone were given in equations 4.3.6–4.3.10. Below are written the remaining equations to complete the set up to second order in the operators.

$$\dot{\langle xp_0\rangle}_t = i\frac{E_J}{2\hbar}\left(\langle xc\rangle_t - \left\langle xc^\dagger\right\rangle_t\right) + \Gamma\langle xp_1\rangle_t + \langle vp_0\rangle_t \tag{C.0.1}$$

$$\dot{\langle xp_1\rangle}_t = -\Gamma\langle xp_1\rangle_t + \Gamma\langle xp_2\rangle_t + \langle vp_1\rangle_t \tag{C.0.2}$$

$$\dot{\langle xp_2\rangle}_t = -i\frac{E_J}{2\hbar}\left(\langle xc\rangle_t - \left\langle xc^\dagger\right\rangle_t\right) - \Gamma\langle xp_2\rangle_t + \langle vp_2\rangle_t \tag{C.0.3}$$

$$\begin{aligned}\dot{\langle xc\rangle}_t = &\left(-i\frac{\Delta E}{\hbar} - \frac{\Gamma}{2}\right)\langle xc\rangle_t + i\frac{E_J}{2\hbar}\left(\langle xp_0\rangle_t - \langle xp_2\rangle_t\right) + \langle vc\rangle_t \\ &- i\frac{2m\Omega^2 x_s}{\hbar}\left\langle x^2c\right\rangle_t\end{aligned} \tag{C.0.4}$$

$$\begin{aligned}\dot{\left\langle xc^\dagger\right\rangle}_t = &\left(i\frac{\Delta E}{\hbar} - \frac{\Gamma}{2}\right)\left\langle xc^\dagger\right\rangle_t - i\frac{E_J}{2\hbar}\left(\langle xp_0\rangle_t - \langle xp_2\rangle_t\right) + \left\langle vc^\dagger\right\rangle_t \\ &+ i\frac{2m\Omega^2 x_s}{\hbar}\left\langle x^2c^\dagger\right\rangle_t\end{aligned} \tag{C.0.5}$$

$$\dot{\langle vp_0\rangle}_t = i\frac{E_J}{2\hbar}\left(\langle vc\rangle_t - \left\langle vc^\dagger\right\rangle_t\right) + \Gamma\langle vp_1\rangle_t - \Omega^2\langle xp_0\rangle_t - \gamma_{ext}\langle vp_0\rangle_t \tag{C.0.6}$$

$$\dot{\langle vp_1\rangle}_t = -\left(\Gamma + \gamma_{ext}\right)\langle vp_1\rangle_t + \Gamma\langle vp_2\rangle_t - \Omega^2\langle xp_1\rangle_t - x_s\Omega^2\langle p_1\rangle_t \tag{C.0.7}$$

$$\dot{\langle vp_2\rangle}_t = -i\frac{E_J}{2\hbar}\left(\langle vc\rangle_t - \left\langle vc^\dagger\right\rangle_t\right) - \left(\Gamma + \gamma_{ext}\right)\langle vp_2\rangle_t - \Omega^2\langle xp_2\rangle_t - 2x_s\Omega^2\langle p_2\rangle_t \tag{C.0.8}$$

$$\begin{aligned}\dot{\langle vc\rangle}_t = &\left(-i\frac{\Delta E}{\hbar} - \frac{\Gamma}{2} - \gamma_{ext}\right)\langle vc\rangle_t - \Omega^2\langle xc\rangle_t + i\frac{E_J}{2\hbar}\left(\langle vp_0\rangle_t - \langle vp_2\rangle_t\right) \\ &- \frac{i2m\Omega^2 x_s}{\hbar}\langle vxc\rangle_t\end{aligned} \tag{C.0.9}$$

$$\langle \dot{vc^\dagger} \rangle = \left(i\frac{\Delta E}{\hbar} - \frac{\Gamma}{2} - \gamma_{ext} \right) \left\langle vc^\dagger \right\rangle_t - \Omega^2 \left\langle xc^\dagger \right\rangle_t - i\frac{E_J}{2\hbar} \left(\langle vp_0 \rangle_t - \langle vp_2 \rangle_t \right) + \frac{i2m\Omega^2 x_s}{\hbar} \left\langle xvc^\dagger \right\rangle_t , \tag{C.0.10}$$

where here the averages imply a trace over the SSET and resonator weighted by the density operator, $\langle O \rangle_t = \mathrm{Tr}\left[O\rho(t)\right]$.

C.1 Forming a closed set of equations

As discussed in Section 4.3 the mean field equations never form a closed set. In order to obtain a closed set of equations at second order we need to eliminate the third order terms (e.g. $\left\langle x^2 c^\dagger \right\rangle_t , \langle vxc \rangle_t$) appearing in equations C.0.4, C.0.5, C.0.9 and C.0.10. This is done by setting the third order cumulant [112] to zero, which means to products of three operators a, b and c we apply the approximation,

$$\langle abc \rangle = \langle a \rangle\langle bc \rangle + \langle b \rangle\langle ac \rangle + \langle c \rangle\langle ab \rangle - 2 \langle a \rangle\langle b \rangle\langle c \rangle , \tag{C.1.1}$$

provided a, b and c all commute. Where the operators involved do not commute the expectation value should be symmetrized appropriately in order for the commutation relations to be preserved. Consider, for simplicity, the example of the expectation value $\langle xv \rangle$ and assuming the second order cumulant is zero. This would result in $\langle xv \rangle \rightarrow \langle x \rangle\langle v \rangle$, but also $\langle vx \rangle \rightarrow \langle x \rangle\langle v \rangle$. This is not consistent with the commutation relations since we could also write $\langle xv \rangle = \langle vx \rangle + i\hbar/m \rightarrow \langle x \rangle\langle v \rangle + i\hbar/m$. The approximation should only be applied to a symmetrized combination of the operators, $\frac{1}{2}(\langle xv \rangle + \langle vx \rangle)$, which ensures that the approximation is consistent with the commutation relations.

Applying the approximation to the term $\left\langle x^2 c \right\rangle_t$, in equation C.0.4, we make the replacement,

$$\left\langle x^2 c \right\rangle_t \rightarrow 2\langle x \rangle_t \langle xc \rangle_t + \left(\left\langle x^2 \right\rangle_t - 2 \langle x \rangle_t^2 \right) \langle c \rangle_t \tag{C.1.2}$$

and similarly for $\left\langle x^2 c^\dagger \right\rangle_t$ in equation C.0.5. The resulting approximate equations are,

$$\langle \dot{xc} \rangle_t = \left(-i\frac{\Delta E + 4m\Omega^2 x_s \langle x \rangle_t}{\hbar} - \frac{\Gamma}{2} \right) \langle xc \rangle_t + i\frac{E_J}{2\hbar} (\langle xp_0 \rangle_t - \langle xp_2 \rangle_t) + \langle vc \rangle_t - i\frac{2m\Omega^2 x_s}{\hbar} \left(\left\langle x^2 \right\rangle_t - 2 \langle x \rangle_t^2 \right) \langle c \rangle_t \tag{C.1.3}$$

$$\langle \dot{xc^\dagger} \rangle_t = \left(i\frac{\Delta E + 4m\Omega^2 x_s \langle x \rangle_t}{\hbar} - \frac{\Gamma}{2} \right) \left\langle xc^\dagger \right\rangle_t - i\frac{E_J}{2\hbar} (\langle xp_0 \rangle_t - \langle xp_2 \rangle_t) + \left\langle vc^\dagger \right\rangle_t + i\frac{2m\Omega^2 x_s}{\hbar} \left(\left\langle x^2 \right\rangle_t - 2 \langle x \rangle_t^2 \right) \left\langle c^\dagger \right\rangle_t . \tag{C.1.4}$$

The other third order terms we need to consider are $\langle vxc \rangle_t$ and $\left\langle xvc^\dagger \right\rangle_t$, which arise in equations C.0.9 and C.0.10 respectively. Since x and v do not commute we must

first rewrite the expectation values in the following way before expansion so that the commutation relations are obeyed.

$$\langle vxc\rangle_t = \frac{1}{2}\langle (vx+xv)\,c\rangle_t - i\frac{\hbar}{2m}\langle c\rangle_t\,. \tag{C.1.5}$$

Performing the expansion as before we can make the replacement,

$$\frac{1}{2}\langle (vx+xv)\,c\rangle_t \to \langle x\rangle_t\langle vc\rangle_t + \langle v\rangle_t\langle xc\rangle_t + \frac{1}{2}\langle c\rangle\langle xv+vx\rangle_t - 2\langle x\rangle_t\langle v\rangle_t\langle c\rangle_t\,. \tag{C.1.6}$$

The same procedure can be followed for the $\langle xvc^\dagger\rangle_t$ term to give

$$\begin{aligned}
\dot{\langle vc\rangle}_t = &\left(-i\frac{\Delta E + 2m\Omega^2 x_s\langle x\rangle_t}{\hbar} - \frac{\Gamma}{2} - \gamma_{ext}\right)\langle vc\rangle_t + i\frac{E_J}{2\hbar}(\langle vp_0\rangle_t - \langle vp_2\rangle_t)\\
&- \Omega^2\left(1 + i\frac{2mx_s}{\hbar}\langle v\rangle_t\right)\langle xc\rangle_t\\
&- x_s\Omega^2\left(1 + i\frac{m}{\hbar}\left(\langle xv\rangle_t + \langle vx\rangle_t - 4\langle x\rangle_t\langle v\rangle_t\right)\right)\langle c\rangle_t
\end{aligned} \tag{C.1.7}$$

$$\begin{aligned}
\dot{\langle vc^\dagger\rangle}_t = &\left(i\frac{\Delta E + 2m\Omega^2 x_s\langle x\rangle_t}{\hbar} - \frac{\Gamma}{2} - \gamma_{ext}\right)\langle vc^\dagger\rangle_t - i\frac{E_J}{2\hbar}(\langle vp_0\rangle_t - \langle vp_2\rangle_t)\\
&- \Omega^2\left(1 - i\frac{2mx_s}{\hbar}\langle v\rangle_t\right)\langle xc^\dagger\rangle_t\\
&- x_s\Omega^2\left(1 - i\frac{m}{\hbar}\left(\langle xv\rangle_t + \langle vx\rangle_t - 4\langle x\rangle_t\langle v\rangle_t\right)\right)\langle c^\dagger\rangle_t\,,
\end{aligned} \tag{C.1.8}$$

which completes the closure of the second order equations. This method is readily extended to obtain the third order mean field equations by instead setting the fourth order cumulant to zero and following the same procedure. For the fourth order cumulant the replacement for the operators a, b, c and d is,

$$\begin{aligned}
\langle abcd\rangle \to &\Big[\langle a\rangle\langle bcd\rangle + \langle b\rangle\langle acd\rangle + \langle c\rangle\langle abd\rangle + \langle d\rangle\langle abc\rangle + \langle ab\rangle\langle cd\rangle + \langle ac\rangle\langle bd\rangle\\
&+ \langle ad\rangle\langle bc\rangle\Big] - 2\Big[\langle a\rangle\langle b\rangle\langle cd\rangle + \langle a\rangle\langle c\rangle\langle bd\rangle + \langle a\rangle\langle d\rangle\langle bc\rangle + \langle b\rangle\langle c\rangle\langle ad\rangle\\
&+ \langle b\rangle\langle d\rangle\langle ac\rangle + \langle c\rangle\langle d\rangle\langle ab\rangle\Big] + 6\langle a\rangle\langle b\rangle\langle c\rangle\langle d\rangle
\end{aligned} \tag{C.1.9}$$

C.2 Current noise

We describe in this section the calculation of the current noise spectrum by use of the mean field equations. We do this for the SSET operators only in order to simplify the notation, but the extension to include the resonator is straightforward. We again make use of the quantum regression theorem (QRT) [32, 48], but in a different form to that given in Section 2.6. If the system can be described by a set of equations for the average

values of the form [48],

$$\left\langle \dot{Y}_i \right\rangle_t = \sum_j A_{ij} \left\langle Y_i \right\rangle_t , \tag{C.2.1}$$

then the equation of motion for the two time correlation functions obeys the same equation,

$$\frac{\partial}{\partial \tau} \left\langle \{\bar{Y}_i(t+\tau), \bar{Y}_l(t)\} \right\rangle = \sum_j A_{ij} \left\langle \{\bar{Y}_j(t+\tau), \bar{Y}_l(t)\} \right\rangle . \tag{C.2.2}$$

The evolution of the system is written in terms of the vector of expectation values, $\boldsymbol{p}(t)$, and the matrix, A,

$$\dot{\boldsymbol{p}}(t) = A\boldsymbol{p}(t), \qquad \boldsymbol{p}(t) = \begin{pmatrix} \langle p_0 \rangle_t \\ \langle p_1 \rangle_t \\ \langle p_2 \rangle_t \\ \langle c \rangle_t \\ \langle c^\dagger \rangle_t \end{pmatrix}, \tag{C.2.3}$$

which is of the form of equation C.2.1. As an example we calculate the charge noise spectrum. We define the vector of correlation functions with the charge operator, $\boldsymbol{p}_Q(t+\tau, t)$, which by the QRT obeys the same equation as $\boldsymbol{p}(t)$,

$$\frac{\partial}{\partial \tau} \boldsymbol{p}_Q(t+\tau, t) = A\boldsymbol{p}_Q(t+\tau, t), \qquad \boldsymbol{p}_Q(t+\tau, t) = \begin{pmatrix} \left\langle \{\bar{p}_0(t+\tau), \bar{Q}(t)\} \right\rangle \\ \left\langle \{\bar{p}_1(t+\tau), \bar{Q}(t)\} \right\rangle \\ \left\langle \{\bar{p}_2(t+\tau), \bar{Q}(t)\} \right\rangle \\ \left\langle \{\bar{c}(t+\tau), \bar{Q}(t)\} \right\rangle \\ \left\langle \{\bar{c^\dagger}(t+\tau), \bar{Q}(t)\} \right\rangle \end{pmatrix}. \tag{C.2.4}$$

The Laplace transform is defined [69],

$$\hat{f}(z) = \int_0^\infty d\tau \, e^{z\tau} f(\tau) \tag{C.2.5}$$

Taking the Laplace transform of equation C.2.4 with $z = -i\omega$ and the $t \to \infty$ limit will give,

$$-i\omega \hat{\boldsymbol{p}}_Q(-i\omega) - \boldsymbol{p}_Q(\infty, \infty) = A\hat{\boldsymbol{p}}_Q(-i\omega) \tag{C.2.6}$$

$$\Rightarrow \hat{\boldsymbol{p}}_Q(-i\omega) = (-A - i\omega)^{-1} \boldsymbol{p}_Q(\infty, \infty) \tag{C.2.7}$$

where $\hat{\boldsymbol{p}}_Q(-i\omega)$ is a vector of noise spectra and $\boldsymbol{p}_Q(\infty,\infty)$ is a vector of expectation values in the steady-state. They are given by,

$$\hat{\boldsymbol{p}}_Q(-i\omega) = \begin{pmatrix} S^+_{p_0,Q}(\omega) \\ S^+_{p_1,Q}(\omega) \\ S^+_{p_2,Q}(\omega) \\ S^+_{c,Q}(\omega) \\ S^+_{c^\dagger,Q}(\omega) \end{pmatrix}, \qquad \boldsymbol{p}_Q(\infty,\infty) = \begin{pmatrix} \langle\{\bar{p}_0,\bar{Q}\}\rangle \\ \langle\{\bar{p}_1,\bar{Q}\}\rangle \\ \langle\{\bar{p}_2,\bar{Q}\}\rangle \\ \langle\{\bar{c},\bar{Q}\}\rangle \\ \langle\{\bar{c^\dagger},\bar{Q}\}\rangle \end{pmatrix}. \tag{C.2.8}$$

We can calculate $S_{Q,Q}(\omega)$ from,

$$\begin{aligned} S_{Q,Q}(\omega) &= S_{p_1,Q}(\omega) + 2S_{p_2,Q}(\omega) \\ &= 2\Re\left[S^+_{p_1,Q}(\omega) + 2S^+_{p_2,Q}(\omega)\right]. \end{aligned} \tag{C.2.9}$$

The charge noise spectrum is found from the addition of the relevant elements of $\hat{\boldsymbol{p}}_Q(-i\omega)$. However, we can go further and express $S_{Q,Q}(\omega)$ in a form very similar to that for the full system given in equation 2.7.4. We first define a matrix Q^m that when acting on $\boldsymbol{p}(\infty)$ gives $\boldsymbol{p}_Q(\infty,\infty)$,

$$\boldsymbol{p}_Q(\infty,\infty) = 2\left(Q^m - \langle Q\rangle\right)\boldsymbol{p}(\infty), \tag{C.2.10}$$

The form of Q^m can be found by calculating the commutators of Q with each of the operators that make up $\boldsymbol{p}(t)$ as required for the elements of $\boldsymbol{p}_Q(\infty,\infty)$,

$$\begin{aligned} &\frac{1}{2}\{Q,p_0\} = 0, && \frac{1}{2}\{Q,p_1\} = p_1, && \frac{1}{2}\{Q,p_2\} = 2p_2, \\ &\frac{1}{2}\{Q,c\} = c, && \frac{1}{2}\{Q,c^\dagger\} = c^\dagger, \end{aligned} \tag{C.2.11}$$

where we have included a factor of $\frac{1}{2}$ to make the operator analogous to the charge superoperator, $\mathcal{Q}$, that acts on the full system (equation 2.7.3). This shows that Q^m is a diagonal matrix of the form,

$$Q^m = \text{diag}\,[0,1,2,1,1] \tag{C.2.12}$$

We also define a vector corresponding to the trace operator $\boldsymbol{t} = [1,1,1,0,0]^T$, where T is the transpose. This is clearly the correct trace since $\boldsymbol{t}^T\boldsymbol{p}(t) = \langle p_0\rangle_t + \langle p_1\rangle_t + \langle p_2\rangle_t = \text{Tr}\,[\rho(t)]$. From the definition of Q^m we will have,

$$\langle Q\rangle = \boldsymbol{t}^T Q^m \boldsymbol{p}(\infty) \tag{C.2.13}$$

Using these definitions the charge noise spectrum is given by,

$$S^m_{Q,Q}(\omega) = 4\Re\left[\boldsymbol{t}^T Q^m \left(-i\omega - A\right)^{-1}\left(Q^m - \langle Q\rangle\right)\boldsymbol{p}(\infty)\right] \tag{C.2.14}$$

A has a set of right eigenvectors, $\boldsymbol{r_p}$, and left eigenvectors, $\boldsymbol{l_p}$,

$$A\boldsymbol{r_p} = \lambda_p^m \boldsymbol{r_p} \tag{C.2.15}$$
$$\boldsymbol{l_p}^T A = \lambda_p^m \boldsymbol{l_p}^T \tag{C.2.16}$$

where λ_p^m are the associated eigenvalues. Just like for the Liouvillian A must have an eigenvalue, $\lambda_0^m = 0$, with corresponding right and left eigenvectors, $\boldsymbol{r_0} = \boldsymbol{p}(\infty)$ and $\boldsymbol{l_0} = \boldsymbol{t}$. By performing this eigenvector expansion on A in equation C.2.14 we obtain the result,

$$S^m_{Q,Q}(\omega) = 4\Re\left[\sum_{p=1}^{5}\frac{\boldsymbol{l_0}^T Q^m \boldsymbol{r_p}\boldsymbol{l_p}^T Q^m \boldsymbol{r_0}}{-i\omega - \lambda_p^m}\right] \tag{C.2.17}$$

which is analogous to equation 2.7.4 for the full system.

We can easily follow the same procedure to find the current noise at the left hand junction. The current operator was $I_L = i\frac{eE_J}{\hbar}\left(c^\dagger - c\right)$ (equation 2.7.5). Calculating the commutators as before,

$$\begin{aligned}
&\frac{1}{2}\{I_L, p_0\} = i\frac{eE_J}{2\hbar}\left(c^\dagger - c\right), && \frac{1}{2}\{I_L, p_1\} = 0,\\
&\frac{1}{2}\{I_L, p_2\} = i\frac{eE_J}{2\hbar}\left(c^\dagger - c\right), && \frac{1}{2}\{I_L, c\} = i\frac{eE_J}{2\hbar}\left(p_0 + p_2\right),\\
&\frac{1}{2}\{I_L, c^\dagger\} = -i\frac{eE_J}{2\hbar}\left(p_0 + p_2\right).
\end{aligned} \tag{C.2.18}$$

I_L^m therefore takes the form,

$$I_L^m = i\frac{eE_J}{2\hbar}\begin{pmatrix} 0 & 0 & 0 & -1 & 1\\ 0 & 0 & 0 & 0 & 0\\ 0 & 0 & 0 & -1 & 1\\ 1 & 0 & 1 & 0 & 0\\ -1 & 0 & -1 & 0 & 0\end{pmatrix}. \tag{C.2.19}$$

The spectrum is given by,

$$S^m_{I_L,I_L}(\omega) = 4\Re\left[\sum_{p=1}^{5}\frac{\boldsymbol{l_0}^T I_L^m \boldsymbol{r_p}\boldsymbol{l_p}^T I_L^m \boldsymbol{r_0}}{-i\omega - \lambda_p^m}\right]. \tag{C.2.20}$$

For the current noise at the right hand junction the quantum regression theorem cannot be used directly. In [24] we used an electron counting variable approach [36, 61, 85] to calculate the current noise at the right hand junction. The final result can be

written in a similar form to the equations for the charge noise and left hand junction noise, derived in this section,

$$S^m_{I_R,I_R}(\omega) = 2e\boldsymbol{l_0}^T I^m_R \boldsymbol{r_0} + 4\Re\left[\sum_{p=1}^{5} \frac{\boldsymbol{l_0}^T I^m_R \boldsymbol{r_p} \boldsymbol{l_p}^T I^m_R \boldsymbol{r_0}}{-i\omega - \lambda^m_p}\right], \tag{C.2.21}$$

where I^m_R is defined,

$$I^m_R = \begin{pmatrix} 0 & \Gamma & 0 & 0 & 0 \\ 0 & 0 & \Gamma & 0 & 0 \\ 0 & 0 & 0 & 0 & 0 \\ 0 & 0 & 0 & 0 & 0 \\ 0 & 0 & 0 & 0 & 0 \end{pmatrix}. \tag{C.2.22}$$

to include the resonator is a straightforward extension. The charge and current operators commute with the resonator operators, so the commutation relations are simple to calculate. The trace operator (or $\boldsymbol{l_0}$) will still have just the three non-zero elements in the positions of $\langle p_0 \rangle_t$, $\langle p_1 \rangle_t$ and $\langle p_2 \rangle_t$. Finally the sums in equations C.2.17, C.2.21 and C.2.21 should be extended to all eigenvalues of A, except for the zero one.

Appendix D

Calculation of $S_{x,x}(\omega)$ and $S_{x^2,x^2}(\omega)$

In this appendix we calculate $S_{x,x}(\omega)$ and $S_{x^2,x^2}(\omega)$ for an oscillator in a thermal state. For the calculation of $S_{x,x}(\omega)$ we begin from the mean field equations for $\langle \bar{x} \rangle_t$ and $\langle \bar{v} \rangle_t$. As before we use the notation $\bar{a}(t) = a(t) - \langle a \rangle$, where $\langle a \rangle \equiv \langle a \rangle_\infty$,

$$\begin{aligned} \langle \dot{\bar{x}} \rangle_t &= \langle \bar{v} \rangle_t \,, \\ \langle \dot{\bar{v}} \rangle_t &= -\Omega^2 \langle \bar{x} \rangle_t - \gamma \langle \bar{v} \rangle_t \,. \end{aligned} \tag{D.0.1}$$

By use of the quantum regression theorem (equation C.2.2) we can write down the evolution of the correlation functions,

$$\begin{aligned} \frac{\partial}{\partial \tau} \langle \{ \bar{x}(t+\tau), \bar{x}(t) \} \rangle &= \langle \{ \bar{v}(t+\tau), \bar{x}(t) \} \rangle \,, \\ \frac{\partial}{\partial \tau} \langle \{ \bar{v}(t+\tau), \bar{x}(t) \} \rangle &= -\Omega^2 \langle \{ \bar{x}(t+\tau), \bar{x}(t) \} \rangle - \gamma \langle \{ \bar{v}(t+\tau), \bar{x}(t) \} \rangle \,. \end{aligned} \tag{D.0.2}$$

We then perform a Laplace transform as defined in equation C.2.5 with $z = -i\omega$ to obtain equations for the $S^+_{a,b}(\omega)$ part of the noise defined in equation 2.6.3, with the result,

$$\begin{aligned} -i\omega S^+_{x,x}(\omega) - 2 \langle \bar{x}^2 \rangle &= S^+_{v,x}(\omega), \\ -i\omega S^+_{v,x}(\omega) - \langle \{ \bar{v}, \bar{x} \} \rangle &= -\Omega^2 S^+_{x,x}(\omega) - \gamma S^+_{v,x}(\omega), \end{aligned} \tag{D.0.3}$$

For a thermal state $\langle\{v, x\}\rangle = 0$. Solving the two equations we obtain the result,

$$\begin{aligned} S_{x,x}(\omega) &= 2\Re\left[S^{+}_{x,x}(\omega)\right] \\ &= 2\Re\left[\frac{2\left(\gamma - i\omega\right)\left\langle \bar{x}^2\right\rangle}{\Omega^2 - \omega^2 - i\omega\gamma}\right] \\ &= \frac{4\gamma\Omega^2\left\langle \bar{x}^2\right\rangle}{\left(\Omega^2 - \omega^2\right)^2 + \omega^2\gamma^2}. \end{aligned} \tag{D.0.4}$$

For the $S_{x^2,x^2}(\omega)$ spectrum we begin from the equations for the second order mean field equations again about the steady-state,

$$\begin{aligned} \left\langle \dot{\bar{x^2}}\right\rangle_t &= \langle\overline{xv_+}\rangle_t\,, \\ \left\langle \dot{\bar{v^2}}\right\rangle_t &= -\Omega^2\langle\overline{xv_+}\rangle_t - 2\gamma\left\langle \bar{v^2}\right\rangle_t\,, \\ \langle\dot{\overline{xv_+}}\rangle_t &= 2\left\langle \bar{v^2}\right\rangle_t - 2\Omega^2\left\langle \bar{x^2}\right\rangle_t - \gamma\langle\overline{xv_+}\rangle_t\,, \end{aligned} \tag{D.0.5}$$

where $xv_+ \equiv xv + vx$. Making the transformation as before we obtain,

$$\begin{aligned} -i\omega S^{+}_{x^2,x^2}(\omega) - \left\langle\{\bar{x^2}, \bar{x^2}\}\right\rangle &= S^{+}_{xv_+,x^2}(\omega), \\ -i\omega S^{+}_{v^2,x^2}(\omega) - \left\langle\{\bar{v^2}, \bar{x^2}\}\right\rangle &= -\Omega^2 S^{+}_{xv_+,x^2}(\omega) - 2\gamma S^{+}_{v^2,x^2}(\omega), \\ -i\omega S^{+}_{xv_+,x^2}(\omega) - \left\langle\{\overline{xv_+}, \bar{x^2}\}\right\rangle &= 2S^{+}_{v^2,x^2}(\omega) - 2\Omega^2 S^{+}_{x^2,x^2}(\omega) - \gamma S^{+}_{xv_+,x^2}(\omega). \end{aligned} \tag{D.0.6}$$

Since we have a Gaussian state we can use the method described in Section C.1 to reduce the expectation values to ones of second order. In doing this we find,

$$\begin{aligned} \left\langle\{\bar{x^2}, \bar{x^2}\}\right\rangle &= 2\left[\left\langle x^2\right\rangle^2 - \langle x\rangle^4\right], \\ \left\langle\{\bar{v^2}, \bar{x^2}\}\right\rangle &= 0, \\ \left\langle\{\overline{xv_+}, \bar{x^2}\}\right\rangle &= 0. \end{aligned} \tag{D.0.7}$$

First eliminating $S^{+}_{xv_+,x^2}(\omega)$ from equations D.0.6 we obtain,

$$\begin{aligned} \left[2\gamma - i\omega\right] S^{+}_{v^2,x^2}(\omega) &= i\omega\Omega^2 S^{+}_{x^2,x^2}(\omega) + 2\Omega^2\left[\left\langle x^2\right\rangle^2 - \langle x\rangle^4\right], \\ \left[2\Omega^2 - \omega^2 - i\omega\gamma\right] S^{+}_{x^2,x^2}(\omega) &= 2S^{+}_{v^2,x^2}(\omega) + 2\left(\gamma - i\omega\right)\left[\left\langle x^2\right\rangle^2 - \langle x\rangle^4\right]. \end{aligned} \tag{D.0.8}$$

The final solution is then,

$$
\begin{aligned}
S_{x^2,x^2}(\omega) &= 2\Re\left[\frac{\left(4\Omega^2+4\gamma^2-2\omega^2-6i\omega\gamma\right)\left[\left\langle x^2\right\rangle^2-\left\langle x\right\rangle^4\right]}{\gamma\left(4\Omega^2-3\omega^2\right)-i\omega\left(4\Omega^2-\omega^2+2\gamma^2\right)}\right] \\
&= \frac{16\gamma\Omega^2\left(\omega^2+4\gamma^2+4\Omega^2\right)\left[\left\langle x^2\right\rangle^2-\left\langle x\right\rangle^4\right]}{\gamma^2\left(4\Omega^2-3\omega^2\right)^2+\omega^2\left(4\Omega^2-\omega^2+2\gamma^2\right)^2} \\
&= \frac{16\gamma\Omega^2\left(\omega^2+4\gamma^2+4\Omega^2\right)\left[\left\langle x^2\right\rangle^2-\left\langle x\right\rangle^4\right]}{\left(\omega^2+\gamma^2\right)\left(\left(4\Omega^2-\omega^2\right)^2+4\omega^2\gamma^2\right)}.
\end{aligned}
\tag{D.0.9}
$$

The $S_{x^2,x^2}(\omega)$ spectrum has peaks at $\omega = 0$ and $\omega = \pm 2\Omega$.

Appendix E

Adding Qubit Dephasing

In this appendix we compare our model with the experimental results of Astafiev et al. [30]. The Hamiltonian, H_A, given in [30] is,

$$H_A = -\frac{1}{2}\left(\varepsilon\sigma_z^A + E_J\sigma_x^A\right) + \hbar\Omega\left(a^\dagger a + \frac{1}{2}\right) + \hbar g_0\left(a^\dagger + a\right)\sigma_z^A, \tag{E.0.1}$$

where the Pauli spin operators $\sigma_z^A \equiv p_2 - p_0$ and $\sigma_x^A \equiv c + c^\dagger$ are used. The form of the Hamiltonian is different to that of equation 2.4.3. However, as we now show they are equivalent. By use of the normalization of the density matrix, $\sigma_z^A = p_1 + 2p_2 - 1$, and also returning to x and p operators to describe the resonator we obtain,

$$H_A = -\varepsilon p_2 - \frac{\varepsilon}{2}\left(p_1 - 1\right) - \frac{E_J}{2}\left(c + c^\dagger\right) + \frac{p^2}{2m} + \frac{1}{2}m\Omega^2 x^2 + \frac{\hbar g_0}{x_{zp}} x\left(p_1 + 2p_2\right) - \frac{\hbar g_0}{x_{zp}} x \tag{E.0.2}$$

The last term, $-\frac{\hbar g_0}{x_{zp}}x$, is the result of a shift in the resonator coordinate between the two models as we will now show. Defining a new position coordinate $x' = x - x_0$ the Hamiltonian becomes,

$$H_S = \left(-\varepsilon + 2\frac{\hbar g_0}{x_{zp}}x_0\right)p_2 + \left(-\frac{\varepsilon}{2} + \frac{\hbar g_0}{x_{zp}}\right)p_1 + \frac{\varepsilon}{2} - \frac{E_J}{2}\left(c + c^\dagger\right) + \frac{p^2}{2m} + \frac{1}{2}m\Omega^2 x'^2 + \frac{\hbar g_0}{x_{zp}}x'\left(p_1 + 2p_2\right) + \frac{1}{2}m\Omega^2 x_0^2 + \left(\hbar\Omega^2 x_0 - \frac{\hbar g_0}{x_{zp}}\right)x'. \tag{E.0.3}$$

Constants in the Hamiltonian can always be neglected since they do not affect the dynamics of the system. Any constant shift in the energy of the $|1\rangle$ state can also be neglected since the state is only accessed via incoherent tunnelling and so has no effect on the evolution. The value of x_0 is chosen to eliminate the final term in equation E.0.3.

The Hamiltonian is then the same as equation 2.4.3 with the following definitions,

$$\Delta E = -\varepsilon + 2\frac{\hbar g_0}{x_{zp}} x_0, \tag{E.0.4}$$

$$g_0 = \frac{m\Omega^2 x_{zp}}{\hbar} x_s, \tag{E.0.5}$$

$$x_0 = \frac{\hbar g_0}{m\Omega^2 x_{zp}} = x_s, \tag{E.0.6}$$

It can be seen that in [30] the resonator position is chosen to be zero when the island charge is one whilst in our model we use an island charge of zero resulting in a position shift of x_s between the two Hamiltonians. For the quasi-particle tunnelling rate we use the model described in Section 2.2.2 to find the value of Γ_{21} on resonance and use this as the value of Γ, which as described in Section 2.2.2 is sufficient. We have checked the calculation below by using the exact rates from the model and it is found to give the same results. The values given in [30] result in the following values for the model parameters.

$$\begin{aligned} \Gamma &= 4.17\,\text{GHz} & \Omega &= 14.9\,\Gamma \\ \kappa &= 8.23 \times 10^{-6} & E_J &= 0.0344\,eV_{\text{ds}} \\ r &= 38.74 & \bar{n}_{\text{ext}} &= 0.3 \\ \gamma_{\text{ext}} &= 1.96 \times 10^{-3}\,\Gamma \end{aligned} \tag{E.0.7}$$

In figure E.1 a comparison of our model with the experimental curve for the current is shown. The JQP peak is fitted quite well by the model. The model also predicts a peak in the current at around the same position as the observed peak in the experiment. This peak corresponds to the condition $\hbar\Omega = -\sqrt{\Delta E^2 + E_J^2}$. However, the peak is not of the correct width and is too large. We also do not observe the additional features seen in the experiment for larger negative detuning.

For the experimental parameters given in equation E.0.7, $E_J \simeq 8.1\,\hbar\Gamma$ and so the condition $E_J \lesssim \hbar\Gamma$, that is assumed for our master equation (see Section 2.4) is not met. It is therefore possible that some other source of dissipation other than the quasi-particle tunnelling is important to correctly describe the SSET. In order to include extra dissipation in the qubit part of the Hamiltonian we include a pure dephasing term. For an uncoupled system this is defined in the eigenbasis of the qubit. We assume that it is unmodified by the interaction with the resonator. In order to calculate the correct form, in the charge basis, we should first diagonalize the qubit part of the Hamiltonian, H_q,

$$H_q = \Delta E p_2 - \frac{E_J}{2}\left(c + c^\dagger\right) \tag{E.0.8}$$

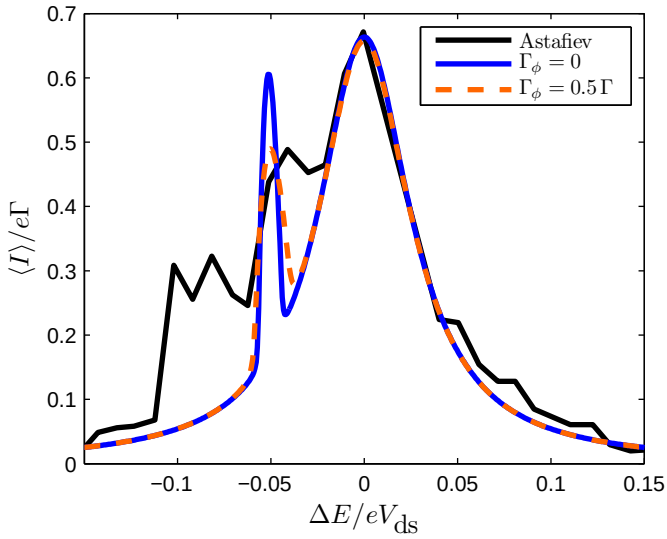

Figure E.1. A comparison of our model with the experiment in [30]. *Astafiev* is the current from the experiment shifted down by $0.08/e\Gamma$, $\Gamma_\phi = 0$ is the current by using the model from this thesis and $\Gamma_\phi = 0.5\,\Gamma$ is the current with the addition of pure dephasing of the qubit as described in this appendix. The parameters used are given in equation E.0.7.

It is diagonalized by the basis vectors,

$$\begin{aligned} |\downarrow\rangle &= \cos\left(\frac{\chi}{2}\right)|0\rangle - \sin\left(\frac{\chi}{2}\right)|2\rangle \\ |\uparrow\rangle &= \sin\left(\frac{\chi}{2}\right)|0\rangle + \cos\left(\frac{\chi}{2}\right)|2\rangle \end{aligned} \tag{E.0.9}$$

With χ set to the value,

$$\tan(\chi) = -\frac{E_J}{\Delta E}, \tag{E.0.10}$$

The diagonalized Hamiltonian is,

$$H_q = \frac{\delta\varepsilon}{2}\left(|\uparrow\rangle\langle\uparrow| - |\downarrow\rangle\langle\downarrow|\right) + \frac{\Delta E}{2}\left(|\uparrow\rangle\langle\uparrow| + |\downarrow\rangle\langle\downarrow|\right), \tag{E.0.11}$$

where $\delta\varepsilon = \sqrt{\Delta E^2 + E_J^2}$, is the energy level separation. The second term above is just a constant shift of the two levels due to our particular choice of initial Hamiltonian. The pure dephasing term uses the operator $\sigma_z \equiv |\uparrow\rangle\langle\uparrow| - |\downarrow\rangle\langle\downarrow|$ which is given by,

$$\begin{aligned} \sigma_z &= \cos(\chi)(p_2 - p_0) + \sin(\chi)\left(c + c^\dagger\right) \\ &= \frac{\Delta E}{\delta\varepsilon}(p_2 - p_0) - \frac{E_J}{\delta\varepsilon}\left(c + c^\dagger\right) \end{aligned} \tag{E.0.12}$$

The pure dephasing superoperator, $\mathcal{L}_\phi$, is of Lindblad form [49] and is defined by,

$$\mathcal{L}_\phi\rho(t) = \Gamma_\phi\left(\sigma_z\rho(t)\sigma_z - \frac{1}{2}\left\{\sigma_z^2, \rho(t)\right\}\right), \tag{E.0.13}$$

where Γ_ϕ is the dephasing rate. Figure E.1 shows the effect of additional dephasing on the current. It can be seen that the dephasing has little effect on the JQP current peak. The peak seen at the resonance is both broadened and reduced in size to be closer to that seen experimentally. However, the broadening of the peak is small in comparison to the reduction in size. The peak will therefore have disappeared before it becomes of the correct width. The addition of dephasing also does not go anyway towards explaining the second feature seen in the current. We can conclude that our model is insufficient to describe this particular experiment.

Bibliography

[1] M. Roukes, Physics World **14**, 25 (2001).

[2] K. L. Ekinci and M. L. Roukes, Rev. Sci. Instrum. **76**, 061101 (2005).

[3] K. Petersen, in *The 8th International Conference on Solid-State Sensors and Actuators, and Eurosensors IX* (1995), pp. 894–897.

[4] M. P. Blencowe, Contemporary Physics **46**, 249 (2005).

[5] M. L. Roukes, in *Technical Digest of the 2000 Solid-State Sensor and Actuator Workshop* (2000).

[6] M. P. Blencowe, Physics Reports **395**, 159 (2004).

[7] V. Sazonova, Y. Yaish, H. Üstünel, D. Roundy, T. A. Arias, and P. L. McEuen, Nature **431**, 284 (2004).

[8] R. H. Blick and D. V. Scheible, Superlattices and Microstructures **33**, 397 (2003).

[9] A. Erbe, R. H. Blick, A. Tilke, A. Kriele, and J. P. Kotthaus, Appl. Phys. Lett. **73**, 3751 (1998).

[10] R. G. Knobel and A. N. Cleland, Nature **424**, 291 (2003).

[11] D. K. Ferry and S. M. Goodnick, *Transport in Nanostructures* (Cambridge University Press, 1997), 1st ed.

[12] H. Grabert and M. H. Devoret, *Single Charge Tunneling Coulomb Blockade Phenomena in Nanostructures* (Plenum Press, New York, 1992).

[13] M. P. Blencowe and M. N. Wybourne, Appl. Phys. Lett. **77**, 3845 (2000).

[14] D. V. Averin and V. Y. Aleshkin, JETP Lett. **50**, 367 (1989).

[15] T. A. Fulton, P. L. Gammel, D. J. Bishop, L. N. Dunkleberger, and G. J. Dolan, Phys. Rev. Lett. **63**, 1307 (1989).

[16] M.-S. Choi, R. Fazio, J. Siewert, and C. Bruder, Europhys. Lett. **53**, 251 (2001).

[17] M.-S. Choi, F. Plastina, and R. Fazio, Phys. Rev. B **67**, 045105 (2003).

[18] M. P. Blencowe, J. Imbers, and A. D. Armour, New J. Phys. **7**, 236 (2005).

[19] A. A. Clerk and S. Bennett, New J. Phys. **7**, 238 (2005).

[20] S. D. Bennett and A. A. Clerk, Phys. Rev. B **74**, 201301(R) (2006).

[21] A. Naik, O. Buu, M. D. LaHaye, A. D. Armour, A. A. Clerk, M. P. Blencowe, and K. C. Schwab, Nature **443**, 193 (2006).

[22] D. A. Rodrigues, J. Imbers, T. J. Harvey, and A. D. Armour, New J. Phys. **9**, 84 (2007).

[23] D. A. Rodrigues, J. Imbers, and A. D. Armour, Phys. Rev. Lett. **98**, 067204 (2007).

[24] T. J. Harvey, D. A. Rodrigues, and A. D. Armour, Phys. Rev. B **78**, 024513 (2008).

[25] M. D. LaHaye, O. Buu, B. Camarota, and K. C. Schwab, Science **304**, 74 (2004).

[26] A. Gaidarzhy, G. Zolfagharkhani, R. L. Badzey, and P. Mohanty, Phys. Rev. Lett. **94**, 030402 (2005).

[27] K. C. Schwab, M. P. Blencowe, M. L. Roukes, A. N. Cleland, S. M. Girvin, G. J. Milburn, and K. L. Ekinci, Phys. Rev. Lett. **95**, 248901 (2005).

[28] A. Gaidarzhy, G. Zolfagharkhani, R. L. Badzey, and P. Mohanty, Phys. Rev. Lett. **95**, 248902 (2005).

[29] A. Wallraff, D. I. Schuster, A. Blais, L. Frunzio, S. K. R.–S. Huang, J. Majer, S. M. Girvin, and R. J. Schoelkopf, Nature **431**, 162 (2004).

[30] O. Astafiev, K. Inomata, A. O. Niskanen, T. Yamamoto, Y. A. Pashkin, Y. Nakamura, and J. S. Tsai, Nature **449**, 588 (2007).

[31] A. Blais, R.-S. Huang, A. Wallraff, S. M. Girvin, and R. J. Schoelkopf, Phys. Rev. A **69**, 062320 (2004).

[32] H. Carmichael, *An Open Systems Approach to Quantum Optics* (Springer-Verlag, 1993).

[33] K. Blum, *Density Matrix Theory and Applications* (Plenum Press, 1996).

[34] T. A. Fulton and G. J. Dolan, Phys. Rev. Lett. **59**, 109 (1987).

[35] U. Hanke, Y. Galperin, K. A. Chao, M. Gisselfält, M. Jonson, and R. I. Shekhter, Phys. Rev. B **51**, 9084 (1995).

[36] A. D. Armour, Phys. Rev. B **70**, 165315 (2004).

[37] R. Wilkins, E. Ben-Jacob, and R. C. Jaklevic, Phys. Rev. Lett. **63**, 801 (1989).

[38] G. Zimmerli, T. M. Eiles, R. L. Kautz, and J. M. Martinis, Appl. Phys. Lett. **61**, 237 (1992).

[39] P. Joyez, Ph.D. thesis, L'Universite Paris 6 (1995).

[40] B. D. Josephson, Physics Letters **1**, 251 (1962).

[41] A. Naik, Ph.D. thesis, University of Maryland (2006).

[42] Y. Nakamura, C. D. Chen, and J. S. Tsai, Phys. Rev. B **53**, 8234 (1996).

[43] M. Tinkham, *Introduction to Superconductivity* (McGraw-Hill, 1996), 2nd ed.

[44] A. Maassen van den Brink, G. Schön, and L. J. Geerlings, Phys. Rev. Lett. **67**, 3030 (1991).

[45] R. J. Fitzgerald, S. L. Pohlen, and M. Tinkham, Phys. Rev. B **57**, R11073 (1998).

[46] Y. Nakamura, Y. A. Pashkin, and J. S. Tsai, Nature **398**, 786 (1999).

[47] M.-S. Choi, F. Plastina, and R. Fazio, Phys. Rev. Lett. **87**, 116601 (2001).

[48] D. F. Walls and G. J. Milburn, *Quantum Optics* (Springer (Berlin), 1994).

[49] G. Lindblad, Commun. Math. Phys. **48**, 119 (1976).

[50] S. Pohlen, Ph.D. thesis, Harvard University (1999).

[51] V. Y. Aleshkin and D. V. Averin, Physica B **165&166**, 949 (1990).

[52] R. Fazio, G. M. Palma, and J. Siewert, Phys. Rev. Lett. **83**, 5385 (1999).

[53] Y. Makhlin, G. Schön, and A. Shnirman, *New Directions in Mesoscopic Physics (Towards Nanoscience)* (Kluwer, 2003), chap. Dissipation in Josephson qubits.

[54] A. Abramovici, W. Althouse, J. Camp, D. Durance, J. A. Giaime, A. Gillespie, S. Kawamura, A. Kuhnert, T. Lyons, F. J. Raab, et al., Physics Letters A **218**, 157 (1996).

[55] A. N. Cleland, *Foundations of Nanomechanics: From Solid State Theory to Device Applications* (Springer-Verlag, 2003).

[56] M. D. LaHaye, Ph.D. thesis, University of Maryland (1995).

[57] A. D. Armour, M. P. Blencowe, and Y. Zhang, Phys. Rev. B **69**, 125313 (2004).

[58] C. M. Caves, K. S. Thorne, R. W. P. Drever, V. D. Sandberg, and M. Zimmermann, Rev. Mod. Phys. **52**, 341 (1980).

[59] C. M. Caves, Phys. Rev. D **26**, 1817 (1982).

[60] M. H. Devoret and R. J. Schoelkopf, Nature **406**, 1039 (2000).

[61] C. Flindt, Master's thesis, Technical University of Denmark (2004).

[62] D. Kohen, C. C. Marston, and D. J. Tannor, J. Chem. Phys. **107**, 5236 (1997).

[63] C. Flindt, T. Novotný, and A.-P. Jauho, Phys. Rev. B **70**, 205334 (2004).

[64] H.-J. Briegel and B.-G. Englert, Phys. Rev. A **47**, 3311 (1993).

[65] M. Jakob and S. Stenholm, Phys. Rev. A **69**, 042105 (2004).

[66] I. Djuric, B. Dong, and H. L. Cui, J. Appl. Phys. **99**, 063710 (2006).

[67] T. Brandes, Ann. Phys. **17**, 477 (2008).

[68] Y. M. Blanter and M. Buttiker, Phys. Rep. **336**, 1 (2000).

[69] G. Doetsch, *Guide to the Applications of the Laplace and Z Transforms* (Van Nostrand Reinhold Company, 1967), 2nd ed.

[70] D. Mozyrsky, L. Fedichkin, S. A. Gurvitz, and G. P. Berman, Phys. Rev. B **66**, 161313 (2002).

[71] L. Y. Chen and C. S. Ting, Phys. Rev. B **43**, 4534 (1991).

[72] T. Novotný, A. Donarini, and A.-P. Jauho, Phys. Rev. Lett. **90**, 256801 (2003).

[73] C. C. Gerry and P. L. Knight, *Introductory Quantum Optics* (Cambridge University Press, 2005).

[74] L. Saminadayar, D. C. Glattli, Y. Jin, and B. Etienne, Phys. Rev. Lett. **79**, 2526 (1997).

[75] R. de Picciotto, M. Reznikov, M. Heiblum, V. Umansky, G. Bunin, and D. Mahalu, Nature **389**, 162 (1997).

[76] M. Reznikov, R. de Picciotto, T. G. Griffiths, M. Heiblum, and V. Umansky, Nature **399**, 238 (1999).

[77] M. O. Scully and M. S. Zubairy, *Quantum Optics* (Cambridge University Press, 1997).

[78] M. Merlo, F. Haupt, F. Cavaliere, and M. Sassetti, New J. Phys. **10**, 023008 (2008).

[79] P. Filipowicz, J. Javanainen, and P. Meystre, Phys. Rev. A **34**, 3077 (1986).

[80] A. A. Clerk, Phys. Rev. B **70**, 245306 (2004).

[81] D. A. Rodrigues and G. J. Milburn, Phys. Rev. B **78**, 104302 (2008).

[82] C. Cohen-Tannoudji, B. Diu, and F. Laloë, *Quantum Mechanics: Volume One* (Hermann and John Wiley & Sons Inc., 1977).

[83] F. Pistolesi, Y. M. Blanter, and I. Martin, Phys. Rev. B **78**, 085127 (2008).

[84] M. A. Armen and H. Mabuchi, Phys. Rev. A **73**, 063801 (2006).

[85] R. Aguado and T. Brandes, Eur. Phys. J. B **40**, 357 (2004).

[86] B.-G. Englert and G. Morigi, in *Coherent Evolution in Noisy Environments*. Lecture Notes in Phys. (Springer, Berlin) **611**, 55 (2002).

[87] D. A. Rodrigues, Phys. Rev. Lett. **102**, 067202 (2008).

[88] A. Isacsson and T. Nord, Europhys. Lett. **66**, 708 (2004).

[89] T. Novotný, A. Donarini, C. Flindt, and A.-P. Jauho, Phys. Rev. Lett. **92**, 248302 (2004).

[90] C. Flindt, T. Novotný, and A.-P. Jauho, Europhys. Lett. **69**, 475 (2005).

[91] O. Usmani, Y. M. Blanter, and Y. V. Nazarov, Phys. Rev. B **75**, 195312 (2007).

[92] A. N. Jordan and E. V. Sukhorukov, Phys. Rev. Lett. **93**, 260604 (2004).

[93] C. Emary, D. Marcos, R. Aguado, and T. Brandes, Phys. Rev. B **76**, 161404(R) (2007).

[94] C. Flindt, T. Novotný, and A.-P. Jauho, Physica E **29**, 411 (2005).

[95] M. B. Plenio and P. L. Knight, Rev. Mod. Phys. **70**, 101 (1998).

[96] H. M. Wiseman, Quantum Semiclass. Opt. **8**, 205 (1996).

[97] H. M. Wiseman and G. J. Milburn, Phys. Rev. A **49**, 1350 (1994).

[98] L. Susskind and J. Glogower, Physics **1**, 49 (1968).

[99] P. Carruthers and M. M. Nieto, Rev. Mod. Phys. **40**, 411 (1968).

[100] S. M. Tan, J. Opt. B: Quantum Semiclass. Opt. **1**, 424 (1999).

[101] The Mathworks, *www.mathworks.com*, Website.

[102] R. B. Lehoucq, D. C. Sorensen, and C. Yang, *ARPACK Users' Guide: Solution of Large-Scale Eigenvalue Problems with Implicitly Restarted Arnoldi Methods* (SIAM, 1998).

[103] T. A. Davies, ACM Transactions on Mathematical Software **30**, 165 (2004).

[104] L. Y. Gorelik, A. Isacsson, M. V. Voinova, B. Kasemo, R. I. Shekhter, and M. Jonson, Phys. Rev. Lett. **80**, 4526 (1998).

[105] H. M. Wiseman and G. J. Milburn, Phys. Rev. A **47**, 642 (1993).

[106] H. M. Wiseman and G. J. Milburn, Phys. Rev. A **47**, 1652 (1993).

[107] S. Gustavsson, R. Leturcq, B. Simovic, R. Schleser, P. Studerus, T. Ihn, K. Ensslin, D. C. Driscoll, and A. C. Gossard, Phys. Rev. B **74**, 195305 (2006).

[108] S. Gustavsson, I. Shorubalko, R. Leturcq, T. Ihn, K. Ensslin, and S. Schön, Phys. Rev. B **78**, 035324 (2008).

[109] C. Flindt, C. Fricke, F. Hohls, T. Novotný, K. Netocný, T. Brandes, and R. J. Haug, arXiv:0901.0832v1 (2009).

[110] H. J. Carmichael, S. Singh, R. Vyas, and P. R. Rice, Phys. Rev. A **39**, 1200 (1989).

[111] W. H. Press, S. A. Teukolsky, W. T. Vetterling, and B. P. Flannery, *Numerical Recipes in C: The Art of Scientific Computing* (Cambridge University Press, 1992).

[112] C. W. Gardiner, *Handbook of Stochastic Methods: for Physics, Chemistry and the Natural Sciences* (Springer-Verlag, 2004), 3rd ed.